ABSTRACT

FENG, SHUO. 3D Integral Invariant Signatures And Their Application on Face Recognition. (Under the direction of Professor Hamid Krim).

Curves are important features in computer vision and pattern recognition, and their classification under a variety of transformations, such as Euclidean, affine or projective, poses a great challenge. Invariant features of these curves turn out to be crutial to simplifying any classification procedure. This, as a result, has recently led to a renewed research interest in transformation invariants.

In this thesis, new explicit formulae for integral invariants for curves in 3D with respect to the special and the full affine groups are presented.The development of the 3D integral invariant are based on an inductive approach in terms of Euclidean invariants. For the first time, a clear geometric interpretation of both 2D and 3D integral invariants is presented. Since integration attenuates the effects of noise, integral invariants have advantages in computer vision applications. We use integral invariants to construct global and local signatures that characterize curves up to the special affine transformations, subsequently extended to the full affine group. Global Signatures are independent of parameterization, and Local Signatures are independent of both parameterizationa and initial point selection. We analyze the robustness of these invariants in their application to the problem of classification of noisy spatial curves extracted as characteristics from a 3D object.

Our investigation of 2D and 3D integral invariants and signatures, originally motivated by Biometrics applications, are successfully implemented and applied to face recognition to eliminate the effects of pose and facial expression. A high recognition performance rate of 95% is achieved in the test with a large face data set.

3D Integral Invariant Signatures And Their Application on Face Recognition

by

Shuo Feng

A dissertation submitted to the Graduate Faculty of
North Carolina State University
in partial fulfillment of the
requirements for the Degree of
Doctor of Philosophy

Electrical Engineering

Raleigh, NC

2007

Approved By:

Dr. Michael Escuti	Dr. Griff Bilbro
Dr. Hamid Krim Chair of Advisory Committee	Dr. Irina Kogan

Dedication

To my wife

Ying Zhang

my daughter

Grace Zixuan Feng

and my parents

Baopu Feng and **Yulian Yuan**

Biography

Shuo Feng was born in Binzhou, Shangdong Province, P. R. China, where he attended the elementary school and high school. He received his B.S. degrees in Electrical Engineering from Tianjin University, China, in 2000, and M.S degree in Computer Science and Engineering from Oakland University, Michigan in 2002. He is currently pursuing his Ph.D. degree in the Department of Electrical and Computer Engineering at North Carolina State University. His research interests include statistical signal/image processing, geometric invariants, computer vision, pattern recognition, and biometrics.

Acknowledgements

I would like to express my sincere gratitude to my adviser, Dr. Hamid Krim, for his guidance, support and encouragement during my PhD study. Dr. Krim introduced me to the new interesting areas, inspired me with new ideas, and polished my technical writing through numerous revisions.

I am grateful for the support and guidance I have received from Dr. Irina A. Kogan, and I also express my gratitude to Dr. Michael Escuti and Dr. Griff Bilbro for serving on my advisory committee, for their interest in the topic with further suggestions.

Many thanks go to former and present students of VISSTA group for many discussions on research and life in general.

Finally, I'd like to thank my wife, my parents and all my family members for their support and encouragement.

Contents

List of Figures

List of Tables

Chapter 1

Introduction

a human being can easily recognize an airplane, tell the difference between a horse and an elephant, identify faces, and understand handwritten characters by "looking at" them. The complicated underlying procedure is, of course, not so simple. Human eyes first capture the scene, the brain then smartly selects the region of interest (ROI), extracts features from the ROI, and makes a decision. It takes almost no time for this procedure.

With the rapid development of computer technologies, it is natural to ask if machines can perform as efficiently. Although the answer is not a perfect "Yes" nowadays, under some reasonable assumptions, a computer is capable to carry out most of the tasks listed above. They are actually typical computer vision problems, and various solutions are available in the literatures.

A typical computer vision system architecture is illustrated in Fig. 1.1. It has a total of five stages: sensing, ROI selection, feature selection, classification, and postprocessing.‘

A real world scene has to be converted into a binary signal, so that a computer is able to process it. To this end, the first stage is always sensing. Various sensors may be required to convert real a world scene to different usable data. For example, a 2D camera may capture a grayscale or a color 2D picture as shown in Fig. 1.2-a, while a 3D scanner captures the full 3D geometry in Fig. 1.2-b. A thermal map (in Fig. 1.2-c) may be achieved using an infrared camera, while signals from spectral

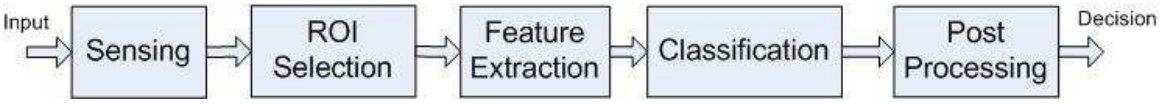

Figure 1.1: Computer vision system architecture

bands (in Fig. 1.3) may be acquired by a multispectral camera.

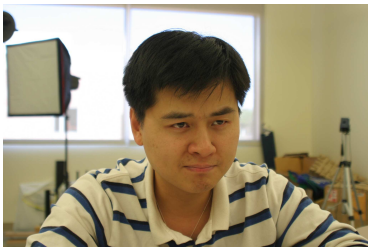

(a)2D face

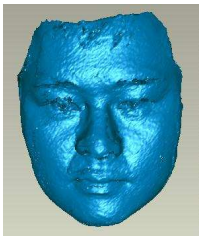

(b) 3D face

(c) Infrared face

Figure 1.2: 2D and 3D data

Oftentimes, a region of interest (ROI) is captured together with background noise in the data, which makes ROI selection(or segmentation) a necessary step for future processing. The segmented region, however, may not be used directly for classification. The input of classifiers are a small subset of ROI containing characteristic information, which is called "the feature". An optimal feature selection would yield a representation to maximally simplify an object classification. With a proper classifier, an object may be identified, and post-processing may help interpret the classification output and make a decision.

1.1 Motivation

Among the stages discussed in the previous section, feature selection is one of the most critical stages. A good feature is the one that remains very similar for objects from same class, very distinct for different classes, all the while invariant to

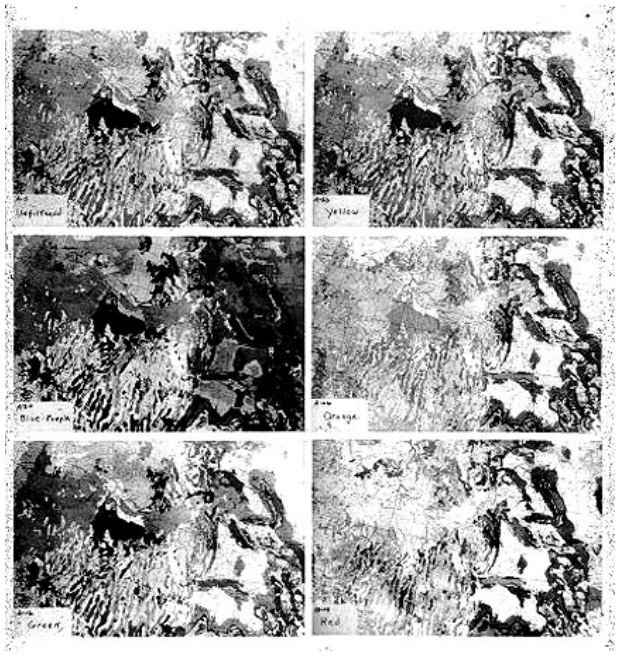

Figure 1.3: Multispectral data from Landsat

geometric transformations on the objet. By selecting enough distinct features, the whole problem may be simplified, and the system performance may be increased.

Features may include color of objects, size of object, or some geometrical characteristics, such as points(in Fig. 1.4), or curves(in Fig. 3.4-a,b). In computer vision and pattern recognition, curves/contours are important features. The objects may undergo various transformations, such as translation, rotation, scaling, and shearing, as a result, feature curves may subject to the same transformations. Their classification under geometrical transformations is challenging. A direct comparison of feature curves generally requires registration, and the ensuing complexity and difficulty in its application in many important problems, have recently led to a renewed research interest in "transformation invariant".

Differential invariants, such as Euclidean curvature and torsion for space curves, are the most classical. The affine and projective counterparts of curvature and torsion

may also be defined. The practical utilization of differential invariants is, however, limited due to their high sensitivity to noise. Indeed, Euclidean curvature and torsion depend on derivatives of up to order 2 and 3 respectively, and their affine analogs depend on derivatives of up to order 6[26]. If the original data is noisy, the numerical differentiation amplifies the effects of noise. This motivated the high interest in other types of invariants such as semi-differential, or joint invariants [48, 37, 4] and various types of integral invariants [42, 30, 33, 21]. Integral invariants in the above references depend on quantities obtained by integration of various functions along a curve. Since integration reduces the effect of noise, integral invariants hold a clear advantage in practical applications. The type of integral invariants that we consider in the sequel was introduced by [21], and may be considered as the 1-dimensional analogs of moment invariants [49].

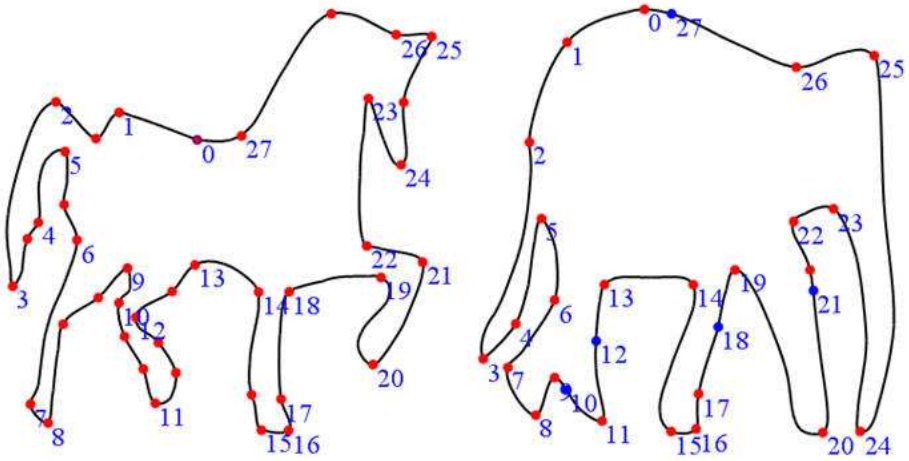

Figure 1.4: feature points

While explicit expressions for integral invariants are known for plane curves in 2D, they have thus far remained elusive for spatial curves in 3D, primarily on account of their analytical tractability. With an increasing availability of 3D data acquisition systems and subsequent emerging applications, interest in 3D analysis and in associated robust integral invariants for 3D curves in 3D is key. In this thesis, we develop

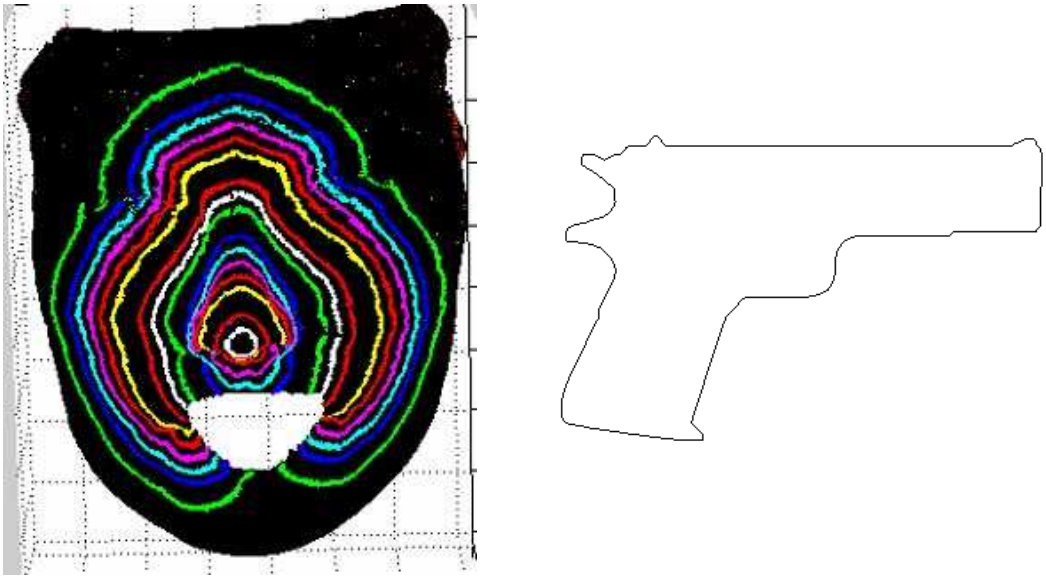

(a)face feature curves (b) gun feature contour

Figure 1.5: Feature points of 2 planar shapes

3D integral invariants/signatures within the context of biometrics and for a natural adaptation to 3D object recognition and face recognition.

1.2 Contribution

The contributions of this thesis are set of as following,

A hybrid integro-differential affine invariantwhich only uses only the first order derivatives along with integrals was developed [15]. Although a performance improvement over classical deferential invariants is achieved, the presence of first order derivatives still affects the performance.

As first appeared in [16], we obtain for the first time explicit formulae of **integral Euclidean and affine invariants for spatial curves in 3D**. The type of curve integral invariants, computed in this paper, may be viewed as a 1-dimensional analog of moment invariants [45, 49]. For plane curves they were introduced and computed by Hann and Hickerman [21]. The standard action of the affine group on $\mathbb{R}^3$ induces an action on curves. Following the approach of [21] we prolong this action to certain

integral expressions, called potentials, and then compute invariants that depend on these integral variables. A direct extension of [21] to 3D, using Fels-Olver moving frame construction [13] is conceptually straight forward, but the computational complexity often makes the problem intractable. An inductive implementation of the moving frame construction, proposed by Kogan [26], significantly simplifies the algebraic derivations, as it allows one to construct invariants for an entire group from the invariants of its subgroup: in our case affine invariants in terms of Euclidean ones.

The integral invariants defined in [21] and [16] are sensitive to parametrization, or sampling of the curve in the discrete case. A uniform parametrization is required for two curves to be compared. In order to overcome this limitation, we develop **local and global 2D/3D integral invariant signatures for the special affine and full affine group**. The global signature depends on the choice of the initial point and does not allow a comparison if fragments of the curves, and is therefore sensitive to occlusions. The local signature, at a slight computational cost, is independent on the choice of the initial point, and is insensitive to the occlusion in the image. It allows to establish local equivalence of the curves.

In [14], we develop a **matching techniques of 3D objects with articulated parts using 3D Euclidean integral invariant signature**. 3D objects are represented by a set of characteristic and intrinsic curves. The object matching is based on comparing integral invariant signatures of corresponding iso-geodesic curves.

Euclidean/Affine Integral invariants/signatures are also shown to be very useful to a biometric application–face recognition. A human face may be represented by a set of vertical and horizonal planar curves [18], and 2D affine integral invariants are introduced to mitigate the effect of pose on the facial curves. Alternatively, a human face may also more robustly be represented by a set of characteristic level curves starting from the nose tip [17]. 3D integral invariants and signatures for space curves are used to eliminate both pose and facial expression. Both approaches achieve accuracy greater than 90%.

1.3 Organization of the thesis

The outline of this thesis is as follows:

We start the next chapter with some mathematical background to introduce the basic concept of geometric transformation, geometric invariant, the moving frame approach to achieve invariant, and an example (2D integral invariant development) is given to show how it works. In Chapter 3, we describe the first approach extending the existing 2D integral invariant to 3D, and illustrate the difficulty–computation complexity–and provide a solution to achieve a hybrid invariant which utilizes lower order(only first order) derivatives and integral auxiliary variables. Although a performance improvement over classical deferential invariants is obtained, the presence of first order derivatives still affects the performance. In Chapter 4, an inductive approach developed by Kogan[26] is exploited to simplify the analytical tractability. As an example, a 2D integral invariant is rederived. We then proceed to develop 3D integral invariants using this inductive approach in Chapter 5. Specifically, three special affine integral invariants are derived. Since each individual integral invariant depends on curve parameterization and initial point selection, we introduce in terms of global and local signatures in Chapter 6 to cancel the parameterization and initialization respectively. In Chapter 7, three interesting applications, namely face recognition with 2D affine integral invariants, 3D object recognition using 3D Euclidean Integral Invariant Signature, and 3D face recognition using 3D integral invariants and signatures, are proposed. Some concluding remarks and future extensions are discussed in Chapter 8.

Chapter 2

Preliminary

This thesis discusses a systematic way of developing integral invariants/signatures for Euclidean and Affine transformations in 2D and 3D. The following background material is presented to provide a context for the remainder of the thesis. Geometric transformations are first discussed, followed by that of geometric invariants and the classical approach to achieve invariants. We finally provide a 2D integral invariant development example to illustrate the moving frame technique.

2.1 Geometric transformation

Generally, when considering geometric transformations, one may refer to either the object or the coordinate system being transformed. Although the two cases are directly related, the transformation matrices are still quite different. In this thesis, all transformations we are discussing are objects based.

The basic transformations of interest hence are: translation, rotation, scaling, shearing, and their combinations (Euclidean transformation, affine transformation) in 2D and 3D

TRANSLATION

Let $\begin{pmatrix} x_1 \\ \vdots \\ x_n \end{pmatrix}$ and $\begin{pmatrix} \overline{x_i} \\ \vdots \\ \overline{x_n} \end{pmatrix}$ be two vectors in $\mathbb{R}^n$. The translation affected by a vector $(v_1, \ldots v_n) \in \mathbb{R}^n$ is as follow:

$$\begin{pmatrix} \overline{x_i} \\ \vdots \\ \overline{x_n} \end{pmatrix} = \begin{pmatrix} x_1 \\ \vdots \\ x_n \end{pmatrix} + \begin{pmatrix} v_1 \\ \vdots \\ v_n \end{pmatrix}. \tag{2.1}$$

ROTATION

Rotation is described by:

$$\begin{pmatrix} \overline{x_i} \\ \vdots \\ \overline{x_n} \end{pmatrix} = R \begin{pmatrix} x_1 \\ \vdots \\ x_n \end{pmatrix}, \tag{2.2}$$

where a rotation matrix R is an orthogonal matrix, and $det(R) = 1$.

In a 2D case, a rotation matrix about the origin by an angle θ is given by:

$$R_{2D} = \begin{pmatrix} cos(\theta) & sin(\theta) \\ -sin(\theta) & cos(\theta) \end{pmatrix},$$

where θ is the rotation parameter.

In a 3D case, a rotation matrix is given by:

$$R_{3D} = \begin{pmatrix} 1 & 0 & 0 \\ 0 & cos(\psi) & -sin(\psi) \\ 0 & sin(\psi) & cos(\psi) \end{pmatrix} \cdot \begin{pmatrix} cos(\phi) & 0 & sin(\phi) \\ 0 & 1 & 0 \\ -sin(\phi) & 0 & cos(\phi) \end{pmatrix} \cdot \begin{pmatrix} cos(\theta) & -sin(\theta) & 0 \\ sin(\theta) & cos(\theta) & 0 \\ 0 & 0 & 1 \end{pmatrix},$$

where ψ, ϕ, and θ specify the rotation angels with respect to x, y, z axis.

SCALING

A scaling transformation is featured by a diagonal transformation matrix. In 2D,

it is defined as

$$\begin{pmatrix} \overline{x} \\ \overline{y} \end{pmatrix} = \begin{pmatrix} s_1 & 0 \\ 0 & s_2 \end{pmatrix} \begin{pmatrix} x \\ y \end{pmatrix}, \tag{2.3}$$

while a 3D scaling transformation is given by

$$\begin{pmatrix} \overline{x} \\ \overline{y} \\ \overline{z} \end{pmatrix} = \begin{pmatrix} s_1 & 0 & 0 \\ 0 & s_2 & 0 \\ 0 & 0 & s_3 \end{pmatrix} \begin{pmatrix} x \\ y \\ z \end{pmatrix}. \tag{2.4}$$

SHEARING

A shearing transformation behaves as "pushing" an object in a direction parallel to a coordinate plane in 3D or a coordinate axis in 2D. An examples is shown in Fig. 2.1.

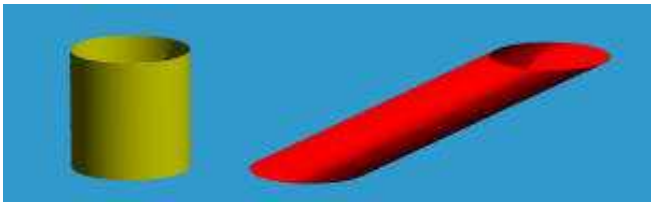

Figure 2.1: 3D shearing transformation on a cylindrical shape.

In a 2D case, a shearing transformation in the x direction with a shearing factor sh_x and in the y direction with a shearing factor sh_y are defined as:

$$\begin{pmatrix} \overline{x} \\ \overline{y} \end{pmatrix} = \begin{pmatrix} 1 & sh_x \\ 0 & 1 \end{pmatrix} \begin{pmatrix} x \\ y \end{pmatrix}, \tag{2.5}$$

$$\begin{pmatrix} \overline{x} \\ \overline{y} \end{pmatrix} = \begin{pmatrix} 1 & 0 \\ sh_y & 1 \end{pmatrix} \begin{pmatrix} x \\ y \end{pmatrix}. \tag{2.6}$$

In 3D space, a shearing transformation with respect to $x-y$ plane, $x-z$ plane and $y-z$ plane are defined as:

$$\begin{pmatrix} \overline{x} \\ \overline{y} \\ \overline{z} \end{pmatrix} = \begin{pmatrix} 1 & 0 & sh_x \\ 0 & 1 & sh_y \\ 0 & 0 & 1 \end{pmatrix} \begin{pmatrix} x \\ y \\ z \end{pmatrix}, \tag{2.7}$$

$$\begin{pmatrix} \overline{x} \\ \overline{y} \\ \overline{z} \end{pmatrix} = \begin{pmatrix} 1 & sh_x & 0 \\ 0 & 1 & 0 \\ 0 & sh_z & 1 \end{pmatrix} \begin{pmatrix} x \\ y \\ z \end{pmatrix}, \tag{2.8}$$

$$\begin{pmatrix} \overline{x} \\ \overline{y} \\ \overline{z} \end{pmatrix} = \begin{pmatrix} 1 & 0 & 0 \\ sh_y & 1 & 0 \\ sh_z & 0 & 1 \end{pmatrix} \begin{pmatrix} x \\ y \\ z \end{pmatrix}. \tag{2.9}$$

An example of these four basic transformations on 3D space curves is shown in Fig. 2.2.

The two transformations we consider in this thesis, namely Euclidean transformation and affine transformation are a combination of the above basic transformations.

EUCLIDEAN TRANSFORMATION

A Euclidean transformation includes a translation and a rotation, and is defined in 2D and 3D as:

$$\begin{pmatrix} \overline{x} \\ \overline{y} \end{pmatrix} = \begin{pmatrix} cos(\theta) & sin(\theta) \\ -sin(\theta) & cos(\theta) \end{pmatrix} \begin{pmatrix} x \\ y \end{pmatrix} + \begin{pmatrix} v_x \\ v_y \end{pmatrix}, \tag{2.10}$$

$$\begin{pmatrix} \overline{x} \\ \overline{y} \\ \overline{z} \end{pmatrix} = R_{3D} \begin{pmatrix} x \\ y \\ z \end{pmatrix} + \begin{pmatrix} v_x \\ v_y \\ v_z \end{pmatrix}, \tag{2.11}$$

AFFINE TRANSFORMATION

An affine transformation may be viewed as a combination of a translation, a rotation, a scaling and a shearing. The standard affine transformation in 2D is defined

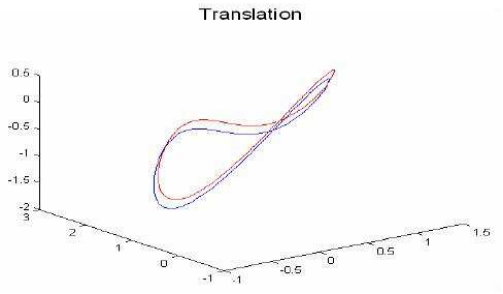

(a) translation

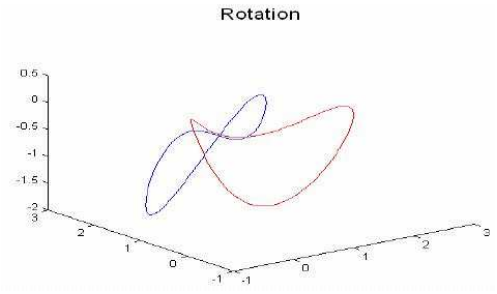

(b) rotation

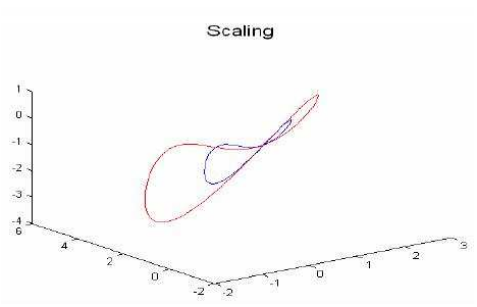

(c) scaling

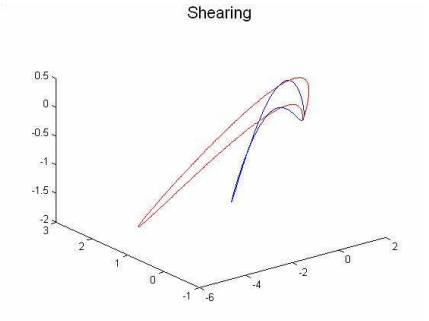

(d) shearing

Figure 2.2: Four basic transformations in 3D of a space curve

as:

$$\begin{pmatrix} \overline{x} \\ \overline{y} \end{pmatrix} = \begin{pmatrix} a_{11} & a_{12} \\ a_{21} & a_{22} \end{pmatrix} \begin{pmatrix} x \\ y \end{pmatrix} + \begin{pmatrix} v_1 \\ v_2 \end{pmatrix}, \quad \det \begin{pmatrix} a_{11} & a_{12} \\ a_{21} & a_{22} \end{pmatrix} \neq 0. \tag{2.12}$$

The standard affine transformation in 3D:

$$\begin{pmatrix} \overline{x} \\ \overline{y} \\ \overline{z} \end{pmatrix} = \begin{pmatrix} a_{11} & a_{12} & a_{13} \\ a_{21} & a_{22} & a_{23} \\ a_{31} & a_{32} & a_{33} \end{pmatrix} \begin{pmatrix} x \\ y \\ z \end{pmatrix} + \begin{pmatrix} v_1 \\ v_2 \\ v_3 \end{pmatrix}, \quad \det \begin{pmatrix} a_{11} & a_{12} & a_{13} \\ a_{21} & a_{22} & a_{23} \\ a_{31} & a_{32} & a_{33} \end{pmatrix} \neq 0, \tag{2.13}$$

where $\det \begin{pmatrix} a_{11} & a_{12} \\ a_{21} & a_{22} \end{pmatrix} = 1$ or $\det \begin{pmatrix} a_{11} & a_{12} & a_{13} \\ a_{21} & a_{22} & a_{23} \\ a_{31} & a_{32} & a_{33} \end{pmatrix} = 1$, the transformation is referred to as a special affine transformation (affine transformation without scaling).

2.2 Group action and geometric invariants

In this section we review the basic terminology of the group actions and invariants, as well as the concept of prolonging the action to jet spaces and the notion of differential invariants. We then introduce the notion of *integral jet space* and define the corresponding prolongation of the action to give rise to *integral invariants*.

2.2.1 Definitions

Definition 2.2.1 *An action of a group G on a set S is a map $\alpha\colon G \times S \to S$ that satisfies the following two properties:*

1. *$\alpha(e, s) = s$, $\forall s \in S$, where e is the identity of the group.*
2. *$\alpha(g_1, \alpha(g_2, s)) = \alpha(g_1\, g_2, s)$, for all $s \in S$ and $g_1, g_2 \in G$.*

For $g \in G$ and $s \in S$ we write $\alpha(g, s) = g \cdot s = \overline{s}$.

Definition 2.2.2 *The* orbit *of a point $s \in S$ is the set $O_s = \{g \cdot s | g \in G\}$.*

Definition 2.2.3 *A function $f\colon S \to \mathbb{R}$ is called* invariant *if*

$$f(g \cdot s) = f(s),\ \forall g \in G \text{ and } \forall s \in S \tag{2.14}$$

Invariant functions are constant along each orbit and can be used to find equivalence classes of objets undergoing various types of transformations.

Let $\mathcal{G}L(n)$ denote a group of non-degenerate $n \times n$ matrices with real entries. Its subgroup of matrices with determinant 1 is denoted by $\mathcal{S}L(n)$. The *orthogonal group* is $\mathcal{O}(n) = \{A \in \mathcal{G}L(n) | AA^T = I\}$, while the *special orthogonal group* is $\mathcal{S}O(n) =$

$\{A \in \mathcal{O}(n) | \det A = 1\}$. The semi-direct product of $\mathcal{G}L(n)$ and $\mathbb{R}^n$ is called the *affine group*: $\mathcal{A}(n) = \mathcal{G}L(n) \ltimes \mathbb{R}^n$. Its subgroup $\mathcal{S}A(n) = \mathcal{S}L(n) \ltimes \mathbb{R}^n$ is called the *special affine group*. The *Euclidean group* is $\mathcal{E}(n) = \mathcal{O}(n) \ltimes \mathbb{R}^n$. Its subgroup $\mathcal{S}E(n) = \mathcal{S}O(n) \ltimes \mathbb{R}^n$ is called the *special Euclidean group*.

Throughtout we consider the action of the affine group $\mathcal{A}(n)$ and its subgroups on $\mathbb{R}^n$ by a composition of a linear transformation and a translation, for $n = 2$ and $n = 3$:

$$\begin{pmatrix} \overline{x_i} \\ \vdots \\ \overline{x_n} \end{pmatrix} = A \begin{pmatrix} x_1 \\ \vdots \\ x_n \end{pmatrix} + \begin{pmatrix} v_1 \\ \vdots \\ v_n \end{pmatrix}. \tag{2.15}$$

where matrix $A \in \mathcal{G}L(n)$ defines a linear transformation and the vector $(v_1, \dots v_n) \in \mathbb{R}^n$ defines a translation.

2.2.2 Prolongation of a group action

A group action in Eq.(2.15) on $\mathbb{R}^n$ induces an action on curves $\gamma(t) = (x_1(t), \dots, x_n(t)) \rightarrow \overline{\gamma}(t) = (\overline{x_1}(t), \dots, \overline{x}_n(t))$ in $\mathbb{R}^n$. Our goal is to obtain invariants that classify curves up to affine transformations. The classical method of obtaining such invariants is to prolong the action to the set of derivatives $\{x_1^{(k)}, \dots, x_i^{(k)} | k = 1..l\}$ of a sufficiently high order l [1]:

$$\overline{x_i^{(1)}}(t) = \frac{d\overline{x_i}(t)}{dt}, \quad \overline{x_i^{(k+1)}}(t) = \frac{d\overline{x_i^{(k)}}(t)}{dt}. \tag{2.16}$$

Definition 2.2.4 *Functions of* $\{x_1, \dots, x_n, x_i^{(k)} \mid i = 1..n,\ k = 1..l\}$ *that are invariant under the prolonged action (2.16) are called* differential invariants *of order* l.

For the Euclidean action on curves in 3D, the two lowest order invariants are called curvature and torsion, and are classically known in differential geometry. Analogous invariants for the affine and projective groups are also known [26].

Differential invariant may be achieved by regularization[13]. For a $r(r < l*(k+1))$ dimensional group, r prolonged group may be normalized to r random constants $(c_1, \cdots, c_r)$, so that the group parameters are fixed by solving the resulting system of

equations. The invariants are achieved by replacing the fixed group parameters into the rest $l*(k+1)-r$ of prolonged group.

As noted in the introduction, differential invariants of particularly high order derivatives are highly sensitive to noise. To alleviate this sensitivity, we extend the approach of [21] from planar curves to curves in a space of arbitrary dimension. Let the curve $\gamma(t)$ be parametrized by $t \in [a,b]$. To that end, we define integral variables

$$X_i^{(\alpha_1,\ldots,\alpha_n)}(t) = \int_a^t x_1(t)^{\alpha_1} \cdots x_n(t)^{\alpha_n} dx_i(t), \tag{2.17}$$

where the integrals are taken along the curve $\gamma(t)$, $(\alpha_1,\ldots,\alpha_n)$ are non-negative integers such that $\alpha_1+\cdots+\alpha_{i-1}+\alpha_{i+1}+\cdots+\alpha_n \neq 0$. We call $l=\alpha_1+\cdots+\alpha_n$ the order of integral variables. There are relations among the integral variables dictated by the integration by parts formulas. Examples of such relations for $n=2$ are given in Section 2.3 below.

Definition 2.2.5 *An* integral jet space of order l *(denoted* $\mathcal{S}^l$*) is the space parametrized by the coordinates* $x_1,\ldots x_n$*, of an arbitrary point on a curve* $\gamma(t)$*,* $t\in[a,b]$*, coordinates* $x_1^0,\ldots x_n^0$ *of the initial point* $\gamma(a)$ *on the curve, and all independent integral variables* $X_i^{(\alpha_1,\ldots,\alpha_n)}$ *of order* l *and less.*

The action (2.15) can be prolonged to the initial point and to the integral variables of order l:

$$\begin{aligned}
\begin{pmatrix} \overline{x_i} \\ \vdots \\ \overline{x_n} \end{pmatrix} &= A \begin{pmatrix} x_1 \\ \vdots \\ x_n \end{pmatrix} + \begin{pmatrix} v_1 \\ \vdots \\ v_n \end{pmatrix} \\
\begin{pmatrix} \overline{x_i^0} \\ \vdots \\ \overline{x_n^0} \end{pmatrix} &= A \begin{pmatrix} x_1^0 \\ \vdots \\ x_n^0 \end{pmatrix} + \begin{pmatrix} v_1 \\ \vdots \\ v_n \end{pmatrix}, \\
\overline{X_i^{(\alpha_1,\ldots,\alpha_n)}} &= \int_\gamma \overline{x_1}^{\alpha_1} \cdots \overline{x_n}^{\alpha_n} d\overline{x_i}.
\end{aligned} \tag{2.18}$$

It is important that the relations among the integral variables be respected under the prolonged action, and therefore the action of the integral jet space $\mathcal{S}^l$ is well defined.

Definition 2.2.6 *A function on $\mathcal{S}^l$ which is invariant under the prolonged action (2.18) is called* integral invariant of order l.

By introducing new variables

$$X_i = x_i - x_i^0,\ i = 1, \ldots, n \tag{2.19}$$

and making the corresponding substitution into the integrals, we reduce the problem of finding invariants under the action (2.18) to an equivalent but simpler problem of finding invariant functions of variables $\{X_1, \ldots, X_n, X_i^{(\alpha_1,\ldots,\alpha_n)} \,|\, i = 1 \ldots n\}$ under the action of $GL(n)$ defined by

$$\begin{aligned} \begin{pmatrix} \overline{X_i} \\ \vdots \\ \overline{X_n} \end{pmatrix} &= A \begin{pmatrix} X_1 \\ \vdots \\ X_n \end{pmatrix} \\ \overline{X_i^{(\alpha_1,\ldots,\alpha_n)}} &= \int_\gamma \overline{X_1}^{\alpha_1} \cdots \overline{X_n}^{\alpha_n} d\overline{X_i}. \end{aligned}$$

Invariants with respect to (2.18) may be obtained from invariants with respect to (2.20) by making substitution (2.19). As an example, 2D integral Invariant development is discussed in the next section.

2.3 2D integral invariant development

The standard affine group action on $\mathbb{R}^2$:

$$\begin{pmatrix} \overline{x} \\ \overline{y} \end{pmatrix} = \begin{pmatrix} a_{11} & a_{12} \\ a_{21} & a_{22} \end{pmatrix} \begin{pmatrix} x \\ y \end{pmatrix} + \begin{pmatrix} v_1 \\ v_2 \end{pmatrix}, \quad \det \begin{pmatrix} a_{11} & a_{12} \\ a_{21} & a_{22} \end{pmatrix} \neq 0.$$

induces the action on the plane curve $\gamma(t) = (x(t), y(t))\ t \in [a, b]$. We prolong this action to integral variables up to second order. Among 6 such variables

$$\begin{aligned} X^{(ij)}(t) &= \int_a^t x(t)^i y(t)^j dx(t), \quad j \neq 0, i+j \leq 2 \\ Y^{(ij)}(t) &= \int_a^t x(t)^i y(t)^j dy(t), \quad i \neq 0, i+j \leq 2 \end{aligned} \tag{2.20}$$

we choose 3 independent: $Y^{(10)}, Y^{(11)}, X^{(11)}$.

We start by translating the initial point $\gamma(a)$ to the origin and make the corresponding substitution $X(t) = x(t) - x(a), Y(t) = y(t) - y(a)$ in the integrals. This reduces the problem to finding invariants under the $GL(2)$-action on $\mathbb{R}^5$ by prolonging the group action in $\mathbb{R}^5$ as follow:

$$\begin{aligned} \overline{X} &= a_{11}X + a_{12}Y, \qquad \overline{Y} = a_{21}X + a_{22}Y, \\ \overline{Y^{(10)}} &= (a_{11}a_{22} - a_{12}a_{21})\, Y^{(10)} + \frac{a_{11}a_{21}X^2}{2} + \frac{a_{12}a_{22}Y^2}{2} + a_{12}a_{21}XY, \\ \overline{Y^{(11)}} &= \frac{a_{11}X^3{a_{21}}^2}{3} + a_{11}a_{21}a_{22}X^2Y - a_{11}a_{22}a_{21}X^{(11)} + a_{11}{a_{22}}^2\, Y^{(11)} \\ &\quad + a_{12}{a_{21}}^2 X^{(11)} - a_{12}a_{21}a_{22}\, Y^{(11)} + a_{12}a_{22}a_{21}XY^2 + \frac{a_{12}Y^3{a_{22}}^2}{3}, \\ \overline{X^{(11)}} &= \frac{{a_{11}}^2X^3a_{21}}{3} + a_{11}a_{21}a_{12}X^2Y - a_{12}a_{21}a_{11}X^{(11)} + {a_{11}}^2a_{22}X^{(11)} \\ &\quad - a_{11}a_{22}a_{12}\, Y^{(11)} + {a_{12}}^2a_{21}\, Y^{(11)} + a_{12}a_{22}a_{11}XY^2 + \frac{{a_{12}}^2Y^3a_{22}}{3}. \end{aligned} \tag{2.21}$$

The regularization approach allows the parameters a_{11}, a_{12}, a_{21}, a_{22} to be normalized by setting

$$(\overline{X}, \overline{Y}, \overline{Y^{(10)}}, \overline{Y^{(11)}}) = (1, 1, 0, 0)$$

Solving the system of equation above, the normalized parameters follow:

$$a_{11} = \frac{4\ {Y^{(10)}}^2Y - 2\,Y^2X\,Y^{(10)} + 6\ Y^{(11)}\,XY - 6\ Y^{(11)}\ Y^{(10)} - 2\,X^2Y^3 + 3\,Y^2X^{(11)}}{(-3\ Y^{(11)}\,X + 2\,X^2Y^2 - 3\,YX^{(11)})\,(-XY + 2\ Y^{(10)})}$$

$$a_{12} = -\frac{4\ {Y^{(10)}}^2X - 6\ Y^{(10)}\,X^2Y + 6\ Y^{(10)}\,X^{(11)} + 3\ Y^{(11)}\,X^2}{(-3\ Y^{(11)}\,X + 2\,X^2Y^2 - 3\,YX^{(11)})\,(-XY + 2\ Y^{(10)})}$$

$$a_{21} = \frac{2\ Y^{(10)}\, Y - 3\ Y^{(11)}}{-3\ Y^{(11)}\, X + 2\, X^2 Y^2 - 3\, Y\, X^{(11)}}$$

$$a_{22} = -\frac{2\ Y^{(10)}\, X - 2\, X^2 Y + 3\, X^{(11)}}{-3\ Y^{(11)}\, X + 2\, X^2 Y^2 - 3\, Y\, X^{(11)}}$$

One integral invariant may be achieved by substituting the group parameters in to $\overline{X^{(11)}}$:

$$I = \frac{3\, Y\, X^{(11)} - 8\ Y10\ XY + 8\ {Y^{(10)}}^2 + 3\ Y^{(11)}\, X}{\left(XY - 2\ Y^{(10)}\right)^2} \tag{2.22}$$

The invariant above is equivalent to the one obtained in [21].

Chapter 3

First trial to extend Integral Invariant from 2D to 3D-3D Mixed Invariants

2D integral invariants, as proposed in [21], are conceptually easy to develop by simply extending the moving frame idea in the integral jet space as shown in the previous section. A natural question is if the same idea works in 3D. In this section, we provide a first attempt to develop 3D integral invariants, show the analytical difficulty which arised in a 3D integral invariant development, and propose an integro-differential solution.

3.1 A naive 3D extension of 2D integral invariant

The standard affine group action on $\mathbb{R}^3$:

$$\begin{pmatrix} \overline{x} \\ \overline{y} \\ \overline{z} \end{pmatrix} = \begin{pmatrix} a_{11} & a_{12} & a_{13} \\ a_{21} & a_{22} & a_{23} \\ a_{31} & a_{32} & a_{33} \end{pmatrix} \begin{pmatrix} x \\ y \\ z \end{pmatrix} + \begin{pmatrix} v_1 \\ v_2 \\ v_3 \end{pmatrix}, \quad \det \begin{pmatrix} a_{11} & a_{12} & a_{13} \\ a_{21} & a_{22} & a_{23} \\ a_{31} & a_{32} & a_{33} \end{pmatrix} \neq 0.$$

induces the action on a space curve $\gamma(t) = (x(t), y(t), z(t))\ t \in [a, b]$.

Three types of integral variables are defined at level l:

$$\begin{aligned} X^{(ijk)}(t) &= \int_a^t x(t)^i y(t)^j z(t)^k dx(t), \quad j+k \neq 0, i+j+k = l \\ Y^{(ijk)}(t) &= \int_a^t x(t)^i y(t)^j z(t)^k dy(t), \quad i+k \neq 0, i+j+k = l \\ Z^{(ijk)}(t) &= \int_a^t x(t)^i y(t)^j z(t)^k dz(t), \quad i+j \neq 0, i+j+k = l \end{aligned} \tag{3.1}$$

We prolong the affine group action to integral variables up to the second order. Among 21 such variables, we choose 11 independent ones:

$$Z^{(100)}, Z^{(010)}, Y^{(100)}, Z^{(011)}, Z^{(020)}, Z^{(101)}, Z^{(110)}, Y^{(101)}, X^{(110)}, X^{(101)}, X^{(020)}.$$

The rest of the invariants may be expressed in terms of above by way of the integration by parts. We translate the initial point $\gamma(a)$ to the origin and make the corresponding substitution $X(t) = x(t) - x(a), Y(t) = y(t) - y(a), Z(t) = z(t) - z(a)$ in the integrals. This reduces the problem to computing $GL(3)$-invariants.

The integral jet space is constructed as:

$$(X, Y, Z, Z^{(100)}, Z^{(010)}, Y^{(100)}, Z^{(011)}, Z^{(020)}, Z^{(101)}, Z^{(110)}, Y^{(101)}, X^{(110)}, X^{(101)}, X^{(020)})$$

The next step is to prolong the group action to the integral jet space:

$$
\begin{aligned}
\overline{X} &= a_{11}X + a_{12}Y + a_{13}Z, \\
\overline{Y} &= a_{21}X + a_{22}Y + a_{23}Z, \\
\overline{Z} &= a_{31}X + a_{32}Y + a_{33}Z, \\
\overline{Z^{(100)}} &= \frac{a_{11}a_{31}X^2}{2} + a_{12}a_{31}XY - a_{12}a_{31}\,Y^{(100)} + a_{13}a_{31}XZ - a_{13}a_{31}Z^{(100)} \\
&\quad + a_{11}a_{32}\,Y^{(100)} + \frac{a_{12}a_{32}Y^2}{2} + a_{13}a_{32}YZ - a_{13}a_{32}Z^{(010)} + a_{11}a_{33}Z^{(100)} \\
&\quad + a_{12}a_{33}Z^{(010)} + \frac{a_{13}a_{33}Z^2}{2} \\
\overline{Z^{(010)}} &= \frac{a_{21}a_{31}X^2}{2} + a_{22}a_{31}XY - a_{22}a_{31}\,Y^{(100)} + a_{23}a_{31}XZ - a_{23}a_{31}Z^{(100)} \\
&\quad + a_{21}a_{32}\,Y^{(100)} + \frac{a_{22}a_{32}Y^2}{2} + a_{23}a_{32}YZ - a_{23}a_{32}Z^{(010)} + a_{21}a_{33}Z^{(100)} \\
&\quad + a_{22}a_{33}Z^{(010)} + \frac{a_{23}a_{33}Z^2}{2}, \\
\overline{Y^{(100)}} &= \frac{a_{11}a_{21}X^2}{2} + a_{12}a_{21}XY - a_{12}a_{21}\,Y^{(100)} + a_{13}a_{21}XZ - a_{13}a_{21}Z^{(100)} \\
&\quad + a_{11}a_{22}\,Y^{(100)} + \frac{a_{12}a_{22}Y^2}{2} + a_{13}a_{22}YZ - a_{13}a_{32}Z^{(010)} + a_{11}a_{23}Z^{(100)} \\
&\quad + a_{12}a_{23}Z^{(010)} + \frac{a_{13}a_{23}Z^2}{2}, \\
\overline{Z^{(011)}} &= -\frac{1}{2}{a_{32}}^2a_{21}X^{(020)} + a_{33}a_{21}a_{31}X^2Z + \frac{1}{3}{a_{32}}^2a_{22}Y^3 + {a_{33}}^2a_{21}Z^{(101)} \\
&\quad + {a_{31}}^2a_{22}X^{(110)} + {a_{33}}^2a_{22}Z^{(011)} + \frac{1}{3}{a_{31}}^2a_{21}X^3 - a_{31}a_{21}a_{33}X^{(101)} \\
&\quad + \frac{1}{3}{a_{33}}^2a_{23}Z^3 + {a_{31}}^2a_{23}X^{(101)} - \frac{1}{2}{a_{32}}^2a_{23}Z^{(020)} + \frac{1}{2}a_{32}a_{22}a_{31}XY^2 \\
&\quad + a_{31}a_{22}a_{33}XYZ - a_{33}a_{23}a_{32}Z^{(011)} + a_{31}a_{23}a_{32}XYZ - a_{31}a_{22}a_{33}\,Y^{(101)} \\
&\quad + \frac{1}{2}{a_{32}}^2a_{23}Y^2Z + \frac{1}{2}a_{33}a_{22}a_{32}Z^{(020)} - a_{33}a_{23}a_{31}Z^{(101)} + \frac{1}{2}{a_{32}}^2a_{21}XY^2 \\
&\quad + a_{31}a_{23}a_{33}XZ^2 - a_{31}a_{23}a_{32}Z^{(110)} + \frac{1}{2}a_{31}a_{22}a_{32}X^{(020)} + a_{32}a_{21}a_{33}\,Y^{(101)} \\
&\quad + \frac{1}{2}a_{32}a_{22}a_{33}Y^2Z - a_{31}a_{21}a_{32}X^{(110)} + a_{33}a_{21}a_{32}Z^{(110)} + a_{32}a_{23}a_{33}YZ^2 \\
&\quad + a_{32}a_{21}a_{31}X^2Y
\end{aligned}
$$

$$
\begin{aligned}
\overline{X^{(110)}} \;=\; & \frac{1}{2}{a_{12}}^2 a_{23} Y^2 Z + a_{11} a_{12} a_{23} XYZ + {a_{13}}^2 a_{22} Z^{(011)} - a_{11} a_{13} a_{21} X^{(101)} \\
& + \frac{1}{2} a_{12} a_{11} a_{22} XY^2 - a_{11} a_{12} a_{23} Z^{(110)} + {a_{11}}^2 a_{23} X^{(101)} + a_{12} a_{13} a_{21}\, Y^{(101)} \\
& + \frac{1}{2} a_{11} a_{12} a_{22} X^{(020)} - \frac{1}{2}{a_{12}}^2 a_{23} Z^{(020)} + a_{13} a_{11} a_{21} X^2 Z + \frac{1}{3}{a_{12}}^2 Y^3 a_{22} \\
& + \frac{1}{3}{a_{13}}^2 Z^3 a_{23} + a_{11} a_{13} a_{22} XYZ + \frac{1}{3}{a_{11}}^2 a_{21} X^3 - a_{11} a_{12} a_{21} X^{(110)} \\
& + a_{11} a_{13} a_{23} XZ^2 + \frac{1}{2}{a_{12}}^2 a_{21} XY^2 - a_{11} a_{13} a_{22}\, Y^{(101)} + {a_{11}}^2 a_{22} X^{(110)} \\
& + \frac{1}{2} a_{13} a_{12} a_{22} Z^{(020)} + \frac{1}{2} a_{12} a_{13} a_{22} Y^2 Z + {a_{13}}^2 a_{21} Z^{(101)} + a_{13} a_{12} a_{21} Z^{(110)} \\
& - \frac{1}{2}{a_{12}}^2 a_{21} X^{(020)} - a_{13} a_{12} a_{23} Z^{(011)} - a_{13} a_{11} a_{23} Z^{(101)} \\
& + a_{12} a_{11} a_{21} X^2 Y + a_{12} a_{13} a_{23} YZ^2,
\end{aligned}
$$

$$
\begin{aligned}
\overline{Z^{(020)}} \;=\; & -a_{32} a_{21} a_{22} X^{(020)} - 2\, a_{33} {a_{21}}^2 X^{(101)} - 2\, a_{32} {a_{21}}^2 X^{(110)} - 2\, a_{31} a_{22} a_{23} Z^{(110)} \\
& + a_{32} a_{22} a_{23} Y^2 Z + 2\, a_{33} a_{21} a_{23} Z^{(101)} + 2\, a_{31} a_{23} a_{21} X^{(101)} - a_{32} a_{22} a_{23} Z^{(020)} \\
& + \frac{1}{3} a_{32} {a_{22}}^2 Y^3 + a_{33} {a_{21}}^2 X^2 Z + 2\, a_{32} a_{21} a_{23}\, Y^{(101)} + 2\, a_{31} a_{22} a_{23} XYZ \\
& + a_{33} {a_{22}}^2 Z^{(020)} + \frac{1}{3} a_{31} {a_{21}}^2 X^3 + 2\, a_{33} a_{21} a_{22} Z^{(110)} - 2\, a_{32} {a_{23}}^2 Z^{(011)} \\
& + 2\, a_{31} a_{22} a_{21} X^{(110)} - 2\, a_{31} {a_{23}}^2 Z^{(101)} + a_{32} {a_{23}}^2 Y Z^2 + \frac{1}{3} a_{33} {a_{23}}^2 Z^3 \\
& + a_{31} {a_{23}}^2 X Z^2 + 2\, a_{33} a_{23} a_{22} Z^{(011)} + a_{32} {a_{21}}^2 X^2 Y + a_{32} a_{21} a_{22} XY^2 \\
& + a_{31} {a_{22}}^2 X^{(020)} - 2\, a_{31} a_{22} a_{23}\, Y^{(101)}
\end{aligned}
\tag{3.2}
$$

We may set:

$$
\big(\overline{X}, \overline{Y}, \overline{Z}, \overline{Z^{(100)}}, \overline{Z^{(010)}}, \overline{Y^{(100)}}, \overline{Z^{(011)}}, \overline{X^{(010)}}, \overline{Z^{(020)}}\big) = \big(c_1, c_2, c_3, c_4, c_5, c_5, c_6, c_7, c_8, c_9\big),
$$

where c_i's may be any constant. In theory, we may solve the above system of equations to get the group parameters (a_{ij}) in order to calculate 3D integral invariants. The system of equations, being so highly nonlinear, complicates its solution. Solving the resulting system for all group parameters in this space, and in fact quickly becomes intractable.The difficulty encountered even using Maple and Mathematica quickly indicates that such a direct approach is unusable.

3.2 A practical solution-mixed invariant

As indicated in [13][26], while a differential invariant is achievable, the higher order derivatives(up to 6^{th}) present a serious numerical challenge. Upon accounting for all the constraints, a tradeoff between the computational complexity of solving the system of equations to obtain an integral invariant, and the numerical sensitivity to noise of computing differential invariants, we propose a hybrid invariant which utilizes lower order(first order) derivatives and integral auxiliary variables. The solution of such a system equations dramatically simplifies, and the use of only first order derivatives greatly improve the noise sensitivity.

To that end, we define,

$$Y' = \frac{dY}{dX}, Z' = \frac{dZ}{dX},$$

to in turn specify the jet space as a Euclidean space with coordinates,

$$(X, Y, Z, Z^{(100)}, Z^{(010)}, Y^{(100)}, Z^{(011)}, Z^{(020)}, Z^{(101)}, Z^{(110)}, Y^{(101)}, X^{(110)}, X^{(101)},$$

$$X^{(020)}, Y', Z')$$

By prolonging the group action onto the new mixed jet space, we achieve:

$$\overline{Y'} = \frac{a_{21}X' + a_{22}Y' + a_{23}Z'}{a_{11}X' + a_{12}Y' + a_{13}Z'}$$

$$\overline{Z'} = \frac{a_{31}X' + a_{32}Y' + a_{33}Z'}{a_{11}X' + a_{12}Y' + a_{13}Z'}$$

The two equations above are much simpler than the second and third order prolonged integral variables. By replace two complicated third order equations ($\overline{Z^{(011)}}$ $\overline{Z^{(020)}}$)with $\overline{Y'}$ and $\overline{Z'}$, the complexity of the system of equation will be dramatically dropped since only one third order equation is present.

Set

$$(\overline{X}, \overline{Y}, \overline{Z}, \overline{Z^{(100)}}, \overline{Z^{(010)}}, \overline{Y^{(100)}}, \overline{Y'}, \overline{Z'}, \overline{X^{(110)}}) = (0, 0, 1, 1, 1, 1, 1, 1, 0),$$

to obtain a solution of the corresponding system of equations for

$$(a_{11}, a_{12}, a_{13}, a_{21}, a_{22}, a_{23}, a_{31}, a_{32}, a_{33}),$$

which are used in the invariants,

$$
\begin{aligned}
a_{11} &= (6\,ZY^{(011)}X - 6\,ZX^{(011)}Y + 6\,YZ^{(011)}X + 3\,Z^2X^{(020)} + 3\,Y^2X^{(002)} \\
&\quad -4\,Z^2XY^2)n_4/((n_1+n_2)n_3) \\
a_{12} &= (3\,XX^{(002)}Y + 6\,X^{(110)}Z^2 + 6\,XY^{(101)}Z - 6\,X^{(101)}YZ - 5\,X^2YZ^2 \\
&\quad +6\,X^2Z^{(011)})n_4/((n_1+n_2)n_3) \\
a_{13} &= (X^2Y^2Z - 6\,X^{(110)}YZ + 6\,Y^{(011)}X^2 + 3\,XX^{(020)}Z + 6\,X^{(101)}Y^2 \\
&\quad -6\,X^{(011)}XY - 6\,Y^{(101)}XY)n_4/((n_1+n_2)n_3) \\
a_{31} &= (Y^2Z^2 - 4\,Y^2Y^{(001)}Z'\,X^{(001)} - Y^2XY^{(001)}Z'\,Z + 2\,YZX^{(010)}Y^{(001)}Z' \\
&\quad +2\,YXY^{(001)}Z'\,Y^{(001)} - 4\,YZY^{(001)} + YZ^2Y^{(001)}Y'\,X \\
&\quad +6\,Y^{(001)}Y'\,X^{(001)}YZ + 4\,X^{(010)}Y^{(001)}Z'\,Y^{(001)} + 4\,{Y^{(001)}}^2 \\
&\quad -2\,Y^{(001)}Y^{(001)}Y'\,ZX - 4\,Y^{(001)}Y'\,X^{(001)}Y^{(001)} \\
&\quad -4\,Y^{(001)}Y'\,Z^2X^{(010)})/(n_3n_4) \\
a_{32} &= (X^2Y^{(001)}Z'\,YZ + 6\,X^{(001)}Y^{(001)}Z'\,YX - 2\,X^{(001)}YZ - 3\,YZ^2X \\
&\quad -4\,Y^{(001)}X^2Y^{(001)}Z' - 4\,Y^{(001)}Z'\,X^{(001)}X^{(010)} - 2\,X^{(010)}XY^{(001)}Z'\,Z \\
&\quad +6\,Y^{(001)}ZX + 4\,X^{(010)}Z^2 - 4\,XX^{(001)}Y^{(001)}Y'\,Z \\
&\quad -4\,X^{(001)}Y^{(001)} + 4\,{X^{(001)}}^2Y^{(001)}Y' + Y^{(001)}Y'\,Z^2X^2)/(n_3n_4) \\
a_{33} &= (X^2Y^{(001)}Z'\,Y^2 - 3\,X^2Y^{(001)}Y'\,YZ + 4\,X^2Y^{(001)}Y^{(001)}Y' \\
&\quad -4\,XYY^{(001)}Z'\,X^{(010)} + 3\,XY^2Z + 6\,XX^{(010)}Y^{(001)}Y'\,Z - 6\,XYY^{(001)} \\
&\quad -2\,XYX^{(001)}Y^{(001)}Y' + 4\,{X^{(010)}}^2Y^{(001)}Z' - 6\,X^{(010)}ZY \\
&\quad +4\,X^{(001)}Y^2 + 4\,X^{(010)}Y^{(001)} - 4\,Y^{(001)}Y'\,X^{(001)}X^{(010)})/(n_3n_4)
\end{aligned}
$$

$$
\begin{aligned}
n_1 &= -3\,XY^{(001)}Z'\,ZX^{(020)} + 3\,Z^2X^{(020)} - X^2Y^{(001)}Z'\,ZY^2 + 6\,ZY^{(011)}X \\
&\quad +6\,Y^{(001)}Y'\,ZZ' - 6\,Y^{(001)}Z'\,X^{(101)}Y^2 + 3\,Y^2X^{(002)} - 6\,X^2Y^{(001)}Z'\,Y^{(011)} \\
&\quad +6\,XY^{(001)}Z'\,Y^{(101)}Y + 6\,XY^{(001)}Z'\,X^{(011)}Y \\
n_2 &= 5\,Y^{(001)}Y'\,Z^2X^2Y - 3\,Y^{(001)}Y'\,XX^{(002)}Y - 6\,ZX^{(011)}Y \\
&\quad -6\,Y^{(001)}Y'\,Z^2X^{(110)} - 4\,Z^2XY^2 + 6\,YZ^{(011)}X - 6\,Y^{(001)}Y'\,ZXY^{(101)} \\
&\quad +6\,Y^{(001)}Z'\,ZX^{(110)}Y - 6\,Y^{(001)}Y'\,X^2Z^{(011)} \\
n_3 &= XYZ - 2\,Y^{(001)}X + 2\,X^{(001)}Y - 2\,X^{(010)}Z \\
n_4 &= 2\,Y^{(001)}Y'\,X^{(001)} + YXY^{(001)}Z' + YZ - 2\,X^{(010)}Y^{(001)}Z' - 2\,Y^{(001)} \\
&\quad -Y^{(001)}Y'\,ZX,
\end{aligned}
$$

which may be directly used to define our desired 3D affine invariant as:

$$
\begin{aligned}
\overline{X^{(002)}} &= a_{11}(\frac{1}{3}\,{a_{31}}^2X^3 + {a_{32}}^2X^{(020)} + {a_{33}}^2X^{(002)} + 2\,a_{31}a_{32}X^{(110)} + 2\,a_{31}a_{33}X^{(101)} \\
&+ 2\,a_{32}a_{33}X^{(011)}) + a_{12}({a_{31}}^2\left(X^2Y - 2\,X^{(110)}\right) + \frac{1}{3}\,{a_{32}}^2Y^3 \\
&+ {a_{33}}^2\left(YZ^2 - 2\,Z^{(011)}\right) + a_{31}a_{32}\left(XY^2 - X^{(020)}\right) + 2\,a_{31}a_{33}Y^{(101)} \\
&+ 2\,a_{32}a_{33}Y^{(011)}) + a_{13}({a_{31}}^2\left(X^2Z - 2\,X^{(101)}\right) + {a_{32}}^2\left(Y^2Z - 2\,Y^{(011)}\right) \\
&+ 1/3\,{a_{33}}^2Z^3 + 2\,a_{31}a_{32}\left(XYZ - Y^{(101)} - X^{(011)}\right) \\
&+ a_{31}a_{33}\left(XZ^2 - X^{(002)}\right) + 2\,a_{32}a_{33}Z^{(011)})
\end{aligned}
$$

3.2.1 An example

Consider two 3D spatial curves Fig. 6.6-a ($\beta(t) = (\sin t - 1/5\,\cos^2 t + 1/5,\ 1/2\,\sin t - \cos t + 1, \sin^2 t + \cos t - 1)$,)and Fig. 6.6-b for comparison. Fig. 6.6-b is related to Fig. 6.6-a by a full affine transformation $\begin{pmatrix} 1 & 2 & 3 \\ 4 & 6 & 6 \\ 9 & 8 & 7 \end{pmatrix}$. Since the invariant is a ratio derived as shown in section above, a zero denominator will yield an infinite invariant.

To better visualize local features which are important for comparison, we selectively remove all numerical instability due to these effects to result in the invariants shown in Fig. 3.2. It is clear that no obvious deviation between the two invariants can be detected.

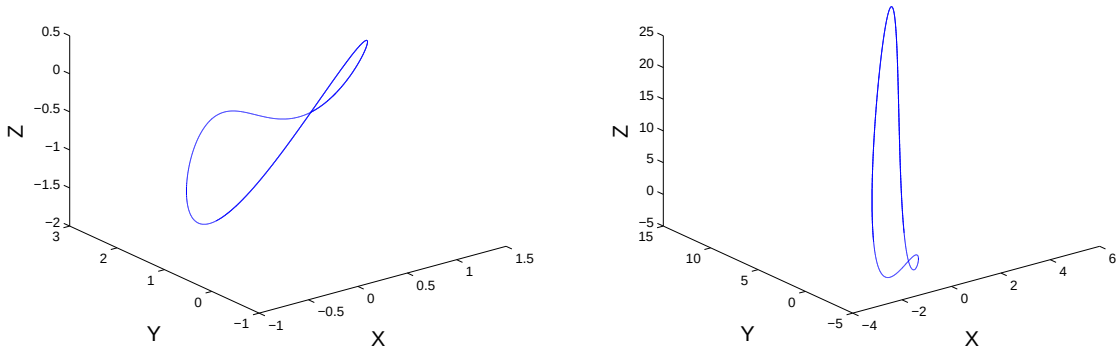

(a) (b)

Figure 3.1: (a)3D curve 1(b)3D curve 2

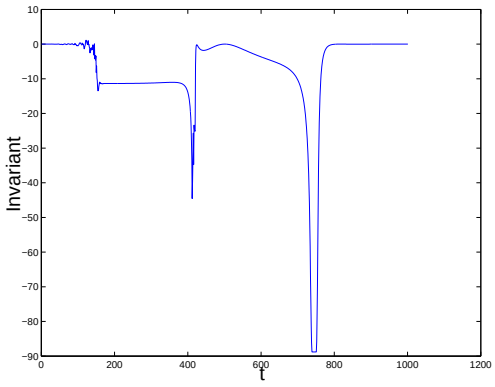

Figure 3.2: the mixed invariant for curves 1 and 2

The appeal of our proposed approach is in representing a 3D curve curve which is subjected to an affine transformation by a 2D invariant. Such problems arise in biometrics [18], where such a technique was successfully adapted. One may contrast this approach to fourier descriptors or moment invariants, as our proposed technique is a one-to-one mapping of the local feature. A direct application of this technique in

3D object clustering, is discussed next to demonstrate the robustness of this mixed invariant.

3.3 Robustness analysis

Tasks of comparing curves arise in many applications and using their invariants expedites the test for their similarity, even when subjected to affine transformations. In the present example, we consider applications such as classifications of 3D objects based on a set of characteristic spatial curves.

3.3.1 Experimental design

The Princeton Shape Benchmark[44] provides a repository of 3D models. We select a subset of four models as shown in Fig. 3.3. We may assume that the characteristic curves [2] (which will be explained later in Chapter 7.2) have already been extracted from 3D models in Princeton Shape Benchmark, as shown in Fig. 3.4. There are a total of 50 characteristic curves, and each of them are re-sampled to 5000 points. Apply 10 randomly generated 3D affine transformations to these curves, and 10 variations for each curve are generated (Fig. 3.5)[1]. The problem is to classify all of these curves. To make this problem even more challenging and to illustrate the noise sensitivity, gaussian noise with distribution $N(0, \sigma^2)$ is added to each of the variations.

A baseline differential invariant as proposed in [26] and the proposed mixed invariant are implemented. The discrimination power and sensitivity to noise are analyzed using the error rate of classification. Two sets are required for classification purpose, namely a training set and a classification set. The training set is obtained by randomly selecting three variations out of ten from each characteristic curve. The 7 left for each characteristic curve automatically form the testing set. Such a classifier is implemented as a Nearest Neighbor (NN) Classifier in a Euclidean Space using a L^2 distance as a metric.

[1] These curves would undergo such transformations when the 3D object is subjected to a transformation.

Figure 3.3: 3D models from The Princeton Shape Benchmark(Best visualized in color)

Table 3.1: error rate for mixed invariant

	Mixed Invariant	Differential Invariant
$\sigma = 0.1$	0.0971	0.6086
$\sigma = 1$	0.1829	0.7314

3.3.2 Experimental results

Two experiments are carried out with different noise variance, namely $\sigma = 0.1$ and $\sigma = 1$. The error rates of the two sigma settings are shown in Table.I.

Due to higher order derivative terms presents in differential invariants, the classification error rates which result render these practically useless. On the other hand, the mixed invariants with a fist order derivative dramatically reduce the classification error rate from 60% to 10%. The presence of the first order derivatives in the Mixed Invariant, results in a modest increase of error rate as the noise variance is increased by an order of magnitude.

A direct and straightforward elaboration of the moving frame approach clearly turns into analytical difficulties, and we show in the next chapter that some of the difficulty may be alleviated by cleverly rewriting the transformation matrix.

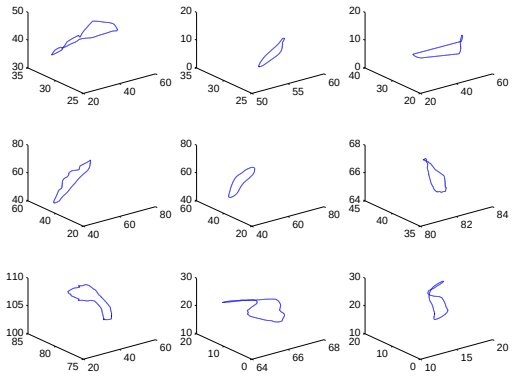

Figure 3.4: 3D spatial feature curves

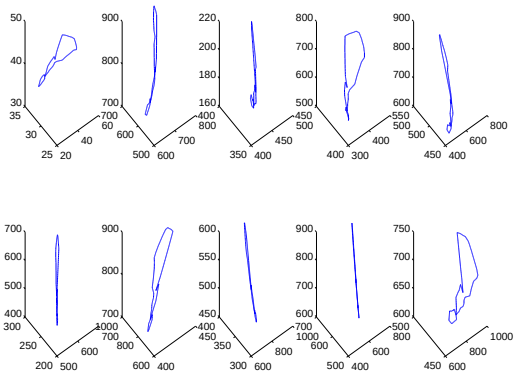

Figure 3.5: 10 variations of a curve under affine transformation

Chapter 4

An alternative approach: inductive construction of moving frames

The direct approach to derive 3D integral invariants was not successful on account of due to the complexity of solving the system of equations. The mixed invariant was proposed as a compromise solution in the last chapter. While a performance improvement over classical differential invariants is obtained, the presence of first order derivatives still affect the overall performance. Our ultimate goal is still to find integral invariants with no differential variables. To that end, an alternative approach is in order. Specifically exploiting an inductive implementation of the moving frame construction, proposed by Kogan [26], we can dramatically simplify algebraic derivations, by constructing invariants for the entire group from invariants of its subgroups: in our case affine invariants may be obtained in terms of Euclidean ones.

We will briefly discuss the inductive approach in this chapter, and reinterpret the 2D integral invariants by the inductive approach to illustrate how it works. A more intuitive geometric meaning of the each 2D integral invariant is provided.

4.1 Inductive approach

It is well known that the moving frame method works well for groups with a small number of group parameters, such as 2D affine group, 3D Euclidean group etc. As the

number of group parameters increases, the practical implementation becomes difficult as we showed in Chapter 3 for the 3D affine group.

Since the high dimensional groups are difficult to tackle, the natural intuition is to use a divide and conquer method, such as dividing the high dimensional group into some low dimensional subgroups, and the implementation of the moving frame method for each subgroup may be much simpler. A systematic algorithm of inductive construction of moving frames is introduced and proved in [26]. The invariants of a group may be found by exploring the invariants of its subgroups using the moving frame method. The algorithm proceeds as follows:

1. Decompose the high dimensional group

In order to simplify the invariant development procedure, a high dimensional group G should be decomposed into the product of two subgroup A and B

$$G = AB, A \cap B = \phi$$

So for each element $g \in G$, there must exist $a \in A$ and $b \in B$ to satisfy $g = ab$.

As an example, a 2D affine group may be written as a product of a Euclidean group and a group featured by an upper triangular matrix.

2. Calculate invariants for group A by the moving frame method

The procedure in this step is very similar to what we discussed in Chapter 2: define a transformation, construct a "jet" space, prolong the group action to the jet space, solve the system of equations to get all group parameters, and obtain invariants in the prolonged variables used resulting group parameters.

The difference with Chapter 2, where arbitrary constants for the system equations were chosen to achieve a solution, is the latters have to be preserved when passing from group A to the action of group B.

3. Calculate invariants for group B by the moving frame method

The procedure in this step is also very similar as what we discussed in chapter 2. In this stage, the constant selection is exactly the same as chapter 2, which is arbitrarily, but the jet space is constructed differently. Instead o using the variables in the jet space in stage 2, we prolong the action of group A on them, and the

prolonged variables are used to construct the jet space. The invariants we achieve in this stage are invariant to group B. Since each of the variables in the jet space are are invariant to group A, we actually achieve the invariants for group $G = AB$.

A example is given in next section to shown how this algorithm works.

4.2 An example: reinterpreting 2D integral invariants

4.2.1 Integral Affine invariants for 2D curves.

The standard affine group action on $\mathbb{R}^2$,

$$\begin{pmatrix} \overline{x} \\ \overline{y} \end{pmatrix} = \begin{pmatrix} a_{11} & a_{12} \\ a_{21} & a_{22} \end{pmatrix} \begin{pmatrix} x \\ y \end{pmatrix} + \begin{pmatrix} v_1 \\ v_2 \end{pmatrix}, \quad \det \begin{pmatrix} a_{11} & a_{12} \\ a_{21} & a_{22} \end{pmatrix} \neq 0.$$

induces the action on the plane curves $\gamma(t) = (x(t), y(t))\ t \in [a, b]$. Proceeding similarly to Chapter 2, we prolong this action to integral variables up to third order. Among 12 such variables

$$\begin{aligned} X^{(ij)}(t) &= \int_a^t x(t)^i y(t)^j dx(t), \quad j \neq 0, i + j \leq 3 \\ Y^{(ij)}(t) &= \int_a^t x(t)^i y(t)^j dy(t), \quad i \neq 0, i + j \leq 3 \end{aligned} \tag{4.1}$$

we choose 6 independent: $Y^{(10)}, Y^{(11)}, X^{(11)}, Y^{(12)}, Y^{(21)}, X^{(21)}$, and construct the integral jet space:

$$(X, Y, Y^{(10)}, Y^{(11)}, X^{(11)}, Y^{(12)}, Y^{(21)}, X^{(21)}).$$

We start by translating the initial point $\gamma(a)$ to the origin with a corresponding substitution $X(t) = x(t) - x(a), Y(t) = y(t) - y(a)$ in the integrals. This reduces the

problem to finding invariants under the following $GL(2)$-action on $\mathbb{R}^8$.

$$
\begin{aligned}
\overline{X} &= a_{11}X + a_{12}Y, \qquad \overline{Y} = a_{21}X + a_{22}Y, \\
\overline{Y^{(10)}} &= Y^{(10)} + a_{11}a_{21}\frac{X^2}{2} + \frac{1}{2}a_{12}a_{22}Y^2 + \frac{1}{2}a_{12}a_{21}XY, \\
\overline{Y^{(11)}} &= a_{22}Y^{(11)} - a_{21}X^{(11)} + \frac{1}{3}{a_{21}}^2a_{11}X^3 + a_{22}a_{11}a_{21}X^2Y - a_{21}a_{12}a_{22}XY^2 \\
&\quad + \frac{1}{3}{a_{22}}^2a_{12}Y^3, \\
\overline{X^{(11)}} &= a_{11}X^{(11)} - a_{12}Y^{(11)} + a_{11}a_{12}a_{22}XY^2 + \frac{1}{3}{a_{11}}^2a_{21}X^3 + a_{12}a_{11}a_{21}X^2Y \\
&\quad + \frac{1}{3}{a_{12}}^2a_{22}Y^3, \\
\overline{Y^{(12)}} &= \frac{1}{4}a_{11}X^4{a_{21}}^3 + a_{11}\,Y^{(30)}\,{a_{21}}^2a_{22} + 2\,a_{11}X^{(21)}\,{a_{21}}^2a_{22} + 2\,a_{11}\,Y^{(21)}\,a_{21}{a_{22}}^2 \\
&\quad + a_{11}X^{(12)}\,{a_{22}}^2a_{21} + a_{11}\,Y^{(12)}\,{a_{22}}^3 + a_{12}X^{(21)}\,{a_{21}}^3 + a_{12}\,Y^{(21)}\,{a_{21}}^2a_{22} \\
&\quad + 2\,a_{12}X^{(12)}\,{a_{21}}^2a_{22} + 2\,a_{12}\,Y^{(12)}\,a_{21}{a_{22}}^2 + a_{12}X^{(03)}\,{a_{22}}^2a_{21} + \frac{1}{4}a_{12}Y^4{a_{22}}^3, \\
\overline{Y^{(21)}} &= \frac{1}{4}{a_{11}}^2X^4{a_{21}}^2 + {a_{11}}^2\,Y^{(30)}\,a_{21}a_{22} + {a_{11}}^2X^{(21)}\,a_{22}a_{21} + {a_{11}}^2\,Y21\,{a_{22}}^2 \\
&\quad + 2\,a_{11}X^{(21)}\,a_{12}{a_{21}}^2 + 2\,a_{11}\,Y^{(21)}\,a_{12}a_{21}a_{22} + 2\,a_{11}X^{(12)}\,a_{12}a_{22}a_{21} \\
&\quad + 2\,a_{11}\,Y^{(12)}\,a_{12}{a_{22}}^2 + {a_{12}}^2X^{(12)}\,{a_{21}}^2 + {a_{12}}^2\,Y^{(12)}\,a_{21}a_{22} \\
&\quad + {a_{12}}^2X^{(03)}\,a_{22}a_{21} + \frac{1}{4}{a_{12}}^2Y^4{a_{22}}^2, \\
\overline{X^{(21)}} &= \frac{1}{4}{a_{11}}^3X^4a_{21} + {a_{11}}^2\,Y^{(30)}\,a_{21}a_{12} + {a_{11}}^3X^{(21)}\,a_{22} + {a_{11}}^2\,Y^{(21)}\,a_{22}a_{12} \\
&\quad + 2\,{a_{11}}^2X^{(21)}\,a_{12}a_{21} + 2\,a_{11}\,Y^{(21)}\,{a_{12}}^2a_{21} + 2\,{a_{11}}^2X^{(12)}\,a_{12}a_{22} \\
&\quad + 2\,a_{11}\,Y^{(12)}\,{a_{12}}^2a_{22} + {a_{12}}^2X^{(12)}\,a_{21}a_{11} + {a_{12}}^3\,Y^{(12)}\,a_{21} \\
&\quad + {a_{12}}^2X^{(03)}\,a_{22}a_{11} + 1/4\,{a_{12}}^3Y^4a_{22}. \qquad (4.2)
\end{aligned}
$$

By defining an invariant for $SL(2)$, an invariant for $GL(2)$ may simply be obtained as a ratio of two $SL(2)$ invariants

$SL(2)$ may be decomposed as a product $SL(2) = B \cdot A$, where

$B = \left\{ \begin{pmatrix} b_{11} & b_{12} \\ 0 & \frac{1}{b_{22}} \end{pmatrix} | b_{11} > 0 \right\}$ and $A = SO(2)$ is a group of rotations. The intersection $B \cap A = \phi$.

Following the inductive method, we are now focusing on the subgroup $\mathcal{S}O(2)$ of

rotation matrices, and trying to derive invariants for it. 2D rotation matrix is defined as:

$$\mathbf{A} = \begin{pmatrix} \cos\phi & \sin\phi \\ \sin\phi & \cos\phi \end{pmatrix}$$

The action of the SO(2) group may be prolonged into the integral jet space by simply setting $a_{11} = \cos\phi, a_{12} = -\sin\phi, a_{21} = \sin\phi, a_{22} = \cos\phi$. Since we only have one parameter, we may pick $Y = 0, X > 0$ serves as a cross-section, which is:

$$Y_{SE} = \sin\phi\, X + \cos\phi\, Y = 0$$

$$X_{SE} = \cos\phi\, X - \sin\phi\, Y > 0$$

The solution is

$$\cos\phi = \frac{X}{\sqrt{X^2+Y^2}}, \sin\phi = \frac{Y}{\sqrt{X^2+Y^2}}$$

The invariants for $SO(2)$ are achieved by replacing the group parameter above in the prolonged space as:

$$\begin{aligned}
X_{\mathcal{S}E} &= \sqrt{X^2+Y^2}, \quad Y^{(10)}_{\mathcal{S}E} = Y_{(\mathcal{S}E)} - \frac{XY}{2}, \\
Y^{(11)}_{\mathcal{S}E} &= -\frac{2\,Y^2X^2 - 3\,XY^{(11)} - 3\,YX^{(11)}}{3\sqrt{X^2+Y^2}}, \\
X^{(11)}_{\mathcal{S}E} &= -\frac{YX^3 - 3\,XX^{(11)} - XY^3 + 3\,YY^{(11)}}{3\sqrt{X^2+Y^2}}, \\
Y^{(12)}_{\mathcal{S}E} &= , \frac{1}{4}\,\frac{Y^3X^3 + 4\,Y^{(12)}\,X^2 - 4\,Y^{(21)}\,YX - 4\,X^{(21)}\,Y^2}{X^2+Y^2}, \\
Y^{(21)}_{\mathcal{S}E} &= \frac{1}{4}\,\frac{4\,X^6Y - 12\,X^3X^{(21)} + 4\,X^2YY^{(21)} - 4\,XY^2Y^{(12)} - Y^7}{\left(X^2+Y^2\right)^{3/2}}, \\
X^{(21)}_{\mathcal{S}E} &= \frac{1}{4}\,\frac{X^7 + 4\,X^2X^{(21)}\,Y - 2\,X^3Y^4 + 4\,XY^2Y^{(21)} - 4\,Y^6X + 12\,Y^3Y^{(12)}}{\left(X^2+Y^2\right)^{3/2}}.
\end{aligned} \tag{4.3}$$

We notice that since denominators of $Y^{(11)}_{\mathcal{S}E}$ and $X^{(11)}_{\mathcal{S}E}$ are invariant, so are their numerators.

Our next step is to seek invariants for the group B affected by a transformation matrix$\left\{ \begin{pmatrix} b_{11} & b_{12} \\ 0 & \frac{1}{b_{22}} \end{pmatrix} | b_{11} > 0 \right\}$. At this stage, the jet space is:

$$(X_{SE}, Y_{SE}, Y_{SE}^{(10)}, Y_{SE}^{(11)}, X_{SE}^{(11)}, Y_{SE}^{(12)}, Y_{SE}^{(21)}, X_{SE}^{(21)}).$$

Prolonging the group action may be simply carried out by setting

$$a_{11} = b_{11}, a_{12} = b_{12}, a_{21} = 0, a_{22} = \frac{1}{b_{11}}$$

We notice that the cross section($Y_{SE} = 0$) in the previous section is preserved since $Y_{SA} = 0$ after the transformation.

Since we have two parameters, the cross section may be chosen as: $X_{SE} = 1, X_{SE}^{(11)} = 0$, which is prolonged as:

$$X_{SA} = b_{11} X_{SE} = 1$$

$$X_{SA}^{(11)} = b_{11} X_{11SE} - b_{12} Y_{11SE} = 0$$

The solution follows as:

$$b_{11} = \frac{1}{X_{SE}}, b_{12} = \frac{X_{11SE}}{X_{SE} Y_{11SE}}.$$

The integral invariants for group B are:

$$\begin{aligned}
Y_{\mathcal{S}A}^{(10)} &= Y_{\mathcal{S}E}^{(10)}, \\
Y_{\mathcal{S}A}^{(11)} &= X_{\mathcal{S}E} Y_{\mathcal{S}E}^{(11)}, \\
Y_{\mathcal{S}A}^{(12)} &= Y_{\mathcal{S}E}^{(12)} X_{SE}^2, \\
Y_{\mathcal{S}A}^{(21)} &= \frac{Y_{SE}^{(21)} Y_{SE}^{(11)} + 2 X_{SE}^{(11)} Y_{SE}^{(12)}}{Y_{SE}^{(11)} X_{SE}}, \\
X_{\mathcal{S}A}^{(21)} &= \frac{X_{SE}^{(21)} {Y_{SE}^{(11)}}^2 + 2 X_{SE}^{(12)} X_{SE}^{(11)} Y_{SE}^{(11)} - 3 {X_{SE}^{(11)}}^2 Y_{SE}^{(12)}}{{Y_{SE}^{(11)}}^2 S_{SE}},
\end{aligned} \tag{4.4}$$

The full special affine integral invariants are achieved by replacing all of the variable in Eq. 4.5 with those in Eq. 4.4 to result in three invariants which are useful later.

$$\begin{aligned} Y_{\mathcal{SA}}^{(10)} &= Y_{\mathcal{SE}}^{(10)} = Y^{(10)} - \frac{XY}{2}, \\ Y_{\mathcal{SA}}^{(11)} &= X_{\mathcal{SE}} Y_{\mathcal{SE}}^{(11)} = X\,Y^{(11)} + Y\,X^{(11)} - \frac{2}{3}\,Y^2X^2, \\ Y_{\mathcal{SA}}^{(12)} &= Y_{\mathcal{SE}}^{(12)} X_{SE}^2 = X^2\,Y^{(12)} - XY\,Y^{(21)} - Y^2\,X^{(21)} + \frac{1}{4}X^3Y^3. \end{aligned} \tag{4.5}$$

By replacing (X, Y) with $(x-x^0, y-y^0)$ in Eq. (4.5), we return to the integral jet space coordinates. In particular, $Y_{\mathcal{SA}}^{(10)} = Y^{(10)} - \frac{1}{2}XY = \int_\gamma (x - x^0)\,dy - \frac{1}{2}(x - x^0)(y - y^0)$.

We introduce a simpler notation for the special affine invariants which will be subsequently used to solve the classification problem with respect to both the special and the full affine groups:

$$\begin{aligned} I_1 &= Y_{\mathcal{SA}}^{(10)} = Y^{(10)} - \frac{1}{2}XY, \\ I_2 &= Y_{\mathcal{SA}}^{(11)} = X\,Y^{(11)} + Y\,X^{(11)} - \frac{2}{3}\,Y^2X^2, \\ I_3 &= Y_{\mathcal{SA}}^{(12)} = X^2\,Y^{(12)} - XY\,Y^{(21)} - Y^2\,X^{(21)} + \frac{1}{4}X^3Y^3. \end{aligned} \tag{4.6}$$

Consider a planar curve $\gamma(t) = (1/2\,\sin t - \cos t + 1, \sin^2 t + \cos t - 1)$, shown in Figure 6.1-a. A curve $\overline{\gamma}(t)$ (Figure 6.1-b) is obtained from $\gamma(t)$ by a special affine transformation $\begin{pmatrix} 2 & 1 \\ 2 & 1.5 \end{pmatrix}$.

The integral invariants I_1, I_2 and I_3 for both curves with same parametrization coincide and are shown in Figure 6.2-a, Figure 6.2-b, and Figure 6.2-c .

To obtain invariants with respect to the full affine group we need to consider the effect of reflections and arbitrary scaling on the above invariants. We note that the transformation $x \to \lambda x$ and $y \to -\lambda y$ induces the transformation $I_1 \to -\lambda^2 I_1$, $I_2 \to \lambda^4 I_2$ and $I_3 \to -\lambda^6 I_3$. one may hence easily deduce that the following rational

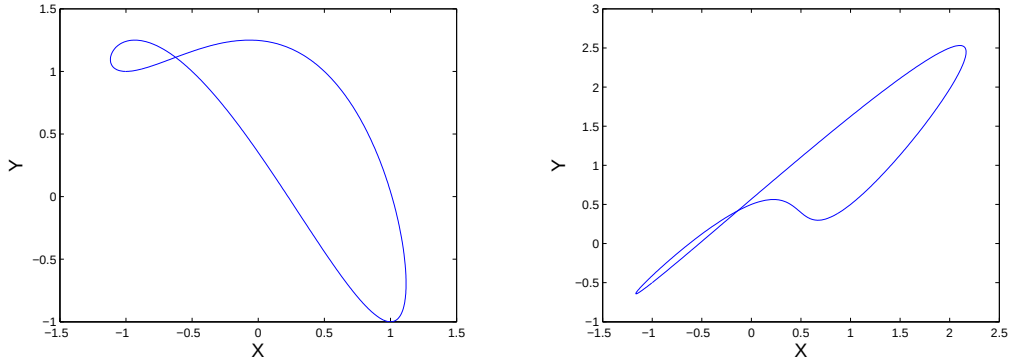

(a) (b)

Figure 4.1: (a) original curve $\gamma(t)$ (b) transformed curve $\overline{\gamma(t)}$

expressions are invariant with respect to the full affine group:

$$\begin{aligned} I_2^{\mathcal{A}} &= \frac{I_2}{I_1^2} = \frac{X\,Y^{(11)} + Y\,X^{(11)} - \frac{2}{3}\,Y^2X^2}{(Y^{(10)} - \frac{1}{2}XY)^2}, \\ I_3^{\mathcal{A}} &= \frac{I_3}{I_1^3} = \frac{X^2\,Y^{(12)} - XY\,Y^{(21)} - Y^2\,X^{(21)} + \frac{1}{4}X^3Y^3}{(Y^{(10)} - \frac{1}{2}XY)^3} \end{aligned} \tag{4.7}$$

The first of the above invariants is equivalent to the one obtained in [21].

4.2.2 Geometric interpretation of planar invariants

The first two integral invariants in Eq.(4.6) readily lend themselves to a geometric interpretation. Invariant I_1 is the area A_b between the curve segment and the secant (see Figure 4.3). Indeed the term Y_{10} in the invariant I_1 is the signed area between the curve $\gamma(t)$ (whose initial point is translated to the origin) and the secant, while $\frac{XY}{2}$ is the signed area of the triangle A_a. Their difference is the area A_b. Since the $\mathcal{S}A(2)$ action preserves areas, I_1 is clearly an invariant.

The interpretation of I_2 is slightly more subtle. By rearranging terms we have,

$$I_2 = -\frac{1}{3}((X^2Y^2 - 3X\,Y_{11}) + (X^2Y^2 - 3Y\,X_{11})), \text{ where } X = x - x^0, Y = y - y^0. \tag{4.8}$$

Further, the curve $\gamma(t)$ is lifted from 2D to 3D by defining $z(t) = x(t)y(t)$ (similar to

the kernel idea), and Eq. (4.8) is rewritten as

$$I_2 = -\frac{1}{3}((XYZ - 3X\int_a^t ZdY) + (XYZ - 3Y\int_a^t ZdX)), \tag{4.9}$$

where $Z = XY = (x - x^0)(y - y^0)$. The geometric meaning of $(XYZ - 3X\int_a^t ZdY)$ is illustrated in Figure 4.4. The term $\int_a^t ZdY$ is the signed area "under" the plane curve $(Y(t), Z(t))$ (this is the area A_a plus A_b in Figure 4.3 with X replaced by Z). Thus $X\int_a^t ZdY$ is the signed volume V_c under the surface F in Figure 4.4. Since XYZ is the signed volume of a rectangular prism ($V_c + V_d$ in Figure 4.4), then $XYZ - 3X\int_a^t ZdY$ is the signed volume of the rectangular prism $(V_c + V_d)$ minus three times the volume V_c "under" the surface $(Y(t), Z(t)) \times [0, X(t)]$. Interchanging X and Y we obtain a similar interpretation for $XYZ - 3Y\int_a^t ZdX$.

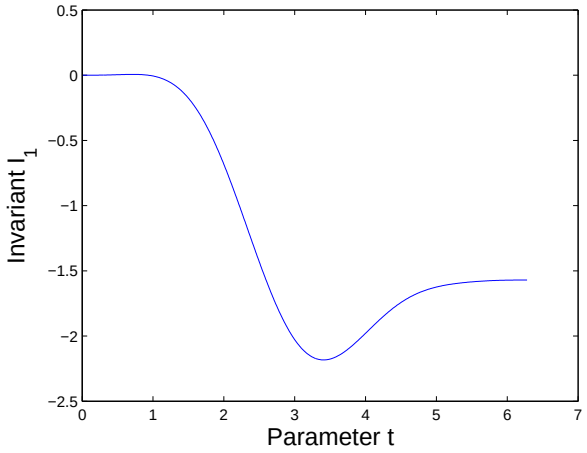

(a) Invariant I_1 for $\gamma(t)$ and $\overline{\gamma(t)}$

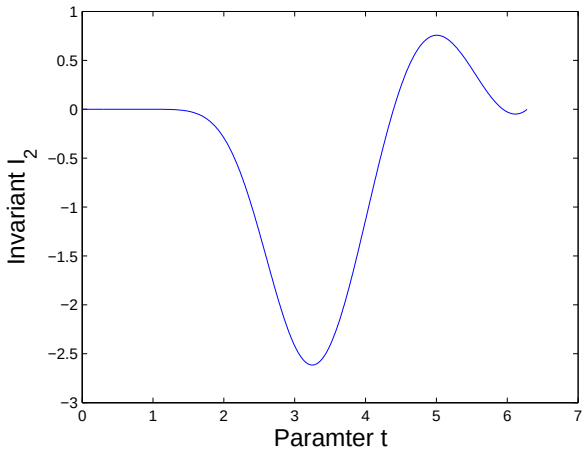

(b) Invariant I_2 for $\gamma(t)$ and $\overline{\gamma(t)}$

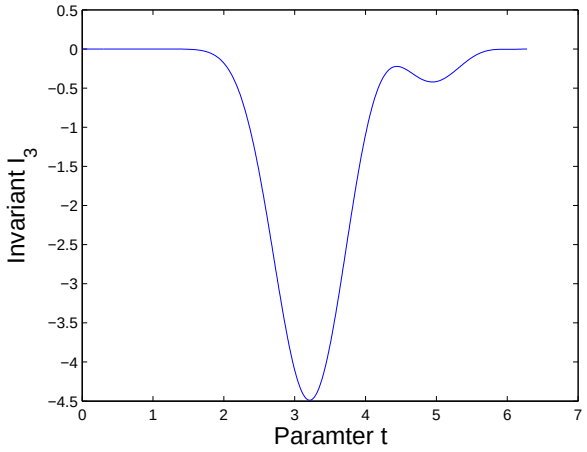

(c) Invariant I_3 for $\gamma(t)$ and $\overline{\gamma(t)}$

Figure 4.2: Integral invariants for 2D curves

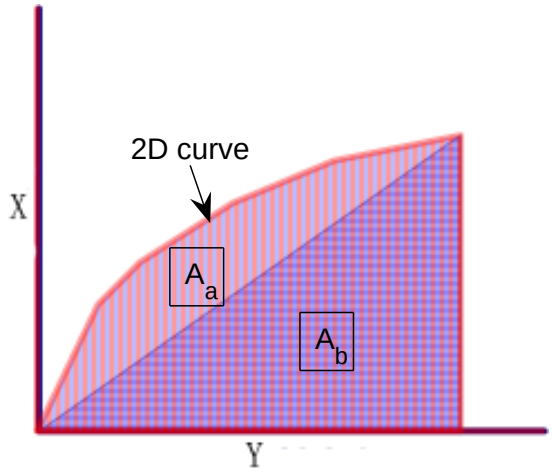

Figure 4.3: Geometric interpretation of invariant I_1

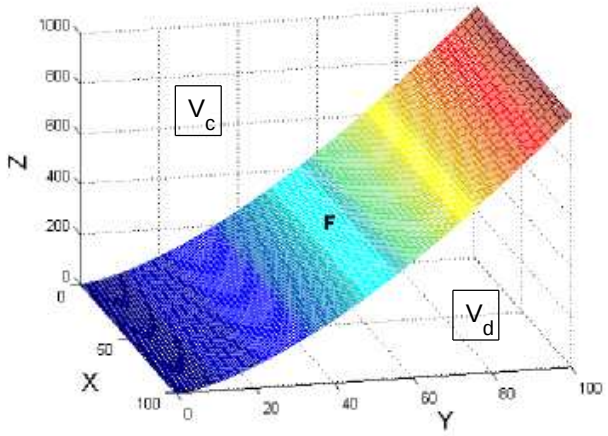

Figure 4.4: Geometric interpretation of invariant I_2

Chapter 5

Extending integral invariant from 2D to 3D

In Chapter 4, the 2D integral invariants development is simplified by way of the inductive method. To address the earlier failed attempt to obtain fully integral invariants in Chapter 3, we call upon the inductive decomposition approach of transformations to simplify the analytical tractability of our development of 3D affine integral invariants.

Following the 2D inductive case, we start from a special affine transformation, and decompose it into a product of the special orthogonal transformation matrix and an upper triangular transformation matrix with determinant 1. Invariants for $SO(3)$ are first developed. These in turn serve as basis to inductively develop the special affine invariants. The full affine invariants are based on the ratio of the special affine invariants.

5.1 Transformation decomposition

The standard affine group action on $\mathbb{R}^3$ is written as,

$$\begin{pmatrix} \overline{x} \\ \overline{y} \\ \overline{z} \end{pmatrix} = \begin{pmatrix} a_{11} & a_{12} & a_{13} \\ a_{21} & a_{22} & a_{23} \\ a_{31} & a_{32} & a_{33} \end{pmatrix} \begin{pmatrix} x \\ y \\ z \end{pmatrix} + \begin{pmatrix} v_1 \\ v_2 \\ v_3 \end{pmatrix}, \quad \det \begin{pmatrix} a_{11} & a_{12} & a_{13} \\ a_{21} & a_{22} & a_{23} \\ a_{31} & a_{32} & a_{33} \end{pmatrix} \neq 0.$$

We start by considering the action of $SL(3)$ defined by Eq.(3.2) on the integral variables up to order 2. Taking into account the relations that arise from an integration by parts, it is sufficient to consider the following 11 integral variables: Z_{100}, Z_{010}, Y_{100}, Z_{011}, Z_{020}, Z_{101}, Z_{110}, $Y_{101}\,X_{110}$, $X_{101}\,X_{020}$. We therefore obtain an action of $SL(3)$ on $\mathbb{R}^{14}$. The integral jet space is constructed as,

$$(X, Y, Z, Z_{100}, Z_{010}, Y_{100}, Z_{011}, Z_{020}, Z_{101}, Z_{110}, Y_{101}\,X_{110}, X_{101}\,X_{020})$$

A direct implementation of the moving frame in $\mathbb{R}^{14}$ doesn't work. Thus we have a product decomposition $SL(3) = B \cdot A$, where $B = \left\{ \begin{pmatrix} b_{11} & b_{12} & b_{13} \\ 0 & b_{22} & b_{23} \\ 0 & 0 & \frac{1}{b_{11}b_{22}} \end{pmatrix} | b_{11} > 0 \right\}$ and $A = SO(3)$ is a group of rotations. The intersection $B \cap A = \phi$ is trivial.

5.2 Special Euclidean invariant

We first restrict the action Eq.(3.2) to A whose elements can be represented as the product of three rotations:

$$\mathbf{A} = \begin{pmatrix} 1 & 0 & 0 \\ 0 & cos(\psi) & -sin\psi \\ 0 & sin\psi & cos\psi \end{pmatrix} \begin{pmatrix} cos\phi & 0 & sin\phi \\ 0 & 1 & 0 \\ -sin\phi & 0 & cos\phi \end{pmatrix} \begin{pmatrix} cos\theta & -sin\theta & 0 \\ sin\theta & cos\theta & 0 \\ 0 & 0 & 1 \end{pmatrix}$$

$$= \begin{pmatrix} \cos(\phi)\cos(\theta) & \cos(\phi)\sin(\theta) & -\sin(\phi) \\ \sin(\psi)\sin(\phi)\cos(\theta) - \cos(\psi)\sin(\theta) & \sin(\psi)\sin(\phi)\sin(\theta) + \cos(\psi)\cos(\theta) & \sin(\psi)\cos(\phi) \\ \cos(\psi)\sin(\phi)\cos(\theta) + \sin(\psi)\sin(\theta) & \cos(\psi)\sin(\phi)\sin(\theta) - \sin(\psi)\cos(\theta) & \cos(\psi)\cos(\phi) \end{pmatrix}.$$

We may prolong this group action on the integral jet space by replacing

$$\begin{aligned} a_{11} &= \cos(\phi)\cos(\theta), \\ a_{12} &= \cos(\phi)\sin(\theta), \\ a_{13} &= -\sin(\phi), \\ a_{21} &= \sin(\psi)\sin(\phi)\cos(\theta) - \cos(\psi)\sin(\theta), \\ a_{22} &= \sin(\psi)\sin(\phi)\sin(\theta) + \cos(\psi)\cos(\theta), \\ a_{23} &= \sin(\psi)\cos(\phi), \\ a_{31} &= \cos(\psi)\sin(\phi)\cos(\theta) + \sin(\psi)\sin(\theta), \\ a_{32} &= \cos(\psi)\sin(\phi)\sin(\theta) - \sin(\psi)\cos(\theta), \\ a_{33} &= \cos(\psi)\cos(\phi). \end{aligned}$$

in Eq.(3.2). The three angles(or the "sin" and "cos" of these three angles) may be solved by setting $Y = 0$, $Z = 0$, $Z_{011} = 0$ as a cross-section. This still remaining complex, we can adopt the inductive method for deriving a Euclidean Invariant. A may be further decomposed into a product of $A_1 A_2$, where

$$A_1 = \begin{pmatrix} 1 & 0 & 0 \\ 0 & cos(\psi) & -sin\psi \\ 0 & sin\psi & cos\psi \end{pmatrix},$$

$$A_2 = \begin{pmatrix} cos\phi & 0 & sin\phi \\ 0 & 1 & 0 \\ -sin\phi & 0 & cos\phi \end{pmatrix} \begin{pmatrix} cos\theta & -sin\theta & 0 \\ sin\theta & cos\theta & 0 \\ 0 & 0 & 1 \end{pmatrix}$$

$$= \begin{pmatrix} \cos^2\phi\,\theta & \cos\,\phi\,\sin\,\theta & -\sin\,\phi \\ -\sin\,\theta & \cos\,\theta & 0 \\ \cos\,\phi\,\sin\,\theta & \sin^2\phi\,\theta & \cos\,\phi \end{pmatrix}.$$

We may prolong the group action A_2 in the integral jet space by replacing

$$\begin{aligned} a_{11} &= \cos^2\phi\,\theta, a_{12} = \cos\,\phi\,\sin\,\theta, a_{13} = -\sin\,\phi, \\ a_{21} &= -\sin\,\theta, a_{22} = \cos\,\theta, a_{23} = 0, \\ a_{31} &= \cos\,\phi\,\sin\,\theta, a_{32} = \sin^2\phi\,\theta, a_{33} = \cos\,\phi. \end{aligned} \tag{5.1}$$

in Eq.(3.2) and the the "sin" and "cos" of these two angles (ϕ and θ) may be solved by setting $Y = 0,\ Z = 0, X > 0$ serves as a cross-section, which is

$$\begin{aligned} \overline{Y} &= -\sin\,\theta\,X + \cos\,\theta\,Y = 0, \\ \overline{Z} &= \cos\,\phi\,\sin\,\theta\,X + \sin\phi\,\sin\theta\,Y + \cos\,\phi\,Z = 0, \\ \overline{X} &= \cos\phi\,\cos\theta\,X + \cos\,\phi\,\sin\,\theta\,Y - \sin\,\phi\,Z > 0. \end{aligned} \tag{5.2}$$

The solution is:

$$\begin{aligned} \cos\theta &= \frac{X}{\sqrt{X^2+Y^2}}, \sin\theta = -\frac{Y}{\sqrt{X^2+Y^2}}, \\ \cos\phi &= \frac{\sqrt{X^2+Y^2}}{\sqrt{X^2+Y^2+Z^2}}, \cos\phi = \frac{Z}{\sqrt{X^2+Y^2+Z^2}}. \end{aligned} \tag{5.3}$$

The invariants for A_2 is achieved by replacing Eq.(5.3) into the prolonged integral variables:

$$
\begin{aligned}
X_R &= \sqrt{X^2+Y^2+Z^2}, \\
Z_R^{(010)} &= -\frac{1}{2}\frac{XYZ - 2\,XZ^{(010)} + 2\,YZ^{(100)} - 2\,ZY^{(100)}}{\sqrt{X^2+Y^2+Z^2}}, \\
Z_R^{(100)} &= -\frac{1}{2}\frac{X^2Z - 2\,XZ^{(100)} + Y^2Z - 2\,YZ^{(010)}}{\sqrt{X^2+Y^2}}, \\
Y_R^{(100)} &= -\frac{1}{2}\frac{YX^3 + XY^3 - 2\,Y^2Y^{(100)} - 2\,ZYZ^{(100)} - 2\,X^2Y^{(100)} + 2\,ZXZ^{(010)}}{\sqrt{X^2+Y^2}\sqrt{X^2+Y^2+Z^2}},
\end{aligned}
$$

$$
\begin{aligned}
Z_R^{(011)} &= \frac{2\,YX^3Z^2 - 6\,X^3Z^{(011)} + 6\,X^2YZ^{(101)} - 6\,X^2ZY^{(101)} - 6\,XZ^{(011)}Y^2}{-6(\sqrt{X^2+Y^2}\,(X^2+Y^2+Z^2))} \\
&\quad + \frac{6\,XYZX^{(101)} - 6\,XZ^2X^{(110)} - 6\,Y^2ZZ^{(110)} - 6\,Y^2ZY^{(101)}}{-6(\sqrt{X^2+Y^2}\,(X^2+Y^2+Z^2))} \\
&\quad + \frac{4\,Z^2Y^3X + 3\,XYZZ^{(020)} + 6\,Y^3Z^{(101)} - 3\,Z^2YX^{(020)}}{-6(\sqrt{X^2+Y^2}\,(X^2+Y^2+Z^2))}, \\
Z_R^{(020)} &= -\frac{1}{3}\frac{-3\,X^2Z^{(020)} - 2\,Y^2X^2Z + 6\,XYZ^{(110)} + 3\,XZX^{(020)} + 6\,Y^2X^{(101)}}{\sqrt{X^2+Y^2}\sqrt{X^2+Y^2+Z^2}} \\
&\quad - \frac{1}{3}\frac{-6\,ZYX^{(110)}}{\sqrt{X^2+Y^2}\sqrt{X^2+Y^2+Z^2}}, \\
Z_R^{(101)} &= \frac{-4\,Z^2X^4 + 6\,Z^{(101)}X^3 + 6\,X^2YZ^{(011)} - 2\,X^2Z^2Y^2 + 6\,ZX^2X^{(101)}}{(6\,X^2+6\,Y^2)\sqrt{X^2+Y^2+Z^2}} \\
&\quad + \frac{6\,XZ^{(101)}Y^2 - 3\,Y^2ZZ^{(020)} + 6\,Y^3Z^{(011)} - Z^2Y^4 - 6\,XYZZ^{(110)}}{(6\,X^2+6\,Y^2)\sqrt{X^2+Y^2+Z^2}},
\end{aligned}
$$

$$
\begin{aligned}
Z_R^{(110)} \;=\; & \frac{6\,Z^2XY\,X^{(101)} - 6\,ZXY^2X^{(110)} - 3\,ZX^2Y\,X^{(020)} + 6\,Z^2Y^2\,Y^{(101)}}{(6\,X^2+6\,Y^2+6\,Z^2)\,(X^2+Y^2)} \\
& + \frac{6\,X^4Z^{(110)} - 6\,Y^4Z^{(110)} - 6\,ZY\,Z^{(101)}\,X^2 + 6\,ZX\,Z^{(011)}\,Y^2}{(6\,X^2+6\,Y^2+6\,Z^2)\,(X^2+Y^2)} \\
& + \frac{-6\,ZX^3X^{(110)} - 3\,X^3Y^3Z + 12\,X^3Y\,X^{(101)} + 12\,XY^3X^{(101)}}{(6\,X^2+6\,Y^2+6\,Z^2)\,(X^2+Y^2)} \\
& + \frac{6\,X^3Y\,Z^{(020)} + 6\,XY^3Z^{(020)} + 6\,ZX^3Z^{(011)} - 6\,X^3Z^3Y + 6\,X^2Z^2Z^{(110)}}{(6\,X^2+6\,Y^2+6\,Z^2)\,(X^2+Y^2)} \\
& + \frac{6\,X^2Z^2\,Y^{(101)} - 3\,ZY^3X^{(020)} - 3\,Z^3Y^3X}{(6\,X^2+6\,Y^2+6\,Z^2)\,(X^2+Y^2)} \\
& + \frac{3\,Z^2XY\,Z^{(020)} - 4\,ZX^5Y + ZY^5X - 6\,ZY^3Z^{(101)}}{(6\,X^2+6\,Y^2+6\,Z^2)\,(X^2+Y^2)},
\end{aligned}
$$

$$
\begin{aligned}
Y_R^{(101)} \;=\; & \frac{-6\,X^4\,Y^{(101)} - 12\,ZXY^2X^{(110)} + 6\,Z^2Y^2\,Y^{(101)} - 6\,ZX^2Y\,X^{(020)}}{-6\,(X^2+Y^2+Z^2)\,(X^2+Y^2)} \\
& + \frac{-6\,Y^2Z^{(110)}\,X^2 - 12\,ZY\,Z^{(101)}\,X^2 + 6\,Y^2Z^2Z^{(110)} - 12\,Y^2X^2\,Y^{(101)}}{-6\,(X^2+Y^2+Z^2)\,(X^2+Y^2)} \\
& + \frac{-6\,ZY^3X^{(020)} - 12\,ZX^3X^{(110)} - 3\,Z^3Y^3X + 9\,X^3Y^3Z + 4\,ZX^5Y}{-6\,(X^2+Y^2+Z^2)\,(X^2+Y^2)} \\
& + \frac{12\,ZX^3Z^{(011)} + 3\,XY^3Z^{(020)} - 3\,Z^2XY\,Z^{(020)} + 12\,ZX\,Z^{(011)}\,Y^2}{-6\,(X^2+Y^2+Z^2)\,(X^2+Y^2)} \\
& + \frac{-6\,Z^2XY\,X^{(101)} + 6\,XY^3X^{(101)} + 6\,X^3Y\,X^{(101)} + 6\,X^2Z^2\,Y^{(101)}}{-6\,(X^2+Y^2+Z^2)\,(X^2+Y^2)} \\
& + \frac{3\,X^3Y\,Z^{(020)} + 5\,ZY^5X - 12\,ZY^3Z^{(101)} - 6\,Y^4\,Y^{(101)} - 6\,Y^4Z^{(110)}}{-6\,(X^2+Y^2+Z^2)\,(X^2+Y^2)},
\end{aligned}
$$

$$
\begin{aligned}
X_R^{(110)} &= \frac{-Y^5X + 3\,Z^2Y^3X - 6\,ZY^2\,Y^{(101)} - 6\,ZX^2\,Y^{(101)} - 6\,ZY^2Z^{(110)}}{(6\,X^2 + 6\,Y^2 + 6\,Z^2)\,\sqrt{X^2+Y^2}} \\
&+ \frac{6\,X^3X^{(110)} + 3\,XYZZ^{(020)} + 3\,X^2YX^{(020)} + 6\,XYZX^{(101)} - 2\,X^5Y}{(6\,X^2 + 6\,Y^2 + 6\,Z^2)\,\sqrt{X^2+Y^2}} \\
&+ \frac{3\,Y^3X^{(020)} - 3\,X^3Y^3 - 6\,Z^2YZ^{(101)} + 6\,Z^2XZ^{(011)} + 6\,XY^2X^{(110)}}{(6\,X^2 + 6\,Y^2 + 6\,Z^2)\,\sqrt{X^2+Y^2}},
\end{aligned}
$$

$$
\begin{aligned}
X_R^{(101)} &= \frac{-2\,ZX^4 + 6\,X^2X^{(101)} + 2\,Y^2X^2Z + 2\,X^2Z^3 - 6\,XYZ^{(110)}}{6\sqrt{X^2+Y^2}\sqrt{X^2+Y^2+Z^2}} \\
&+ \frac{-6\,ZXZ^{(101)} - 6\,ZYZ^{(011)} + 2\,Y^2Z^3 + Y^4Z - 3\,Z^{(020)}\,Y^2}{6\sqrt{X^2+Y^2}\sqrt{X^2+Y^2+Z^2}}, \\
X_R^{(020)} &= \frac{-X^4Y^2 - Y^4X^2 - 3\,XY^2X^{(020)} - 3\,X^2Z^2Y^2 + 6\,Y^2ZX^{(101)}}{-3\sqrt{X^2+Y^2+Z^2}\,(X^2+Y^2)} \\
&+ \frac{6\,XYZZ^{(110)} - 3\,ZX^2Z^{(020)} + 6\,X^2YX^{(110)} - 3\,X^3X^{(020)} + 6\,Y^3X^{(110)}}{-3\sqrt{X^2+Y^2+Z^2}\,(X^2+Y^2)}.
\end{aligned}
\tag{5.4}
$$

The next step is to extend group action of A_1 into the invariants of A_2 by replacing

$$a_{11} = 1, a_{12} = 0, a_{13} = 0, a_{21} = 0, a_{22} = cos\psi, a_{23} = -sin\psi, a_{31} = 0, a_{32} = sin\psi,$$

$a_{33} = cos\psi$ in Eq.(3.2). Since there is only one group parameter ψ, we may set up $Z_R^{(011)} = 0$, and the solution for $\sin\psi$ and $\cos\psi$ is:

$$\cos\psi = \frac{Z_R^{(020)}}{\sqrt{{Z_R^{(020)}}^2 + 4\,{Z_R^{(011)}}^2}}, \sin\psi = \frac{-2Z_R^{(011)}}{\sqrt{{Z_R^{(020)}}^2 + 4\,{Z_R^{(011)}}^2}}$$

Substituting the solution into the prolonged variable, we obtain the invariants for

A

$$
\begin{aligned}
X_{\mathcal{SE}} &= X_R, \\
Z_{\mathcal{SE}}^{(010)} &= Z_R^{(010)}, \\
Z_{\mathcal{SE}}^{(100)} &= -\frac{2\,Z_R^{(011)}\,Y_R^{(100)} - Z_R^{(020)}\,Z_R^{(100)}}{\sqrt{{Z_R^{(020)}}^2 + 4\,{Z_R^{(011)}}^2}}, \\
Y_{\mathcal{SE}}^{(100)} &= \frac{Z_R^{(020)}\,Y_R^{(100)} + 2\,Z_R^{(011)}\,Z_R^{(100)}}{\sqrt{{Z_R^{(020)}}^2 + 4\,{Z_R^{(011)}}^2}}, \\
Y_{\mathcal{SE}}^{(101)} &= -\frac{-2\,Z_R^{(020)}\,Z_R^{(011)}\,Z_R^{(101)} - Z_R^{(011)}\,Z_R^{(020)}\,X_R^{(020)} + 4\,{Z_R^{(011)}}^2 Z_R^{(110)}}{{Z_R^{(020)}}^2 + 4\,{Z_R^{(011)}}^2} \\
&\quad -\frac{{Z_R^{(020)}}^2\,Y_R^{(101)}}{{Z_R^{(020)}}^2 + 4\,{Z_R^{(011)}}^2}, \\
Z_{\mathcal{SE}}^{(020)} &= \sqrt{{Z_R^{(020)}}^2 + 4\,{Z_R^{(011)}}^2}, \\
Z_{\mathcal{SE}}^{(101)} &= -\frac{2\,Z_R^{(020)}\,Z_R^{(011)}\,Z_R^{(110)} - {Z_R^{(020)}}^2 Z_R^{(101)} + 2\,{Z_R^{(011)}}^2 X_R^{(020)}}{{Z_R^{(020)}}^2 + 4\,{Z_R^{(011)}}^2} \\
&\quad +\frac{2\,Z_R^{(011)}\,Z_R^{(020)}\,Y_R^{(101)}}{{Z_R^{(020)}}^2 + 4\,{Z_R^{(011)}}^2}, \\
Z_{\mathcal{SE}}^{(110)} &= \frac{2\,Z_R^{(020)}\,Z_R^{(011)}\,Z_R^{(101)} + Z_R^{(011)}\,Z_R^{(020)}\,X_R^{(020)} - 4\,{Z_R^{(011)}}^2 Y_R^{(101)}}{{Z_R^{(020)}}^2 + 4\,{Z_R^{(011)}}^2} \\
&\quad +\frac{{Z_R^{(020)}}^2 Z_R^{(110)}}{{Z_R^{(020)}}^2 + 4\,{Z_R^{(011)}}^2}.
\end{aligned}
\tag{5.5}
$$

5.3 Special and Full Affine Invariant

We now restrict the action of Eq.(3.2) to the action of a subgroup B based on the invariants we achieved in the section above. By substituting

$$a_{11} = b_{11}, a_{12} = b_{12}, a_{13} = b_{13}, a_{21} = 0, a_{22} = b_{22}, a_{23} = b_{23}, a_{31} = 0, a_{32} = 0, a_{33} = \frac{1}{a_{11}a_{22}},$$

the following transformations are obtained:

$$
\begin{aligned}
\overline{X_{SA}} &= b_{11}\, X_{SE}, \\
\overline{Z_{SA}^{(010)}} &= b_{22}\, b_{33}\, Z_{SE}^{(010)}, \\
\overline{Z_{SA}^{(100)}} &= b_{11}\, b_{33}\, Z_{SE}^{(100)} + b_{12}\, b_{33}\, Z_{SE}^{(010)}, \\
\overline{Y_{SA}^{(100)}} &= b_{11}\, b_{22}\, Y_{SE}^{(100)} - b_{13}\, b_{22}\, Z_{SE}^{(010)} + b_{11}\, b_{23}\, Z_{SE}^{(100)} + b_{12}\, b_{23}\, Z_{SE}^{(010)}, \\
\overline{Z_{SA}^{(020)}} &= {b_{22}}^2 b_{33}\, Z_{SE}^{(020)}, \\
\overline{Z_{SA}^{(101)}} &= b_{11}\, {b_{33}}^2 Z_{SE}^{(101)}, \\
\overline{Z_{SA}^{(110)}} &= b_{33}\, b_{11}\, b_{22}\, Z_{SE}^{(110)} + b_{33}\, b_{11}\, b_{23}\, Z_{SE}^{(101)} + b_{33}\, b_{12}\, b_{22}\, Z_{SE}^{(020)}, \\
\overline{Y_{SA}^{(101)}} &= Y_{SE}^{(101)} + \frac{b_{23} Z_{SE}^{(101)}}{b_{22}} - \frac{b_{12} Z_{SE}^{(020)}}{2 b_{11}}.
\end{aligned} \tag{5.6}
$$

We choose a cross-section defined by the equations

$$
\overline{Z_{SA}^{(010)}} = 1, \overline{Z_{SA}^{(100)}} = 1, \overline{Y_{SA}^{(100)}} = 1, \overline{Z_{SA}^{(020)}} = 1, \overline{Z_{SA}^{(110)}} = 1,
$$

to yield the following group parameters,

$$
\begin{aligned}
b_{11} &= Z_{SE}^{010}, \\
b_{12} &= -\frac{Z_{SE}^{(020)} Z_{SE}^{(100)} - Z_{SE}^{(010)}}{Z_{SE}^{(020)}}, \\
b_{13} &= -\frac{-{Z_{SE}^{(010)}}^2 Z_{SE}^{(020)} Z_{SE}^{(100)} + {Z_{SE}^{(010)}}^3 Z_{SE}^{(110)} - Z_{SE}^{(020)} Z_{SE}^{(101)} {Z_{SE}^{(010)}}^2 Y_{SE}^{(100)}}{Z_{SE}^{(020)} Z_{SE}^{(101)} {Z_{SE}^{(010)}}^2} \\
&\quad + \frac{Z_{SE}^{(101)} {Z_{SE}^{(020)}}^2}{Z_{SE}^{(020)} Z_{SE}^{(101)} {Z_{SE}^{(010)}}^2}, \\
b_{22} &= \frac{Z_{SE}^{(010)}}{Z_{SE}^{(020)}}, \\
b_{23} &= \frac{-Z_{SE}^{(010)} Z_{SE}^{(110)} + Z_{SE}^{(020)} Z_{SE}^{(100)}}{Z_{SE}^{(020)} Z_{SE}^{(101)}}.
\end{aligned} \tag{5.7}
$$

We use them to construct the invariants with respect to the $SA(3)$ actions,

$$\begin{aligned} X_{\mathcal{SA}} &= Z_{\mathcal{SE}}^{(010)} X_{\mathcal{SE}}, \\ Y_{\mathcal{SA}}^{(101)} &= \frac{2Y_{\mathcal{SE}}^{(101)} Z_{\mathcal{SE}}^{(010)} - 2Z_{\mathcal{SE}}^{(010)} Z_{\mathcal{SE}}^{(110)} + 3Z_{\mathcal{SE}}^{(020)} Z_{\mathcal{SE}}^{(100)}}{2Z_{\mathcal{SE}}^{(010)}} - \frac{1}{2}, \\ Z_{\mathcal{SA}}^{(101)} &= \frac{Z_{\mathcal{SE}}^{(101)} {Z_{\mathcal{SE}}^{(020)}}^2}{{Z_{\mathcal{SE}}^{(010)}}^3}. \end{aligned} \tag{5.8}$$

For clarity sake, we introduce a simpler notation for the special affine invariants which will be subsequently used in a classification problem with respect to both special and full affine groups in terms of the original integral variables:

$$\begin{aligned} J_1 &= X_{\mathcal{SA}} = n_1 X + n_2 Z - n_3 Y \\ J_2 &= -4\left(Y_{\mathcal{SA}}^{(101)} + \frac{1}{2}\right) X_{\mathcal{SA}} = 2\,n_2(XYZ^2 - 3\,Z^{(011)}X + 3\,YZ^{(101)} - ZZ^{(110} - 2\,ZY^{(101)}) \\ &+ n_3(2\,XY^2Z + 3\,XZ^{(020)} - 3\,ZX^{(020)} - 4\,YZ^{(110)} - 2\,YY^{(101)}) \\ &- 2\,n_1(3\,YX^{(101)} - 3\,ZX^{(110} + XZ^{(110)} - XY^{(101)}) \\ J_3 &= \frac{27}{8} Z_{\mathcal{SA}}^{(101)} X_{SA}^3. \end{aligned} \tag{5.9}$$

where $X = x - x^0, Y = y - y^0, Z = z - z^0$ and $n_1 = \frac{YZ}{2} - Z_{010}, n_2 = \frac{XY}{2} - Y_{100}, n_3 = \frac{XZ}{2} - Z_{100}$.

For example, a space curve $\beta(t) = (\sin t - 1/5\,\cos^2 t + 1/5,\, 1/2\,\sin t - \cos t + 1\,\sin^2 t + \cos t - 1)$, is shown in Figure 6.6-a. A curve $\overline{\beta(t)}$ is obtained from β by a special affine transformation $\begin{pmatrix} 0.3816 & 0.7631 & 1.1447 \\ 1.9079 & 1.5263 & 2.2894 \\ 2.6710 & 3.0526 & 3.4341 \end{pmatrix}$.

The integral invariants I_1, I_2 and I_3 for both curves with the matching parametrization coincide and are shown in Figure 5.2-a, Figure 5.2-b, and Figure 5.2-c .

To obtain the invariants with respect to the full affine group we have to consider the effect of reflection and scaling on these invariants. For $\lambda \in \mathbb{R}$ scaling $(x, y, z) \to (\lambda x, \lambda y, -\lambda z)$ induces scaling $J_1 \to -\lambda^3 J_1$, $J_2 \to \lambda^6 J_2$ and $J_3 \to -\lambda^6 J_3$. Therefore

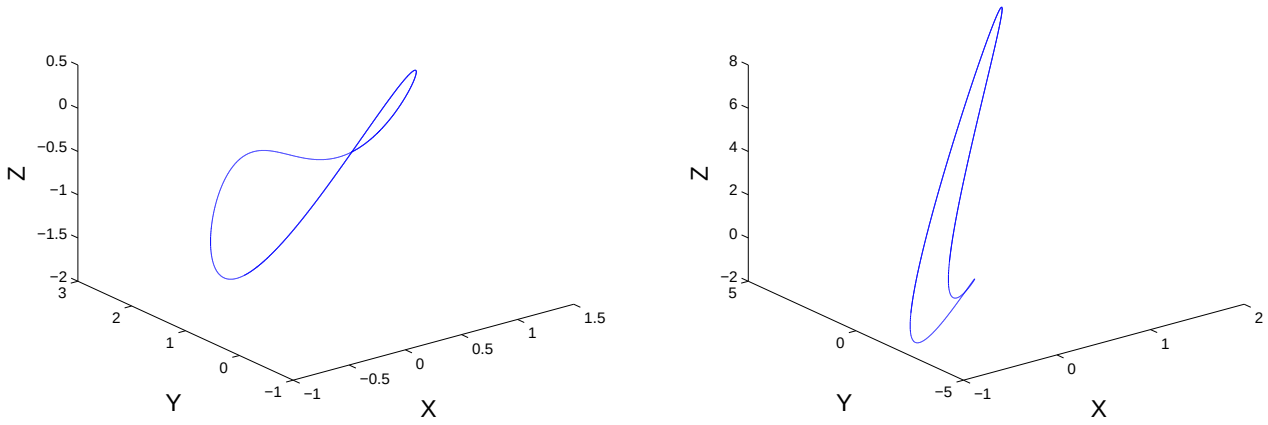

(a) (b)

Figure 5.1: (a) original curve $\beta(t)$ (b) special affine transformed curved $\overline{\beta(t)}$

we obtain invariants with respect to the full affine group of transformations:

$$J_2^{\mathcal{A}} = \frac{J_2}{J_1^2} \tag{5.10}$$
$$J_3^{\mathcal{A}} = \frac{J_3}{J_1^2}$$

5.4 Geometric interpretation

The first invariant J_1 may be viewed as 3D extension of the 2D invariant I_1. In detail, n_1, n_2, and n_3 represent exactly the same area as the 2D invariant I_1(in Figure4.3) in three coordinate planes. They are extended from 2D area to 3D volume by multiplying by X, Z, and Y respectively. For example, n_1X is the volume C under surface F in Figure 4.4, and n_2Z and n_3Y are similar volumes obtained by relabelling X, Y, Z axis. Therefore, the invariant J_1 is the summation of two volumes n_1X and n_2Z minus the volume n_3Y. The geometric interpretation of the second and third invariants J_2 and J_3, however, remains at the present time unclear to us.

Table 5.1: Classification error rate with same parametrization, same initial points

Noise variance	I_1	I_2
$\sigma = 0.5$	**0.0022**	0.0472
$\sigma = 1$	**0.04**	0.12
$\sigma = 2$	**0.0789**	0.2233

5.5 Robustness analysis

5.5.1 Design of experiment

We follow the same procedure in Section 3.3 to carry out a robust analysis for integral invariants. We extract a total of 100 characteristic curves, and each of them are re-sampled to 5000 points with the same arch-length. We applied to each curve 9 randomly generated 3D special affine transformations. To make this problem even more challenging and to illustrate the noise sensitivity of the proposed approach, gaussian noise with distribution $N(0, \sigma^2)$ is added to each of the variations. We therefore obtain a classification set of 900 curves that has to be separated into 100 equivalent classes under affine transformations. The training set consists of 100 original curves without any noise and transformation. The discrimination power and sensitivity to noise are analyzed using the error rate of classification. We implemented a Nearest Neighbor (NN) Classifier in a Euclidean Space using Euclidean distance.

5.5.2 Experimental results

The experiment is carried out with different noise variance, namely $\sigma = 2$(Fig. 5.5.2), $\sigma = 1$, and $\sigma = 0.5$. The error rates of the three sigma settings with same parametrization are shown in Table 5.1.

In Table 5.1, both integral invariants perform well as indicated by the error rates. For comparison, the classical differential invariants have a classification error rate of more than 80%, which makes the differential invariants practically useless. Since the order of integral variables involved in I_2 is higher than I_1, as well as the explicit form of I_2 is more complicated than that of I_1, the performance of I_2 is not as good as I_1. As for the mixed invariant that we proposed in Chapter 3, the error rate is 0.0971 at

$\sigma = 0.1$ and 0.1829 at $\sigma = 1$. Integral invariants (both I_1 and I_2) outperform their counterparts primarily due to the elimination of first order derivatives.

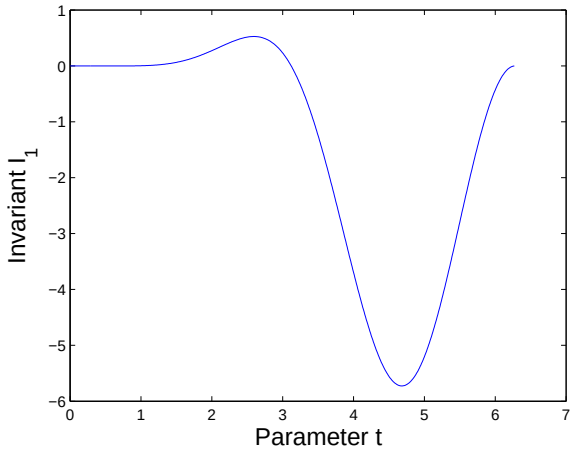

(a) Invariant I_1 for $\beta(t)$ and $\overline{\beta(t)}$

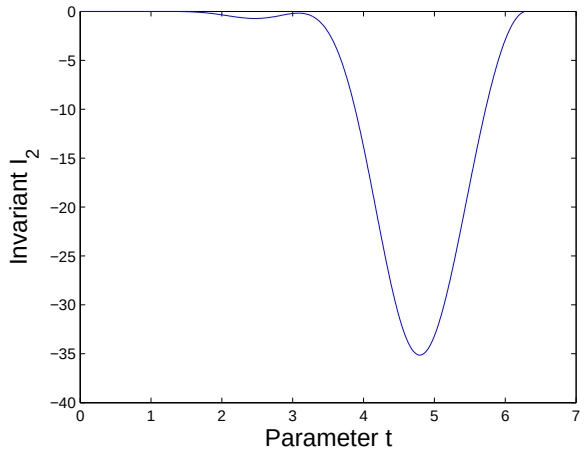

(b) Invariant I_2 for $\beta(t)$ and $\overline{\beta(t)}$

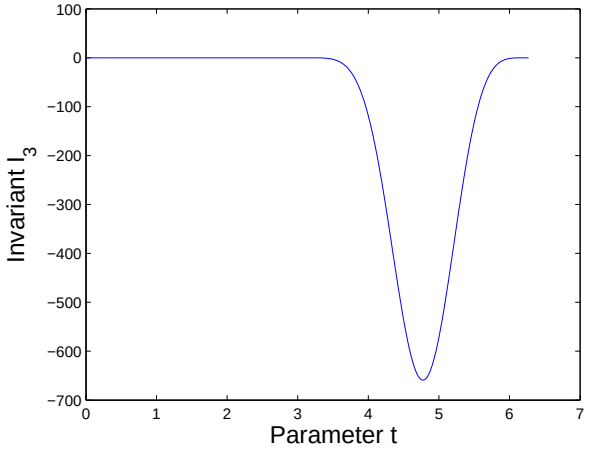

(c) Invariant I_3 for $\beta(t)$ and $\overline{\beta(t)}$

Figure 5.2: Integral invariants for curves in 3D

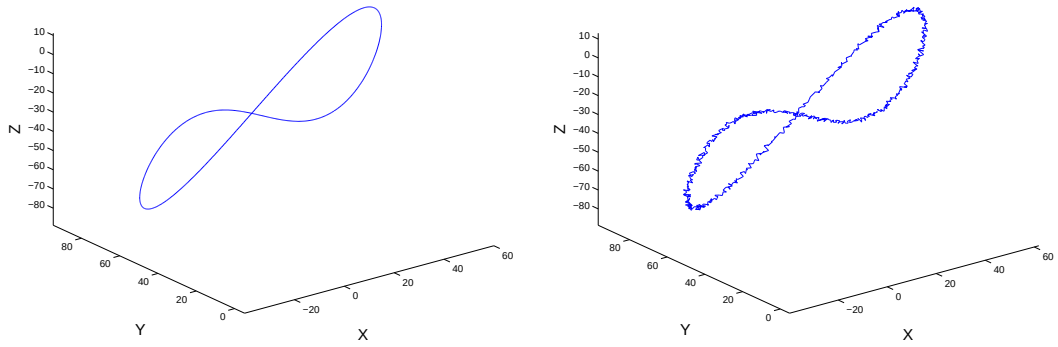

(a) (b)

Figure 5.3: (a) A spatial curve without noise (b)with Gaussian Noise $N(0, 4)$,

Chapter 6

Integral Invariant Signature

In Chapters 4 and 5, we developed three special affine integral invariants and two full affine invariants in 2D and 3D. They may be used to classify curves subjected to special affine or full affine transformations. There exists however a critical restriction for these invariants, depending on parameterization and initial point selection. In this chapter, we first address this problem in detail, and the notion of invariant signature is proposed as a solution. Parameterization independent invariants, 2D and 3D global integral invariant signatures, are developed, and the initialization problem is solved by 2D and 3D local integral invariant signatures.

6.1 Invariant Signature

Curves, with similar parameterization/similar sampling for a discrete case, under special affine and full affine transformations will have similar integral invariant (as shown in Fig. 5.2). These in turn may be efficiently used to classify curves under transformation. These invariants, however, depend on the choice of the initial point and the parameterization of the curve. For instance, consider a planar curve $\gamma(t) = (1/2\ \sin t - \cos t + 1, \sin^2 t + \cos t - 1)$, shown in Figure 6.1-a. A curve $\overline{\gamma}(t)$ (Figure 6.1-b) is obtained from $\gamma(t)$ by a special affine transformation $\begin{pmatrix} 2 & 1 \\ 2 & 1.5 \end{pmatrix}$. The integral invariants I_1 and I_2 for both these curves with the same parametrization are

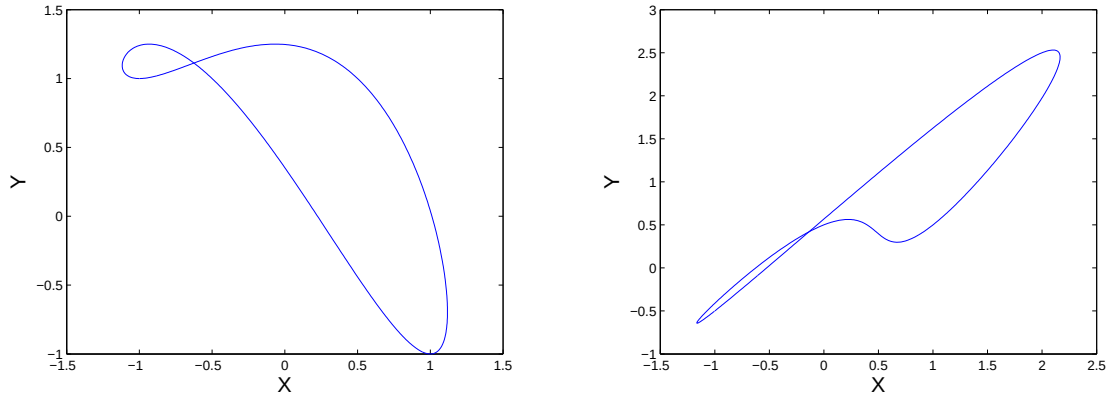

(a) (b)

Figure 6.1: (a) original curve $\gamma(t)$ (b) transformed curve $\overline{\gamma(t)}$

shown to coincide in Fig. 6.2-a and Fig. 6.2-b. As illustrated in Fig. 6.2-c and Fig. 6.2-d these invariants change under reparametrization $\tau = \sqrt{t+1}$. Therefore invariants with arbitrary parameterization may not be used for curves classification. In theory one can achieve a uniform affine invariant curve parameterization by using an affine analog of the Euclidean arc-length parameter $d\alpha = \kappa^{1/3} ds$, where κ is Euclidean curvature and ds is Euclidean arc-length. We would, however, like to keep our approach derivative free. Even when uniform parameterization is achieved, the dependence of the invariants on the choice of the initial point presents another comparison challenge for matching closed curves, or for matching parts of the contours.

The construction of a signature, proposed in this chapter, leads to classification methods which are independent of parameterization and initial point. Inspired by signatures based on differential invariants [7], we use integral invariants to construct two types of signatures that classify curves under affine transformation: the global signature and the local signature. Global integral signature is independent of parametrization, but is dependent on the choice of the initial point and can not be used to compare parts of the contours. Local integral signature is independent of both the initial point of a curve and its parametrization. They can be used to compare parts of the curves and can therefore be used on images with occlusions. As our experiments illustrate, they are slightly more sensitive to noise than global signatures, but still

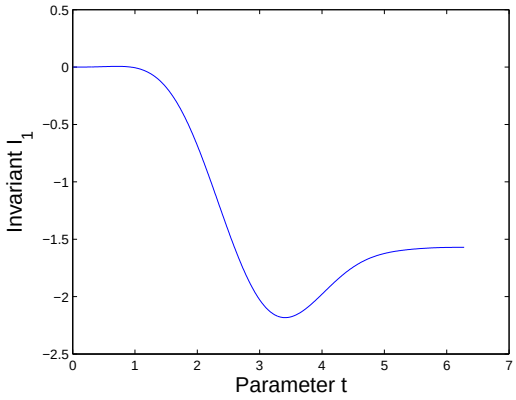

(a) Invariant I_1 for $\gamma(t)$ and $\overline{\gamma(t)}$

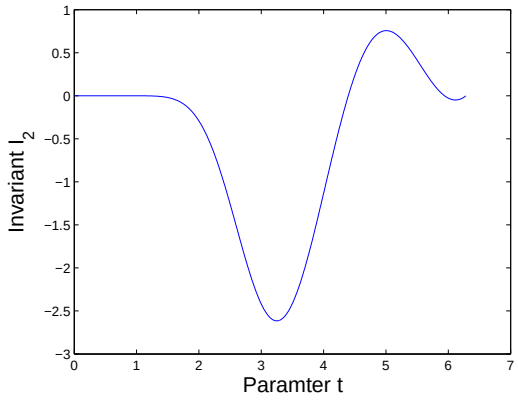

(b) Invariant I_2 for $\gamma(t)$ and $\overline{\gamma(t)}$

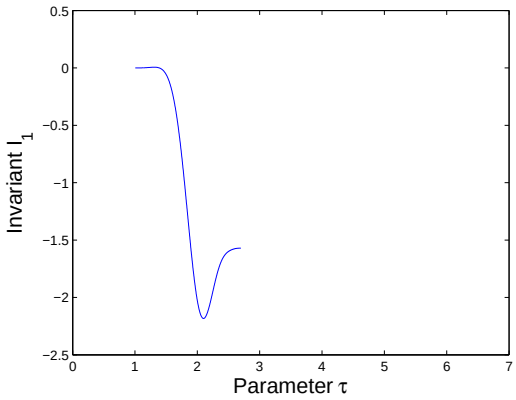

(c) Invariant I_1 for $\gamma(\tau)$ and $\overline{\gamma(\tau)}$

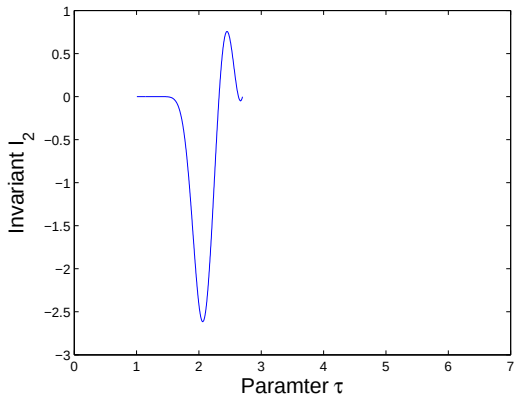

(d) Invariant I_2 for $\gamma(\tau)$ and $\overline{\gamma(\tau)}$

Figure 6.2: Dependence of invariants on re-prametrization: $\tau = \sqrt{t+1}$

provide robust classification results.

6.2 Global Integral Affine Signature

A global integral signature of a curve is achieved by evaluating one independent integral invariant against the other on the curve. If a curve is mapped to another curve by a group transformation, their signatures will coincide independently of the selected parametrization. The global signature does, however, depend on the choice of an initial point.

6.2.1 Global affine signature for curves in 2D

The special affine signature of a plane curve $\gamma(t)$ is constructed by, first, evaluating invariants I_1 and I_2 (4.5) on this curve, and then plotting the parameterized curve $(I_1(t), I_2(t))$ in $\mathbb{R}^2$. For instance, the signature of the planar curve $\gamma(t)$ shown in Figure 6.1-a is a plane curve shown in Figure 6.3. Moreover the signature of the curve $\overline{\gamma(t)}$ related to $\gamma(t)$ by an affine transformation (Figure 6.1-b), as well as their reparameterization $\gamma(\tau)$ and $\overline{\gamma(\tau)}$ coincide with the signature of $\gamma(t)$.

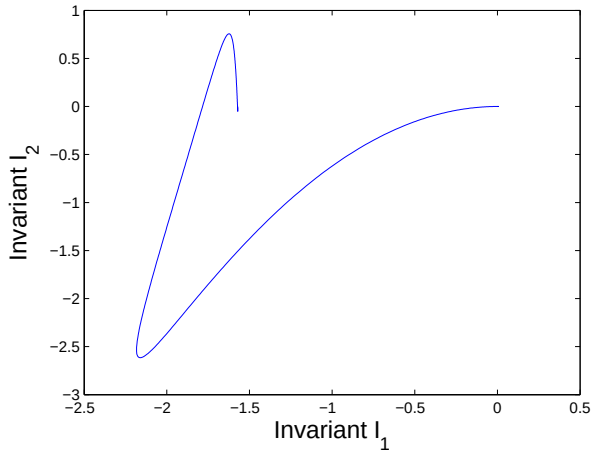

Figure 6.3: Signature for $\gamma(t)$, $\overline{\gamma(t)}$,$\gamma(\tau)$, and $\overline{\gamma(\tau)}$

Similarly a full affine signature can be defined as a parameterized plane curve $\left(I_2^{\mathcal{A}}, I_3^{\mathcal{A}}\right)$ defined by invariants (4.7). Alternatively we normalize the two special affine invariants to cancel the affects of reflection and arbitrary scaling:

$$\tilde{I}_1(t) = \frac{|I_1(t)|}{\max_t |I_1|}, \quad \tilde{I}_2(t) = \frac{|I_2|}{\max_t (I_1^2)}. \tag{6.1}$$

Both invariants are normalized relative to the range of $|I_1|$ due to the simplicity of I_1. It is not difficult to show that $\max_t |I_1| = 0$ on γ if and only if γ is a straight line. In this case the affine signature does not exits, but the straight line regions can easily be detected by other means. The range of $\tilde{I}_1$ is from 0 to 1. The full affine signature of a spatial curve $\gamma(t)$ is obtained by, first, evaluating $\tilde{I}_1$ and $\tilde{I}_2$ on this curve and then

by plotting the parameterized curve $\left(\tilde{I}_1(t), \tilde{I}_2(t)\right)$ in $\mathbb{R}^2$. As an example, curves in Fig. 6.4-a and Fig. 6.4-b are related by a full affine transformation $\begin{pmatrix} 2 & 2 \\ 4 & 3 \end{pmatrix}$. Their special affine signatures are shown difference in Fig. 6.5-a(better to view in color), while the full affine signatures are coincident in Fig. 6.5-b.

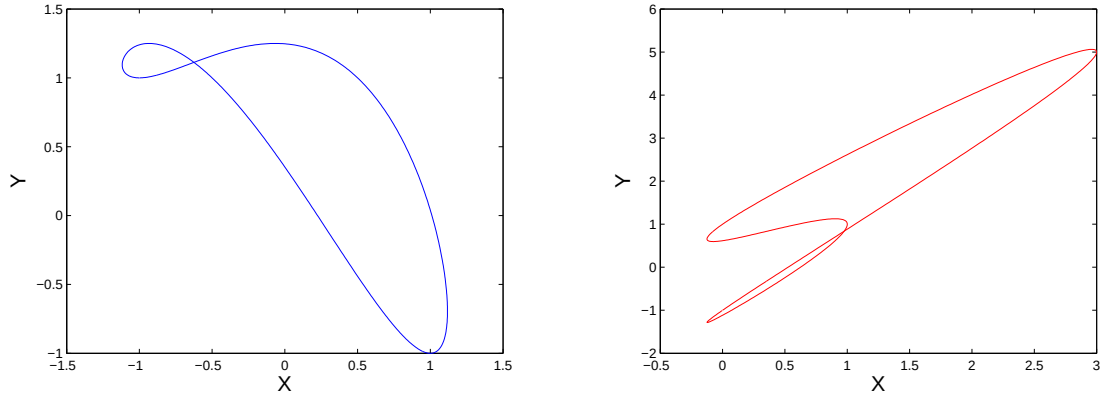

(a) (b)

Figure 6.4: (a) original curve $\gamma(t)$ (b) full affine transformed curve $\widehat{\gamma'(t)}$

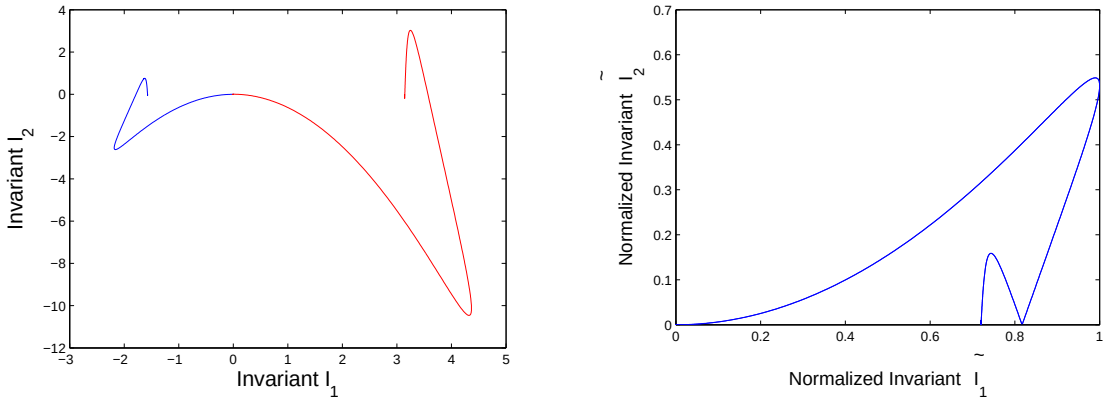

(a) (b)

Figure 6.5: (a) special affine signature (b) full affine signature $\overline{\gamma'(t)}$

6.2.2 Global Affine Signatures for Curves in 3D

To construct special affine signatures for spatial curve we use invariants J_1 and J_2 given by Eq.(5.9). Similarly to 2D case, the special affine signature of a spatial curve $\beta(t)$ is obtained by, first, evaluating J_1 and J_2 on this curve and then plotting the parameterized curve $(J_1(t), J_2(t))$ in $\mathbb{R}^2$.

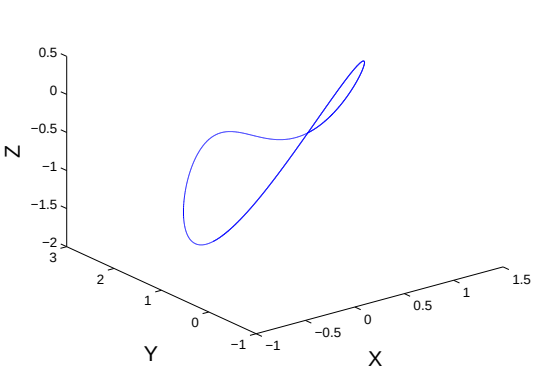

(a)

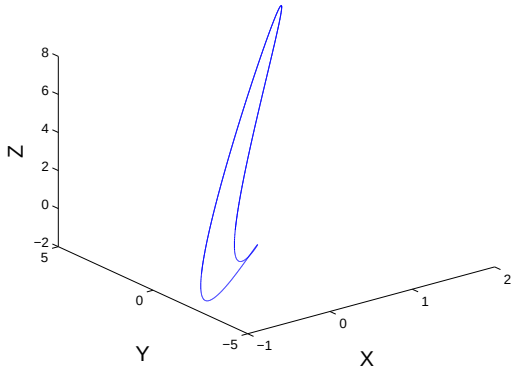

(b)

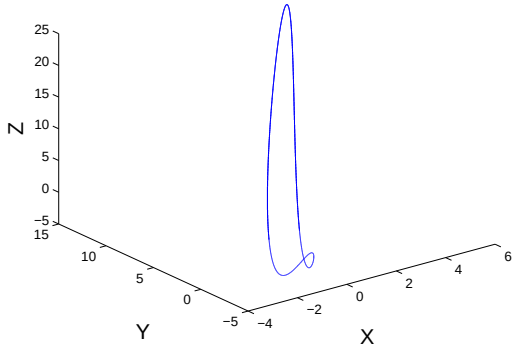

(c)

Figure 6.6: (a) original curve $\beta(t)$ (b) special affine transformed curved $\overline{\beta(t)}$ (c) full affine transformed curved $\overline{\beta_a(t)}$

For example, the signature of a space curve $\beta(t) = (\sin t - 1/5\ \cos^2 t + 1/5,\ 1/2\ \sin t - \cos t + 1, \sin^2 t + \cos t - 1)$, shown in Figure 6.6-a, is the planar curve shown on Fig 6.7. A curve $\overline{\beta(t)}$ (shown in Figure 6.6-b) is obtained from β by a special affine transfor-

mation $\begin{pmatrix} 0.3816 & 0.7631 & 1.1447 \\ 1.9079 & 1.5263 & 2.2894 \\ 2.6710 & 3.0526 & 3.4341 \end{pmatrix}$, and a curve $\overline{\beta_a(t)}$ (shown in Figure 6.6-c) is obtained from β by a full affine transformation $\begin{pmatrix} 1 & 2 & 3 \\ 4 & 5 & 6 \\ 9 & 8 & 7 \end{pmatrix}$. As Fig 6.7 illustrates, the special affine signatures of $\beta(t)$ and $\overline{\beta(t)}$ coincide. The full affine signatures of all three curves are shown in Fig 6.8.

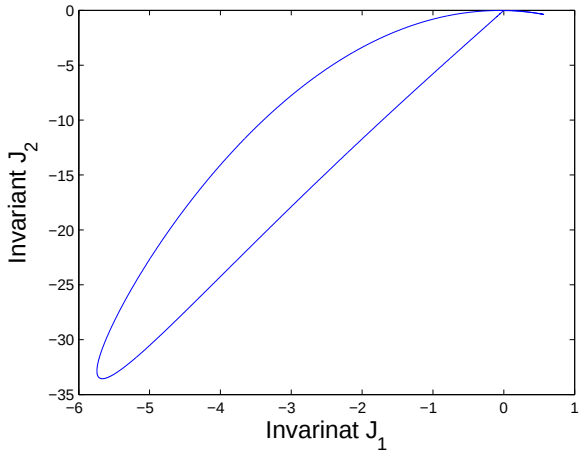

Figure 6.7: Signatures for $\beta(t)$ and $\overline{\beta(t)}$ coincide.

As for the 2D case, the full affine signature is obtained by normalizing the special affine invariants by the range of $|J_1|$.

$$\tilde{J}_1(t) = \frac{|J_1(t)|}{\max_t |J_1|}, \quad \tilde{J}_2(t) = \frac{J_2(t)}{\max_t(J_1^2)}. \tag{6.2}$$

The full affine signature of a spatial curve $\beta(t)$ is obtained by, first, evaluating $\tilde{J}_1$ and $\tilde{J}_2$ on this curve and then by plotting the parameterized curve $\left(\tilde{J}_1(t), \tilde{J}_2(t)\right)$ in $\mathbb{R}^2$.

The advantage of global signatures is their independence of parametrization, whereas the result of evaluation of invariants J_1 and J_2 on a curve depends on the

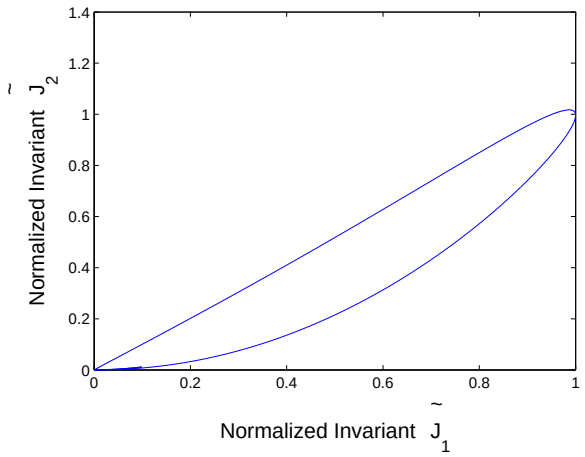

Figure 6.8: Full Signatures for $\gamma(t)$, $\overline{\beta(t)}$, $\overline{\beta_a(t)}$

choice of parametrizations similarly to I_1 and I_2 in 2D case. The disadvantage of global signatures is in their dependence on the choice of the initial point. The local signature construction proposed in the next section overcomes this dependence.

6.3 2D and 3D Local Affine Integral Invariant Signatures

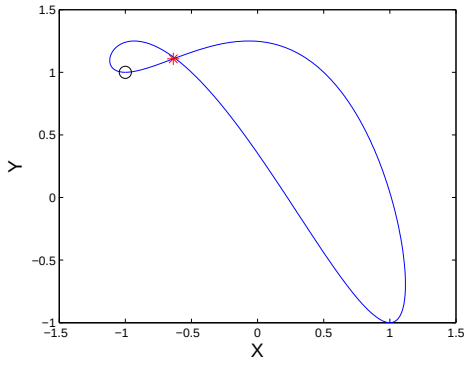

Figure 6.9: A planar curve with two different choices of the initial points

The signatures defined in the previous section can not be used for classification

purpose unless the initial point of a curve is known. This becomes an obstacle for closed curves comparison or for matching parts of contours. For illustration let us choose two different initial points, a black circle or a red star, on the planar curve in Figure 6.9. The resulting global affine signatures are different as illustrated in Figures 6.10-a and Figures 6.10-b. We overcome the dependence on the initial point

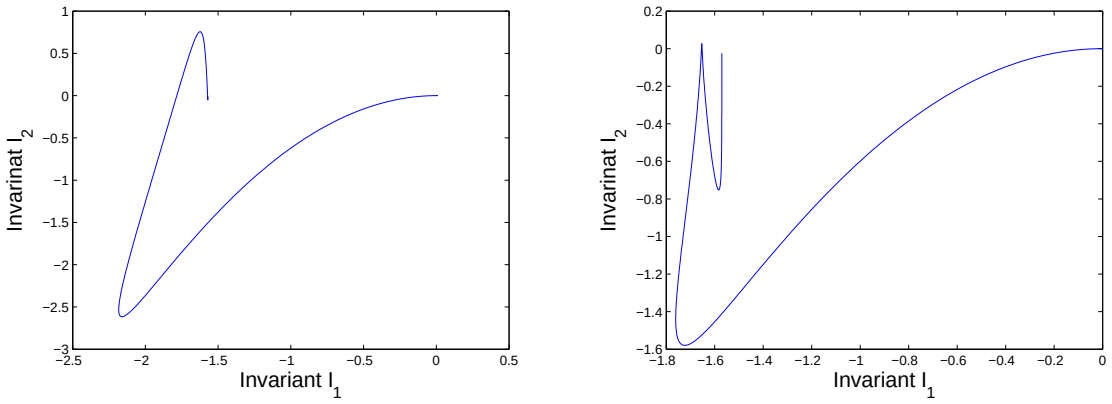

(a) (b)

Figure 6.10: (a) The global signature for the curve in Fig. 6.9 whose initial point is the black circle (b)The global signature for the curve in Fig. 6.9 whose initial point is the red star

by introducing local signatures. To proceed with the local signature construction, we replace the integration from an initial point by an integration on local segments. To retain an affine invariant property of the signatures, we have to partition the curve while preserving an invariants. Such partition may be achieved using the notion of affine arc-length from classical differential geometry, which is preferably to avoid in practical computations. We propose to use the lowest order integral invariants, namely I_1 for plane curves and J_1 for spatial curve to obtain an equi-affine partition of a given curve. The details are described next.

6.3.1 Local Affine Signatures for curves in 2D

We will use I_1 to partition a given curve into equi-affine sub-segments. Assume that γ is parametrized by $t \in [a, b]$. For this purpose, we define an evaluation of

invariants on sub-segments of γ. Recall that integration in the integral variables is performed from an initial point $\gamma(a)$ to a current point on the curve $\gamma(t)$. For instance, $I_1(t) = \int_a^t X dY - \frac{1}{2}XY$, where $X = x(t) - x(a)$ and $Y = y(t) - y(a)$. Thus $I_1(t)$ is a function from $[a, b]$ to $\mathbb{R}$:

$$I_1 : [a, b] \mapsto \mathbb{R}$$

We define the evaluation of an invariant on sub-segments of γ by defining the starting point of a segment as the initial point and the end as the upper limit of the integral. In particular, for a sub-segment defined by a parameter range $[p, q] \subset [a, b]$ the localization

$$I_1^{[p,q]} = \int_p^q (x(t) - x(p))\, dy(t) - \frac{1}{2}\,(x(q) - x(p))\,(y(q) - y(p))$$

, and similarly for invariants I_2 and I_3 defined by Eq.(4.5). We note that the evaluation of an invariant on a segment is a real number.

We first choose a sufficiently small $\Delta > 0$, and define an equi-affine partition $a = t_0 < t_1 < \cdots < t_N = b$ of the curve $\gamma(t)$, $t \in [a, b]$, to obtain sub-segments satisfying the condition

$$|I_1^{[t_{i-1},t_i]}| = \Delta.$$

In practice, we choose Δ proportionally to the maximum of the absolute value of I_1, i.e. we choose an integer N and set $\Delta = \frac{\max_t |I_t|}{M}$. Note that the total number N of segments that we obtain generally differs from M. The *local discrete special affine signature* of γ is defined by evaluation of I_2 and I_3 on the intervals $[t_{i-1}, t_i]$, $i = 1..N$, that is a set of points with coordinates $\left(I_2^{[t_{i-1},t_i]}, I_3^{[t_{i-1},t_i]}\right)$ $i = 1..N$. Figure 6.11 illustrates that the local discrete special affine signature for the curve shown in Fig 6.9, with different starting points coincides.

To obtain *local discrete affine invariant signature* of γ we need to use scaling invariant normalizations of I_2 and I_3, that is to plot $\left(\frac{I_2^{[t_{i-1},t_i]}}{max_t(I_1^2)}, \frac{I_3^{[t_{i-1},t_i]}}{max_t|I_1|}\right)$ $i = 1..N$.

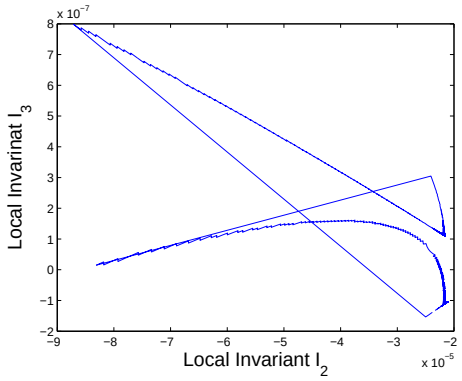

Figure 6.11: Local invariants based signature for curves in Fig. 6.9

6.3.2 Local Affine Invariant Signatures for curves in 3D

For spatial curves we proceed in a similar manner as for plane curves. We use invariant J_1 to partition a curve $\gamma(t), t \in [a, b]$ into N sub-intervals defined by $a = t_0 < t_1 < \cdots < t_N = b$ defined by the condition $J_1^{[t_{i-1},t_i]} = \Delta$, $i = 1..N$, where $\Delta > 0$ is proportional to the maximum of the absolute value of J_1. We define a local special affine signature by evaluation of J_2 and J_3 on the intervals $[t_{i-1}, t_i]$, $i = 1..N$, that is by a set of points on the plane with coordinates $\left(J_2^{[t_{i-1},t_i]}, J_3^{[t_{i-1},t_i]}\right)$ $i = 1..N$.

Figure 6.12-b shows the local special affine signature for a curve shown on Figure 6.12-a. The signature does not depend on our choice of initial point.

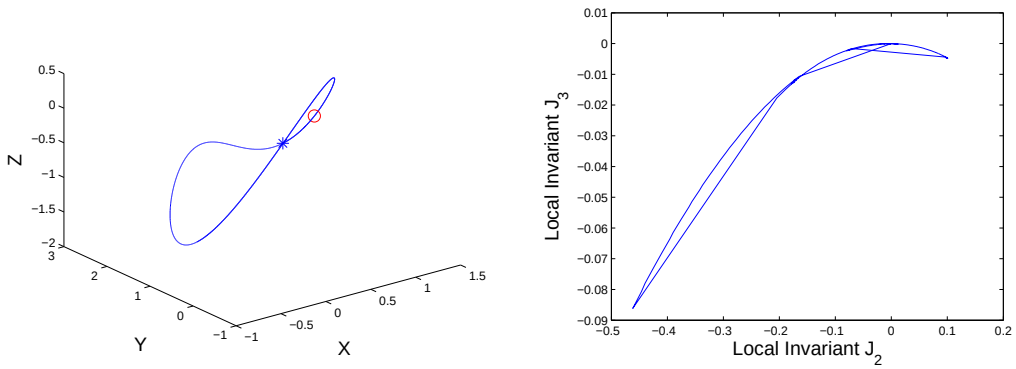

(a) Two choices of the initial point (b) Local special affine signature

Figure 6.12: A curve and its local special affine signature

6.3.3 Local Euclidean Invariant Signature in 3D

Local Affine Invariant Signature was defined in the previous subsection, and may be used to classify curves in 3D up to affine transformation. However, many objects may only undergo Euclidean transformation. An Affine invariant signature is over qualified to classify curves under Euclidean transformation, and may in fact affect the numerical accuracy due to the complexity of J_2. A much simpler Euclidean Invariant Signature is required. A 2D Euclidean Intelgral Invariant Signature has been developed in [33], while 3D counterpart has yet to appear.

For a closed/open space curve in 3D, the scaling effect may be canceled by normalizing the total arch length to be 1. Similarly to [33], we also focus on local regions to make the signature independent of the starting point of a curve. The local regions are obtained by dividing a curve into small segments of equal arch length. To construct a signature, two invariants are required for each segment. However, the area criterion in [33] is not easily defined for space curves in 3D, requiring us to adopt a different strategy, namely the Moving Frame approach [13].

In our development of 3D special affine invariants, we have several Euclidean invariants in Eq.(5.4). Two of them are picked to construct a Euclidean Invariant Signature:

$$\begin{aligned} ie_1 &= \overline{X} = \sqrt{X^2 + Y^2 + Z^2}, \\ ie_2 &= \overline{Z}_{010} = \frac{\left(XYZ - 2\,XZ_{010} + 2\,YZ_{100} - 2\,ZY_{100}\right)^2}{4\sqrt{X^2 + Y^2 + Z^2}}. \end{aligned}$$

Simplifying ie_1 and ie_2 yield two Euclidean Invariants IE_1 and IE_2:

$$\begin{aligned} IE_1 &= ie_1 = \sqrt{X^2 + Y^2 + Z^2} \\ IE_2 &= \sqrt{4ie_1ie_2} = XYZ - 2\,XZ_{010} + 2\,YZ_{100} - 2\,ZY_{100} \end{aligned}$$

Since one end of the segment coincides with the origin, IE_1 is the Euclidean distance between two end points. Instead of area in [33], IE_2 is some volume defined

for the segment.

The integral signature of a space curve in 3D is the variation of one independent invariant I_1, evaluated on the curve, relative to another I_2.

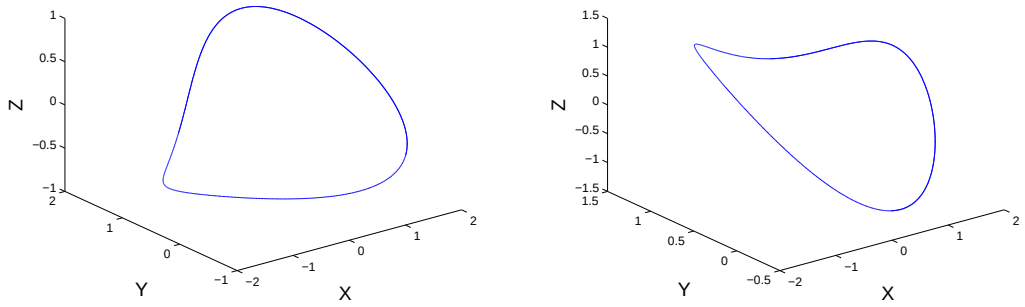

(a) (b)

Figure 6.13: (a) Original curve (b) Transformed curved (Rotation angles $\theta = \phi = \psi = \frac{\pi}{9}$)

The signature of two versions (in Fig. 6.13) of a curve under a Euclidean transformation is shown in Fig. 6.14.

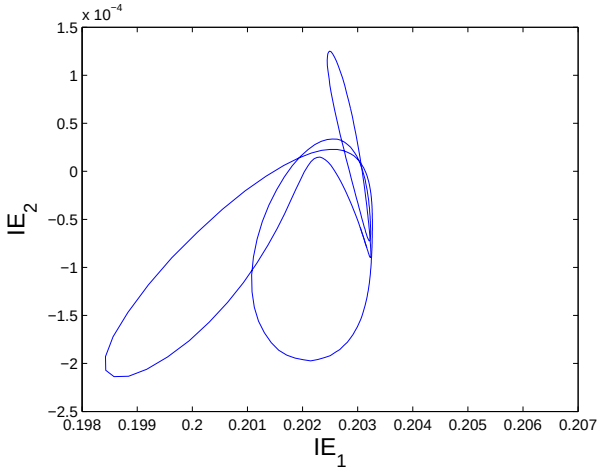

Figure 6.14: Integral Invariant Signature for curves in Fig. 6.13.

Table 6.1: Classification error rate with same parametrization, same initial points

Noise variance	I_1	I_2	Global signature	Local signature
$\sigma = 0.5$	**0.0022**	0.0472	0.06	0.07
$\sigma = 1$	**0.04**	0.12	0.15	0.17
$\sigma = 2$	**0.0789**	0.2233	0.28	0.32

Table 6.2: Classification error rate with different parametrization, same initial points

Noise variance	I_1	I_2	Global signature	Local signature
$\sigma = 0.5$	*0.42*	*0.61*	**0.06**	**0.07**
$\sigma = 1$	*0.48*	*0.70*	**0.15**	**0.17**
$\sigma = 2$	*0.56*	*0.83*	**0.28**	**0.32**

6.4 Robustness Analysis

Similarly to Section 5.5.2, we analyze the robustness of both invariants and signatures in the same experimental setting. Three classification experiments are carried out with different noise variance, namely $\sigma = 2$(Fig. 5.5.2), $\sigma = 1$, and $\sigma = 0.5$. The first experiment uses a common parametrization and initial point for both the training and testing, while in the second experiment, we choose different parameterizations (samplings) for the testing data. In the third experiment, we choose both different parameterizations (samplings) and different initial points for the testing data. The classification error rates of the three experiments with are shown in Table 6.1,Table 6.2,Table 6.3.

In Table 6.1, both integral invariants and the signatures perform well as indicated by the error rates. Since the order of integral variables involved in I_2 is higher than I_1, as well as the explicit form of I_2 is more complicated than that of I_1, the performance of I_2 is not as good as I_1. And the global signature is constructed with both I_1 and I_2, and the local signature is based on I_2 and I_3. The performance of signatures is

Table 6.3: Classification error rate with different parameterization, and different initial points

Noise variance	I_1	I_2	Global signature	Local signature
$\sigma = 0.5$	*0.87*	*0.95*	*0.95*	**0.07**
$\sigma = 1$	*0.91*	*0.97*	*0.97*	**0.17**
$\sigma = 2$	*0.94*	*0.98*	*0.98*	**0.32**

therefore slightly worse than I_2.

If the parameterizations are not the same, the plot of invariants I_1 and I_2 with respect to a parameter can not be used for classification purposes, as illustrated in Table. 6.2. Even with the lowest noise variance, the error rates are greater than 0.4 for I_1 and 0.6 for I_2. However, both the global signature and a local signature are not affected.

If the initial points of a curve are selected differently, both individual invariants(I_1 and I_2) and a global signature have poor performance as shown in Table 6.3. Only local signature may be used to characterize a curve.

As a conclusion, if the training data and testing data have similar parameterization and same initial point, either invariants or signatures may be used. Under different parameterization, the global signature is the best choice. With an unknown starting point, the local signature is the only solution.

Chapter 7

Applications of Integral Invariants and Signatures

The motivation of the integral invariant development is its import to specific applications, namely finding invariant features of 2D/3D facial images for classification. We have derived 3D integral invariants and signature in Chapters 5 and 6, for applications where objects may be subject to geometric transformations. So long as the features are curves, the geometric transformations of feature curves may be eliminated by the corresponding integral invariants or signatures.

In this chapter, we introduce several 3D applications. The first one is biometric application in face recognition, where 2D integral invariants are used to eliminate the pose effect. In the second application, a 3D Euclidean integral invariant signature is used to match objects with articulated parts. 3D Euclidean and affine integral invariant signatures are reapplied to face recognition to eliminate both the pose effect and the facial expression effect, and a dramatic performance improvement is achieved.

7.1 Application of 2D Affine Integral Invariant: pose invariant face recognition

7.1.1 Face recognition

Face recognition has been extensively studied for over 30 years, and its complexity together with its timely relevance in security and surveillance problems have recently led to a renewed research interest. Techniques in 2D face recognition abound, and Zhao and Chellappa [52] provide a fairly comprehensive account of the state of the art. Lighting and pose in 2D face recognition are widely recognized to be major impediments to the deployment of robustly performing algorithms. Specifically, the performance of many existing algorithms greatly deteriorates when the training and testing sets do not share a significant number of common viewing and lighting conditions. The recently developed 3D scanning techniques are believed to provide a potential to alleviate the limitation due to lighting and pose, and their rapid deployment would go far in paving the way for a viable recognition system. Exploiting such data amounts to extracting intrinsic geometric information of faces and utilizing it as the basis for characterizing and distinguishing them.

Recent research activity in 3D and multi-modal face recognition techniques is reviewed in Chang *et al.*[9]. We can distinguish two main classes of data driven techniques:

- A 3D (geometric-only) approach includes a curve and profile-based description of a face by Nagamine *et al.*[35] and Baumier [3], a curvature feature-driven technique by Gordon [19], a registration and mean differences of depth comparison approach by Lao [28], a volumetric approximative representation of a face proposed by Irganoglu *et al.* [24] and a Iterative Closest Point based algorithm by Cook et al. [10] .

- A multi-model (geometric and photometric) approach includes several PCA based methods. Chang *et al.*[8] implement PCA for both 3D and 2D images, Tsalakanidou *et al.*[46] extract depth and color eigenfaces, and Bronstein, Bron-

stein and Kimmel [5] use an eigen decomposition of flattened textures and Multidimensional scaling (MDS)-based canonical images. Also related is 3D Point Signatures and 2D Garbor Filter responses based technique proposed by Wang [50]. Lu and Jain [31] jointly exploit range and texture information with a Linear Discriminant Analysis to construct a hierarchical system.

We propose in the next subsection a novel technique which bases an accurate description of a face range image on a set of curves intrinsic to the 3D surface. To better contend with face pose variability, we propose to derive in subsection 7.1.3 integral invariants as associated features to characteristic curves of a face . The affine invariance provides robustness of curves to rotation, scaling and shearing. With a set of such invariants in hand, we demonstrate that a relatively small set of such features for a face, is sufficient for its accurate representation. Subsection 7.1.4 discusses the use of these features in a face comparison task by way of Discrimination Analysis and Jensen-Shanon divergence measure. A photometric invariant is proposed in subsection 7.1.5. To take advantages of both this and the geometric invariants, we discuss fusion in three steps in subsection 7.1.6. Illustrating examples are provided in subsection 7.1.7.

7.1.2 Facial Curve Feature Extraction

Data Set

The experimental data we are using in this paper consists of three data subsets from the University of Notre Dame Biometrics database[38]. One subset henceforth referred to as S_1, comprised of 10 subjects, each with 2 3D range images along with corresponding 2D color images per subject, is selected as the experimental set to be analyzed by way of its extracted features. Another subset S_2 of 105 range images and gray-scale images from 35 subjects is used as the testing set to validate the feature selection procedure in S_1 and to test its performance in a recognition task. The performance is analyzed on the basis of the population size. The third set S_3 contains all of the subjects in UND database with more than 3 scans. There is a total

of 120 subjects. The performance is evaluated with the help of Set S_3.

Facial Curve Extraction

The 3D range image data from the database are in a form of a point cloud as shown in Fig. 7.1-a. Using the 3D coordinates for all points in a given cloud (or face), we process the raw data to obtain a 3D triangular mesh as shown in Fig. 7.1-b.

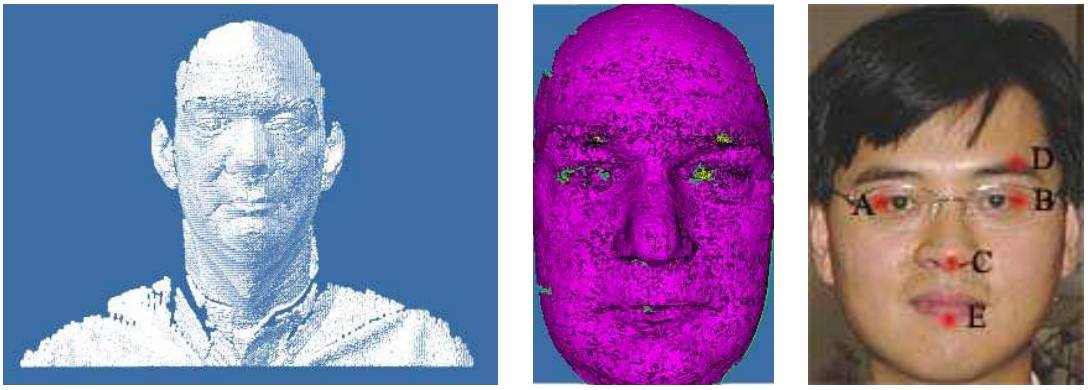

(a) (b) (c)

Figure 7.1: (a)Typical Range image in the database, (b) Face triangulated mesh and (c) Feature points location.

The curve feature extraction proceeds in the vertical and horizontal directions for each representative mesh image embedded in a Euclidean reference frame. The region of interest is delineated by five feature points, namely two outer corners of the eyes, the tip of the nose, the upper end of the eyebrows, and the lower end of the lower lip as illustrated in Fig. 7.1-c. While the localization of these feature points may be achieved automatically, we carry it out manually in the sequal.

A feature curve is defined as the intersection of a plane with the surface of a face. A total of 35 vertical and 35 horizontal planes are used. The vertical planes are perpendicular to the straight line joining the two eye corners A and B as illustrated in Fig. 7.1-c. These are uniformly placed at equal distance from the the left corner of the face to the center of the face. The two eye corners A, B and the nose tip C define a reference plane. The Horizontal planes (Fig. 7.2) are perpendicular to the intersection line of the reference plane and the vertical plane (Fig. 7.2), which range

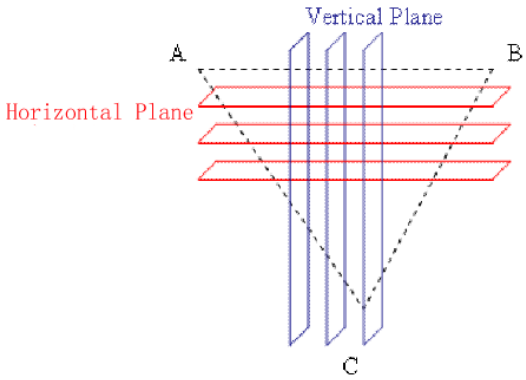

Figure 7.2: Vertical planes and horizontal planes

from the eyebrows D to the mouth E. The 70 vertical and horizontal curves which are collected for each face are shown in Fig. 7.3.

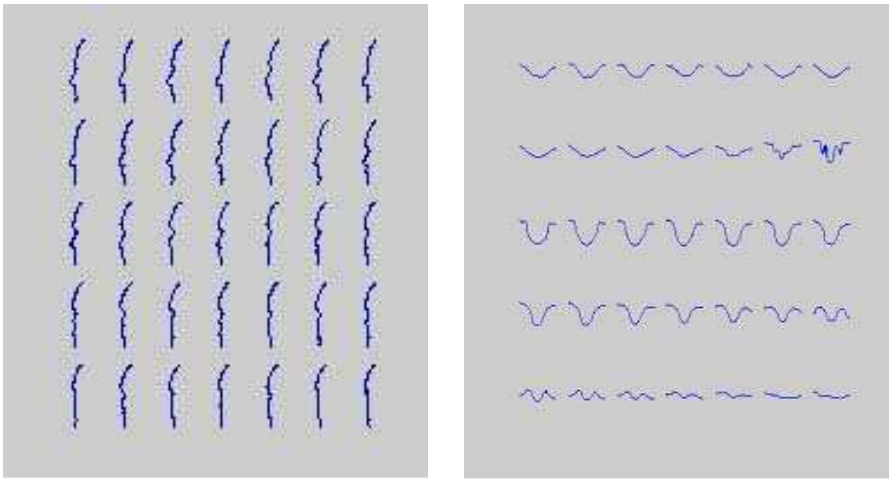

(a) (b)

Figure 7.3: Vertical(a) and Horizontal(b) Curves of a face surface.

7.1.3 Integral Invariant

Curves may be subjected to transformations as a result of a variation in pose of a subject. The transformations include translation, scaling, rotation and shearing.

This clearly impacts the performance of any face recognition procedure, whenever a different set of reference templates are invoked. It is hence important to rather describe these feature curves by invariants which are insensitive to any potential transformation.

The feature curves of interest here are plane curves, hence necessitating affine transformations. Affine Integral invariants were proposed by Hann and Hickman [21], and reinterpreted in this effort in Chapter 4.

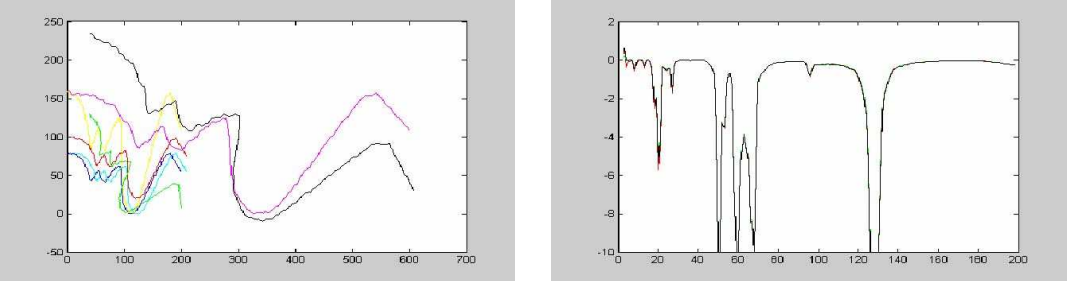

(a) (b)

Figure 7.4: (a)Various affine transformations of a curve (b) Corresponding and coinciding affine integral invariants

An example is shown in Fig. 7.4-a. The solid line curve is the original face profile curve whereas all other styled line curves correspond to its various affine transforms. The associated affine integral invariants are computed and displayed in Fig. 7.4-b, and shown to coincide.

As previously noted, a total of 70 curves are extracted for each face in set $S1$ and 70 corresponding invariants are computed. The vertical set of invariants is shown in Fig. 7.5. Due to regions of missing data on the face range image, large (noise) spikes may appear as may be seen in Fig. 7.5(a). Smoothing of these spikes may be effected in one of two ways: interpolating the raw data domain to smooth over the missing data regions, or by thresholding the invariants and thereby eliminating the spikes directly as demonstrated in Fig. 7.5(b).

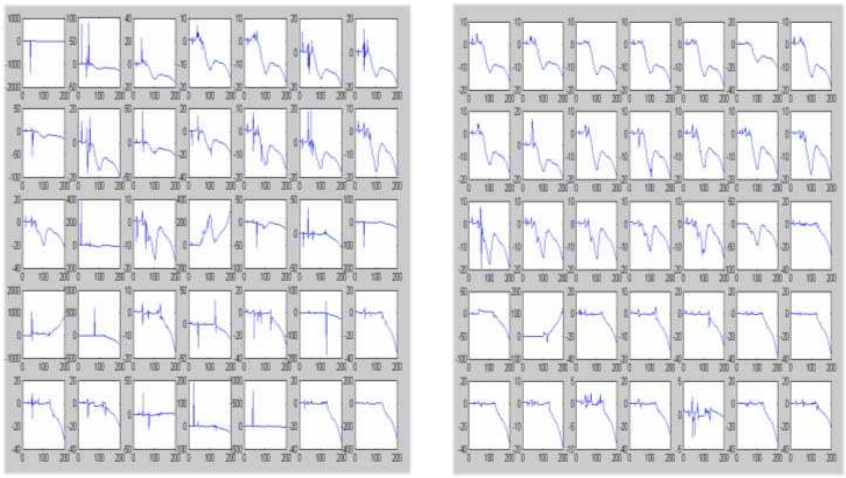

(a) (b)

Figure 7.5: Integral invariant for one vertical curve set(a) Spike removal results(b).

7.1.4 Feature curve selection and analysis

As previously noted, a total of 70 curves are extracted for each face in set $S1$ and 70 corresponding invariants are computed. The vertical set of invariants is shown in Fig. 7.5. Due to regions of missing data on the face range image, large (noise) spikes may appear as may be seen in Fig. 7.5(a). Smoothing of these spikes, as noted above, may be effected in one of two ways: interpolating in the raw data domain to smooth over the missing data regions, or by thresholding the invariants and thereby eliminating the spikes directly as demonstrated in Fig. 7.5(b).

Upon obtaining the set of invariants, a natural question which arises is about the discrimination power of such features among different faces as well as how to quantitatively evaluate such a measure. To that end, we propose a statistical robust approach which effectively evaluates the clustering of features for a given subject face. Two measures will be specifically exploited, one being that of a scatter ratio in Discriminant Analysis and the other is Jensen Shannon Divergence measure of dissimilarity between invariant curves [22, 29].

Discriminant Analysis

Discriminant analysis unveils directions that are efficient for discrimination. The entire invariant curve set is

$$\{\vec{\kappa}_{i,j}^{k} | i \in [1, N], j \in [1, M], k \in [1, K]\}$$

where i is the subject index set, k is the observation index for each subject, and j is the index of extracted curves of each face. For set S_1, N is 10, K is 2 and M is 70. The vertical invariant set is $\{\vec{\kappa}_{i,j}^{k} | k \in [1, 35]\}$ and the horizontal invariant set is $\{\vec{\kappa}_{i,j}^{k} | k \in [36, 70]\}$.

The overall mean of each feature invariant curve set is defined as:

$$\vec{m_j} = \frac{\sum_{i=1}^{N} \sum_{k=1}^{K} (\vec{\kappa}_{i,j}^{k})}{KN}.$$

The mean of a feature invariant curve set for each subject is:

$$\vec{m_{i,j}} = \frac{\sum_{k=1}^{K} \vec{\kappa}_{i,j}^{k}}{K}.$$

The inter-class scatter $\tilde{S}_{Bj}$ and the intra-class scatter $\tilde{S}_{Wj}$ are defined as

$$\tilde{S}_{Bj} = \sum_{i=1}^{N} K(\vec{m}_{i,j} - \vec{m}_j)^T (\vec{m}_{i,j} - \vec{m}_j), \tag{7.1}$$

$$\tilde{S}_{Wj} = \sum_{i=1}^{N} \sum_{k=1}^{K} (\vec{\kappa}_{i,j}^{k} - \vec{m}_{i,j})^T (\vec{\kappa}_{i,j}^{k} - \vec{m}_{i,j}). \tag{7.2}$$

A good characteristic measure will exhibit a large inter-class scatter to better distinguish subjects, and a small intra-class scatter to reflect the similarity/coherence of feature for the same subject. The ratio J_j is hence a good candidate measurement

for the quality of each feature.

$$J_j = \frac{\tilde{S}_{Bj}}{\tilde{S}_{Wj}} \tag{7.3}$$

Jensen-Shannon Divergence Analysis

As a special case of Jensen-Renyi Divergence[22], Jensen-Shannon Divergence is a powerful tool to measure the similarity of Probability Density Functions(pdf). Invariant curves may easily be normalized (e.g., by translation and scaling) to satisfy the non-negativity and the integrability properties of a pdf. Such processing simplifies the comparison of invariant curves to subsequently yield a quantitative measure of clustering of intra-class features relative to inter-class features. Thus identifying each $\vec{\kappa}^k_{i,j}$ with $p^k_{i,j}$, we may proceed to compute such a measure which we would expect to be large for two different subjects and small for a positive recognition. An inter-class divergence JSD_{Bj}, and an intra-class divergence $JSD_{Wi,j}$ yield a divergence ratio JSD_j. It is an alternative measurement for feature quality.

$$JSD_{Bj} = S\left(\sum_{i=1}^{N}\sum_{k=1}^{2}\pi_i p^k_{i,j}\right) - \sum_{i=1}^{N}\sum_{k=1}^{2}\pi_i S(p^k_{i,j}), \tag{7.4}$$

$$JSD_{Wi,j} = S\left(\sum_{k=1}^{2}\pi_i p^k_{i,j}\right) - \sum_{k=1}^{2}\pi_i S(p^k_{i,j}), \tag{7.5}$$

$$\text{where } S(p) = -\sum_{l=1}^{L} p_l log p_l, 0 \leq \pi_i \leq 1, \sum_{i=1}^{N}\pi_i = 1,$$

$$JSD_j = \frac{JSD_{Bj}}{\sum_{i=1}^{N} JSD_{Wi,j}}, \tag{7.6}$$

Feature Invariant Selection

Scatter and divergence ratios reflect the importance of each feature. The number of relevant and required curve invariants to fully represent a face is also an important parameter to determine. The classification performance of a face recognizer may for instance be used to unravel this parameter. Such a classifier is implemented as a Nearest Neighbor (NN) Classifier in Euclidean Space using a Ł^2 distance as the metric. On account of the small size of the data set, Leave-One-Out Cross (LOOC)-validation[27] is adopted as the procedure of choice.

Starting with an invariant corresponding to the largest scatter ratio J_j, we progressively increase the set of accounted features by one in correspondence to a decreasing J, and simultaneously monitor the performance of the NN classifier with Leave-One-Out Cross-validation. We note that this performance dramatically changes with the first few features and subsequently reaches a state of small fluctuations as illustrated in Fig. 7.6-a.

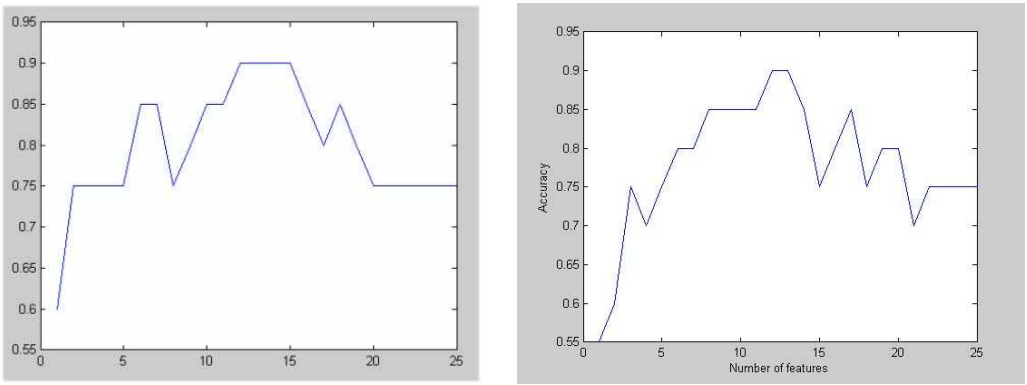

(a) (b)

Figure 7.6: (a) Classification performance as a function of feature selection by Scatter ratio and (b) Classification performance using a JSD ratio.

Carrying out the same procedure using Jensen Shannon Divergence ratio yields similar results shown in Fig. 7.6-b.

In comparing Figs. 7.6-a and Figs. 7.6-b, it is interesting to see that the graphs, albeit different both indicate that a *best* performance is achieved with a total of 12 curve invariants. The 12 curves selected by both approaches coincide albeit chosen

in a different order. 10 out of the 12 feature curves are vertical curves, namely curves 10, 12, 15, 25, 27, 29, 30, 32, 33 and 35. The two horizontal curves are curves 15 and 30. The feature curve locations are depicted in Fig. 7.7.

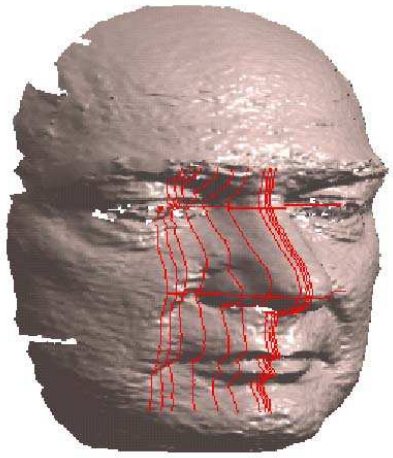

Figure 7.7: feature curve locations.

That the vertical curves contribute to the classification more significantly as indicated by the above results, is an interesting point. Most of the distinguishable vertical feature are located near the face center profile (32, 33, 35), center (10, 12, 15) and corner (27, 29, 30) of eye regions. The two horizontal curves (15,30) also characterize the eye and nose. While the psychophysical interpretation of this result is certainly significant, we defer this discussion to a future study.

Dimension Reduction

The dimension of each vertical and horizontal feature vector is 200, making each of the 12 feature curve invariants a 1x2400 long feature vector. Fully realizing the presence of redundant information in such a vector, and towards reducing the computational load of our approach, we proceed to project our feature data onto a lower dimensional space with no loss in classification performance. To that end, we first construct a covariance matrix of feature vectors K_j for each curve set (at a location),

$$K_j = \left[\vec{\kappa}^1_{1,j},\ \cdots,\ \vec{\kappa}^K_{1,j},\ \cdots,\ \vec{\kappa}^1_{N,j},\ \cdots,\ \vec{\kappa}^K_{N,j}\right].$$

We subsequently define a matrix **D** (mean) whose columns are given by the following vector

$$\vec{m}_j = \frac{1}{NK} \sum_{i=1}^{N} \sum_{k=1}^{K} \vec{\kappa}_{i,j}^{k}.$$

A covariance matrix may hence be constructed as

$$C_j = (K_j - M)^T (K_j - M), \tag{7.7}$$

where T denotes the transpose operation on a matrix.

Performing a PCA analysis on the covariance matrix, and identifying the most significant Eigen values, defines our non-redundant space of interest. Our Experiments show that the first 8 eigenvectors may be used to characterize every feature invariant curve set to achieve the same performance as that using the full feature space. This procedure effectively reduces the complexity from a 2400 dimension to a 96 dimension.

7.1.5 Photometric Invariant

In the UND Biometric face database, each 3D range image has a corresponding 2D intensity image. The five feature points marked in both the 3D range image and the 2D intensity image guide the mapping of photometric information to the 3D surface. Thus, each of the feature curves is associated with its color information.

The intensity values may change dramatically as a result of variation of lighting conditions. It is important to have a photometric invariant to improve the recognition performance.

Towards obtaining a photometric invariant, we adopt a Lambertian model assumption, which is effectively a simplified BRDF (Bidirectional Reflectance Distribution Function). It defines the image intensity as a product of surface texture or albedo (ρ), a surface normal ($\vec{n}$) and a lighting source ($\vec{s}$): $I = \rho(x, y)\vec{n} \cdot \vec{s}$.

We may also assume the normals of neighboring points at a smooth and continuous surface to be nearly equal ($\vec{n}_k \approx \vec{n}_{k-1}$), which makes the ratio of the intensity values

of two neighboring points a good approximation of the ratio of albedos [36]. Along a sampled feature curve with n points, the photometric invariant is the reflectance ratio of neighboring points, which is defined as:

$$p_k = \frac{I_k}{I_{k-1}} = \frac{\rho_k \vec{n}_k \cdot \vec{s}}{\rho_{k-1} \vec{n}_{k-1} \cdot \vec{s}} \approx \frac{\rho_k}{\rho_{k-1}}, k \in [2, n] \tag{7.8}$$

An intensity ratio does not carry chromatic information. The chromatic information also characterizes the human face, which has a great potential to improve the recognition rate. A conceptual similar idea may be used to to define the ratio in RGB color space. The albedo at each point is redefined as a tuple: (ρ_R, ρ_G, ρ_B). Each primary, R, G or B could be presented in the same form with corresponding ρ_R, ρ_G, and ρ_B in the following equations:

$$R = \rho_R(x, y)\vec{n} \cdot \vec{s}, \tag{7.9}$$

$$G = \rho_G(x, y)\vec{n} \cdot \vec{s}, \tag{7.10}$$

$$B = \rho_B(x, y)\vec{n} \cdot \vec{s}. \tag{7.11}$$

The lighting effect is canceled in the ratio of each primary due to the similarity of the norms of neighboring points. And a new photometric feature is R, G and B ratios, namely, p_k^R p_k^G and p_k^B.

$$p_k^R = \frac{\rho_k^R}{\rho_{k-1}^R}, k \in [2, n], \tag{7.12}$$

$$p_k^G = \frac{\rho_k^G}{\rho_{k-1}^G}, k \in [2, n], \tag{7.13}$$

$$p_k^B = \frac{\rho_k^B}{\rho_{k-1}^B}, k \in [2, n]. \tag{7.14}$$

Another color space option is XYZ space, which is based on direct measurements of the human eye, and serves as the basis from which many other color spaces are defined. Since the transformation between XYZ space and RGB space is linear, it is easy to show that the ratio property still holds in XYZ space. Similar ratios p_k^X p_k^Y and p_k^Z may therefore be defined.

For each geometric feature vector/curve, we now have a corresponding photometric feature vector, which could be either the intensity ratio, or ratios for various primaries in RGB or XYZ space.

7.1.6 Fusion

Geometric features and Photometric features are complementary with each other. Taking advantage of both is expected to dramatically improve the performance. Fusion of such information may be implemented in three stages [39], namely feature extraction level, matching score level and decision level.

Geometric and photometric invariants are independent. Thus, a newly constructed vector using a combined geometric ($\vec{f_G}$) and photometric ($\vec{f_P}$) features has a great potential to improve the performance. Scaling factors α and $(1 - \alpha)$ balance the geometric and photometric features for optimized performance to result in,

$$\vec{f} = \begin{bmatrix} \alpha\vec{f_f} \\ (1-\alpha)\vec{f_P} \end{bmatrix}. \tag{7.15}$$

At the matching score level, the dissimilarity measure is a Euclidean Distance. A linear combination of the geometric dissimilarity (D_G) and photometric dissimilarity (D_P) is a good dissimilarity measure containing both information:

$$D = \alpha D_G + (1 - \alpha) D_P \tag{7.16}$$

At the decision level, a strategy is designed on the basis of recognition results from the geometric classifier and photometric classifier. The confidence level of the geometric classifier makes the decision. Geometric classifier dominates if the confidence level is high, which is equivalent to choosing $\alpha = 1$ in the first two levels. Low confidence results in photometric classifier dominance ($\alpha = 0$). Fig. 7.8 shows the architecture of the decision level fusion system. The definition of confusion is discussed in the next section.

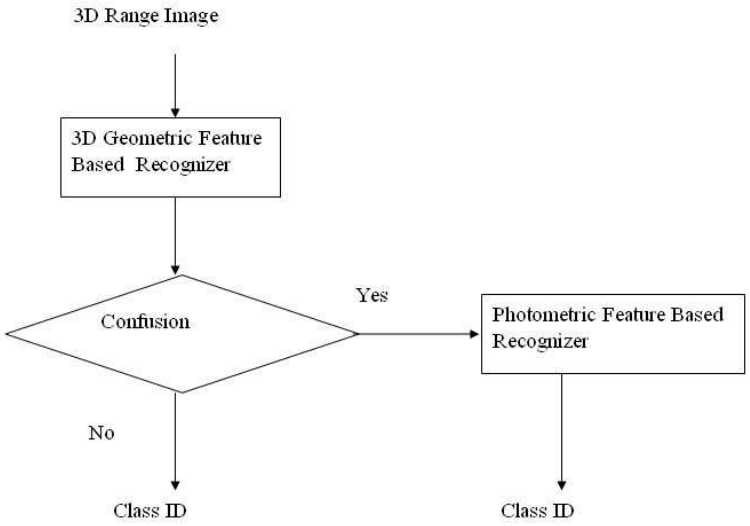

Figure 7.8: Decision level fusion architecture

7.1.7 Performance Analysis

The analysis of set S_1 indicates that a 3D face may be represented by a geometric invariant feature vector together with a photometric invariant feature vector. The performance is to be evaluated using the testing set $S2$.

Geometric Only Classifier

Out of the 70 feature curves for each face in set $S2$, the invariants of 12 feature curves are calculated and projected onto eigenvectors as described in Sec. 4.4 to

Table 7.1: Accuracy for Geometric feature based recognition.

Training:Testing		1:4	2:3	3:2	4:1
1NN	Max	0.8714	0.9143	0.9429	1.0000
	Min	0.7500	0.7810	0.8000	0.8000
	Mean	0.8061	0.8571	0.8857	0.9143
3NN	Max			1.0000	1.0000
	Min			0.8429	0.8571
	Mean			**0.9214**	**0.9286**

generate a 96 dimensional feature vector.

The ratios between the training data and testing data are set to be $1:4$, $2:3$, $3:2$, and $4:1$. We randomly pick the training set on the basis of this ratio and implement the 1NN and 3NN classifier to test the performance. For each ratio, the experiment is repeated 100 times. As a result, the maximum, minimum and average performances are listed in Table. 7.1.

Table 7.1 indicates that 3NN classifier outperforms 1NN classifier. As the training set size increases, the performance is dramatically improved. With 3 or 4 training 3D scans per subject, the accuracy can reach 92%.

Fusion System

Using the geometric only classifier, 3NN with more than 3 training data per subject achieves the best performance. Thus, the same setting is applied to the fusion system. All of the three level fusions in the previous section are tested.

The class label is assigned by majority voting rule, which helps to define the confusion in the decision level fusion. If in the geometric system, all the the three nearest neighbors are from the same class (subject), no confusion is considered ($\alpha = 1$). Otherwise the geometric system is considered as confused, and the photometric system is called upon to help disambiguate the geometric system output. The performance is listed in Table 7.2. The average performance is greater than 98%, which outperforms the geometric system alone.

Balancing the α in Eq. 2.16 affects the matching level fusion accuracy as shown in Fig. 7.9. The best performance (around 99%) is achieved when α is between 0.35

Table 7.2: Accuracy for fusion at decision level.

Training:Testing		3:2	4:1
3NN	Max	1.0000	1.0000
	Min	0.9286	0.9429
	Mean	**0.9829**	**0.9886**

and 0.5. The feature extraction level fusion could also achieve the same performance with different α range.

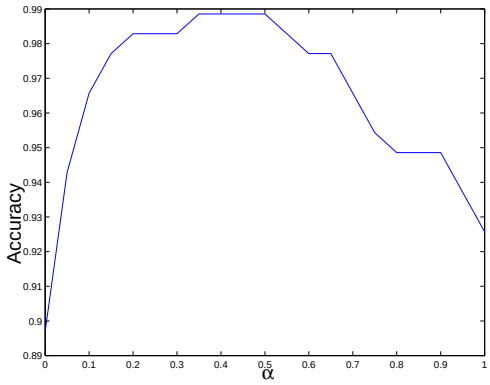

Figure 7.9: accuracy for similarity level fusion

The accuracy for a fusion system at every level is around 99%. Since nearest Neighbor is a very basic classifier, the performance may be further improved by e.g., a Support Vector Machine Classifier.

Large data set verification

The set S_3 has 120 subjects and four scans for each subject. The same procedure described above is applied to S_3. Three scans from each subject are randomly selected as training data and the forth is testing data. The decision level fusion experiment is repeated for 100 times, and the accuracy is listed in Table 7.3.

As the number of subjects increases, the accuracy decreases slightly. When chromatic information is added, the performance increases. And the performance in the XYZ space is slightly better then the RGB space. Our results are numerically comparable with recently proposed geometry and photometry driven techniques[38].

Table 7.3: Accuracy for face set S_3.

3NN	3D	3D+2D(I)	3D+2D(RGB)	3D+2D(XYZ)
Min	0.8583	0.9333	0.9417	0.9417
Max	0.9833	1.0000	1.0000	1.0000
Average	0.9175	0.9745	0.9853	0.9867

As a conclusion, we presented a new geometric and photometric invariants based method for 3D face recognition. An affine integral invariant of each facial curve is not affected by translation, scaling, rotation and shearing distortion of 3D faces. The reflectance ratio cancels the lighting factors to remain the albedo property. Our experiments indicate that the human face can be characterized by 12 affine invariant curves along with the corresponding reflectance ratio curves, which are located near the face center profile, center and corner of eye regions. Fusion of geometric information and photometric information at any of the three levels results in a performance better than 98% by a 3-NN classifier. However, in this approach, only pose has been taken care of. Facial expression may still affect the performance. A more robust approach will be discuss in Section 7.3.

7.2 3D Euclidean Signature: 3D object matching

7.2.1 Application Background

3D Object representation and classification have been extensively studied. However, geometric transformations, such as Euclidean, Isometric, or affine transformation, on objects often constitute a great challenge to the problem. Geometric Invariants have, as a result, been of great research interest.

2D invariants for Euclidean group, affine group and projective group have been developed for 2D computer vision and pattern recognition problems. The most classical Euclidean invariants are the Curvature and Torsion, whose practical utilization is limited due to their high sensitivity to noise. To smooth noise out, a variety of integral invariants [42, 30, 32, 21] were proposed. Among them, [32] developed a robust integral invariant signature, which is independent of parameterization and initialization

of curves.

Recently developed 3D scanning techniques have offered increased accuracy and wider availability of 3D data. It has resulted in an increasing research interest in 3D applications. However, 3D invariants has far less been studied than 2D. To the best of our knowledge, no 3D integral invariants have been proposed in the past, and our goal here is to propose such invariants, which are not only robust to noise, but also quite amenable to applications where 3D Euclidean transformations and, then isometric transformations are involved.

To that end, and inspired by [32], we derived in Section 6.3.3 a novel integral invariant signature for 3D Euclidean transformation, which may in turn be used to classify curves undergoing isometric transformation as discussed next. In Section 7.2.3, we discuss a potential application of this signature to extracted iso-geodesic curve features from 3D objects for a subsequent object matching application. Experimental results are shown in Section 7.2.4. We provide some concluding remarks in Section 7.2.5.

7.2.2 3D Integral Invariant Signature

A 3D object may be represented by a set of space curves [23] [40], implying that invariants of 3D object/2D surface may be investigated by way of invariants of space curves in 3D. For a closed/open space curve in 3D, the scaling effect may be cancelled by normalizing the total arch length to be 1, and an integral invariant signature developed in Section 6.3.3 may be used to classify curves (objects) undergoing Euclidean transformations.

The integral Invariant Signature is developed for Euclidean transformations. For objects under isometric transformations, such as those in Fig. 7.12, curves on the surfaces of objects also undergo isometric transformation globally (Fig. 7.10). However, locally, most segments are under Euclidean transformation. And only the articulated parts, such as the region near the two stars in Fig. 7.10, are transformed isometrically. In this case, we can still use the integral invariant signature to characterize surfaces. The Euclidean transformed segment will display a similar signature. The only dif-

ference will be in the isometric transformed segment, which highlights an important additional information, the location of the articulation. For example, the signatures of the two curves in Fig. 7.10 are shown in Fig. 7.11. Note that the signatures for the most parts overlap. The only different regions near the star correspond to the articulate regions in Fig. 7.10. Any similarity measurement may indicate that these two signatures are highly similar. An application of matching iso-geodesic curves from isometric transformed objects is presented in the next section.

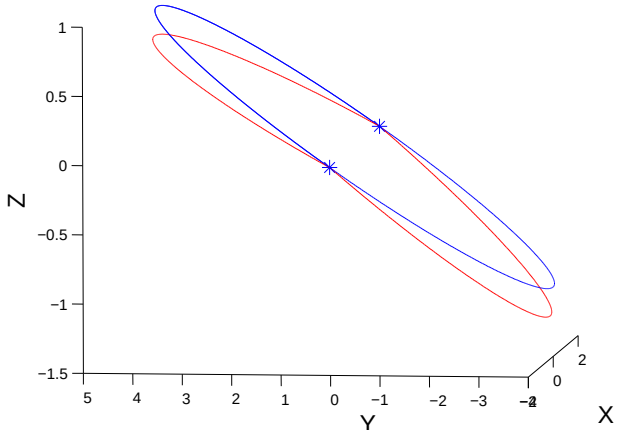

Figure 7.10: Curves undergo isometric transformation

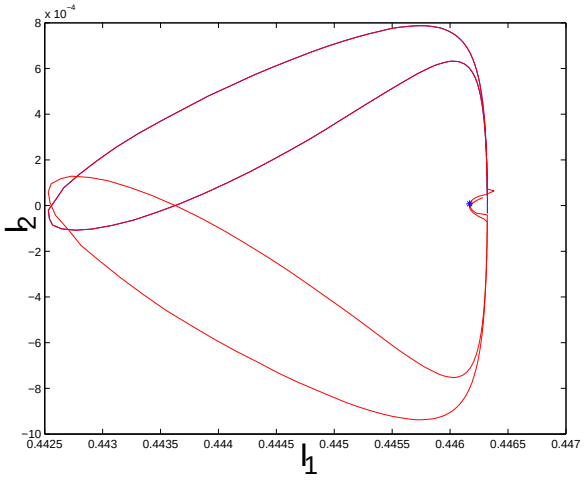

Figure 7.11: Signature for Curves undergoing isometric transformation

7.2.3 Matching Iso-geodesic Curves

Problems of curve matching under transformations arise in many applications. In the present example, we consider an application of matching 3D objects based on a set of characteristic spatial curves.

Data set

The McGill 3D Shape Benchmark[51] provides a repository of 3D shapes,which includes models with articulating parts. We pick a subset of 25 models from 5 objects (in Fig. 7.12) in data set I (Objects with articulating parts). This subset is picked to verify the robustness of the integral invariant signature to match objects under both Euclidean Transformation and Isometric transformation.

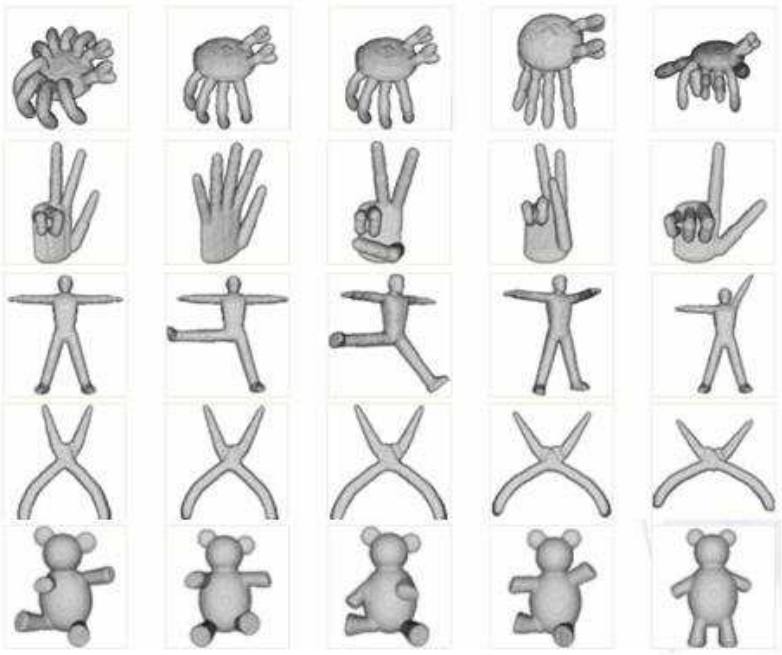

Figure 7.12: a subsets of objects under Isometric transformation

Curve Based Object Representation

3D object representation has been extensively studied, and various approaches [11] have been proposed in the literature. When 3D objects are subject to transformations, especially Isometric transformation, most representations will vary for the same object. It is well known that a Geodesic distance between points on the surface is invariant to isometric transformation. This property has been exploited in several approaches [12] [47] [25][20]. Most of them, however, require predefined feature points. [23] and [2] characterized a 2D surface by integrated distance, which is independent of any feature point. We adopt here the Global Geodesic Function(GGF) defined in [2] to guide the curve extraction, i.e., object characterization.

Global Geodesic Function

A Global Geodesic Function(GGF) is proposed in [2] to characterize a surface invariantly to arbitrary isometric transformation.

A 3D object may be represented by a triangular mesh with a $m * 3$ vertex matrix V and face matrix F. For any two vertices $v_i \in V$ and $v_j \in V$, the geodesic distance between them is written as $d(v_i, v_j)$. The integrated distance for a vertex v_i is defined as,

$$g(v_i) = \sum_{j=1}^{m} d(v_i, v_j)\delta S_j.$$

GGF is defined as a normalized integrated distance function, and written as,

$$\begin{aligned} g_n(v_i) &= \frac{g(v_i)}{\max_{j=1,\ldots,m} g(v_j)} \\ &= \frac{\sum_{j=1}^{m} d(v_i, v_j)\delta S}{\max_{j=1,\ldots,m} \sum_{k=1}^{m} d(v_j, v_k)\delta S} \\ &= \frac{\sum_{i=1}^{m} d(v_j, v_i)}{\max_{i=1,\ldots,m} \sum_{k=1}^{m} d(v_i, v_k)}, \end{aligned} \tag{7.17}$$

where the subscript n denotes normalization. Normalization bounds the GGF be-

tween 0 and 1. And the GGF of several objects in Fig. 7.12 are shown in Fig. 7.13 with a color code. The color of the object in Fir. 7.13 indicates the GGF value at each point on the surfaces of the object. One may observe that no isometric transformations on an object will affect its GGF distribution. This will in fact help us in extracting the iso-geodesic curves, irrespectively of the changes.

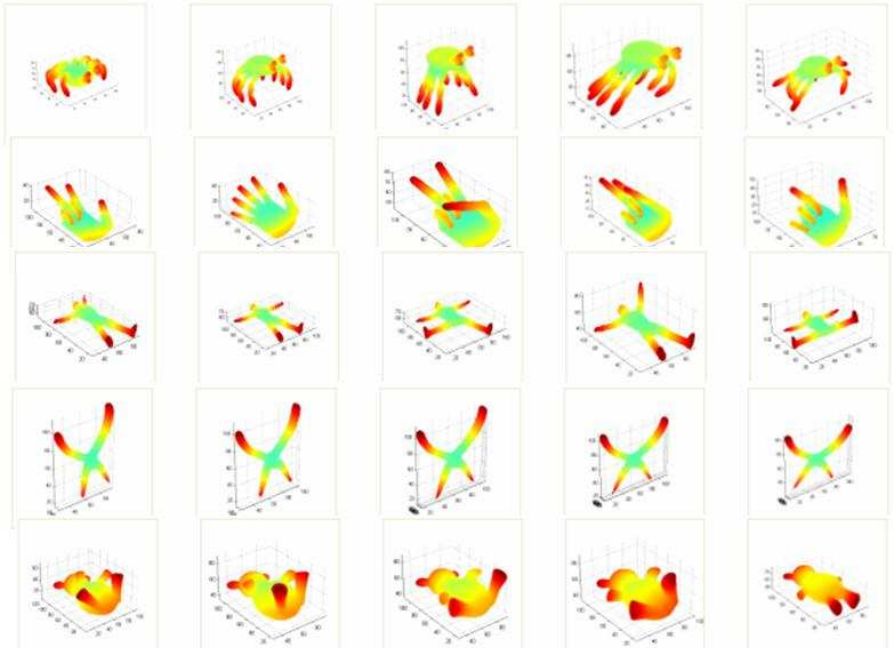

Figure 7.13: GGF for objects in Fig. 7.12

Iso-Geodesic Curves

GGF is a continuous function on the surface of an object. Within the surface, iso-geodesic curves of level c_i are defined as curves satisfying the following condition,

$$g_n(v) = c_i.$$

For a discrete surface, the vertex with the exact level c_i may not exist. However, under a reasonable assumption that the GGF is distributed linearly along each edge, the vertex with an exact level c_i may be interpolated linearly. Specifically, it follows

two steps:

1) Locate the edge

For any edge starting from v_s and ending at v_e, calculate,

$$S = (g_n(v_s) - c_i)(g_n(v_e) - c_i)$$

Under the linearly distributed assumption of a GGF, it is easy to see that c_i is located on the edge where $S \leq 0$.

2) Locate the vertex by linear interpolatation

Once an edge is selected in step 1, the exact location of a vertex may be linearly determined as:

$$v_{c_i} = \frac{c_i - g_n(v_s)}{g_n(v_e) - g_n(v_s)}(v_e - v_s) + v_s.$$

The iso-geodesic curves at level c_i may be generated by connecting the vertices on the same face and nearby faces sharing the same vertex. Several examples of iso-geodesic curves of surfaces are shown in Fig. 7.14 as space curves in 3D. Each color indicates one level $c_i = \max(g_n(v))\frac{i}{n}$ for a total of 20 levels, where $n = 20$ and $i = 1, 2, ..., n$.

Curve Matching

The Iso-geodesic curves capture the same sets of points under translation, rotation, scaling and isometric transformations. As such, it is a robust to representation of 3D objects, and the object matching problem is solved by comparing the similarity of space iso-geodesic curves. Comparing curves under transformations is not so trivial. And a direct comparison requires registration, which is usually time consuming, especially for object under isometric transformation. Using an integral invariant signature, space curves in 3D are mapped to a 2D invariant space, where there are no transformation effects, and the curve matching is reduced to matching signatures. A signature curve is parameterized by arch-length starting at the $\min(I_1)$ point, and the signature may be represented by a vector. The Euclidean distance is used to measure

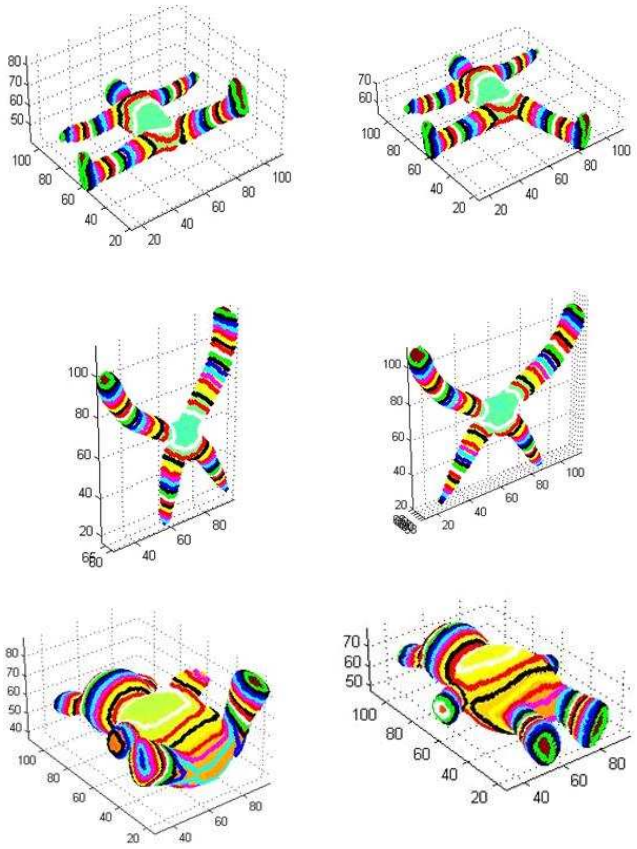

Figure 7.14: Examples of iso-geodesic curves of 3D articulated objects

the similarity between signatures.[1] And the similarity between objects is obtained as a weighted sum of similarities between sets of curves.

Experimental Result

Following the above three steps, we may achieve a similarity matrix of all objects in Fig. 7.12 (normalized by the largest Euclidean distance for display purpose). The darker color of the blocks indicates a large similarity between the same objects under transformations. Although the objects themselves have articulated parts and the global transformation is an isometric transformation, most local regions are under Euclidean Transformations. Integral Invariant signatures characterize well the local

[1] An improved metric would be a geodesic metric in the space of signature curves.

features of the iso-geodesic curves for object matching.

We add Gaussian noise ($N(0, 0.01)$) to the objects and repeat the experiment to yield the result shown in Fig. 7.16. As a reference, the similarity matrix based on differential signature (curvature v.s. torsion) is shown in Fig. 7.17. In the noisy data case, it is easy to observe that the differential signature has a worse object matching performance, with the integral signature still matching objects successfully.

As a short conclusion, Integral Invariant Signature may be used to characterize space curves in 3D. Integral signatures obviate effects of a transformation, of parametrization, and also provide additional information, such as locations of the non-Euclidean isometric changes. An application to matching of iso-geodesic curves of a 3D object as they are subjected to isometric transformation is considered. And the matching similarity matrixes are shown to verify the robustness of 3D Integral Signature.

7.3 3D face signature: affine invariance to pose and facial expression invariant face recognition

7.3.1 Face representation

A general 3D object representation has been extensively studied, and various approaches [11] have been proposed in the literature. When faces are subjected to transformations, especially Isometric transformation (under effect of pose and facial expression), most representations will vary for the same subject. The vertical and horizontal curves-based representation we proposed in Section 7.1 is only pose invariant, and the effect of facial expression will hence affect its performance. It is well known that a Geodesic distance between points on a surface is invariant to isometric transformations. This property has been exploited in several approaches [12] [47] [25][20],[2] and [6] , [41], [34] extend this idea to face recognition since it is invariant to facial expression as verified in [6], [34]. We exploit here a similar idea to guide the curve extraction, and construct a curve-based 3D face representation.

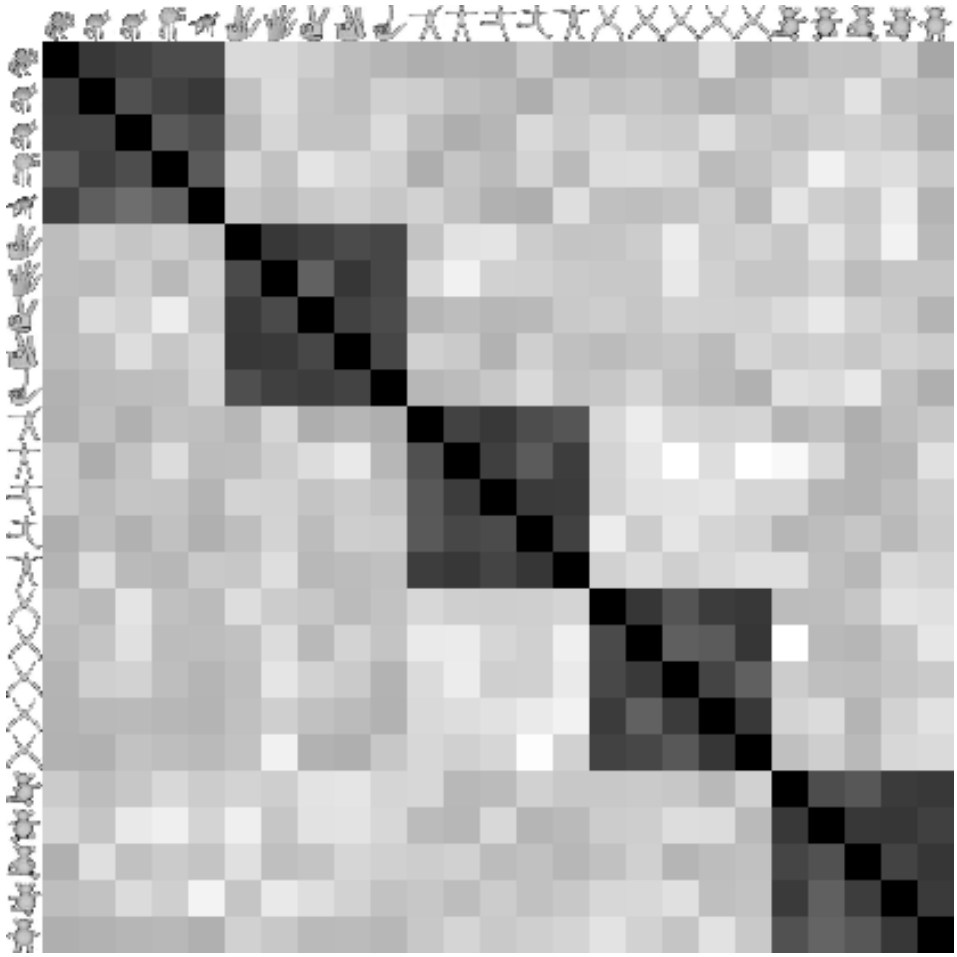

Figure 7.15: The color coded similarity matrix for integral signature in a noise free scenario

Geodesic Distance Function

A geodesic distance between two points on a manifold is the shortest path between these two points along the manifold. Although the Euclidean distance between two points may change under different facial expressions, the geodesic distance, only changes very slightly [6], [34], and the changes may be ignored. We, hence, may predefine the nose tip as a reference point, and the Geodesic Distance Function(GDF) at any point on the 3D face is defined as the geodesic distance between this point and the nose tip.

The movement of the mouth poses a practical problem in that an opening mouth

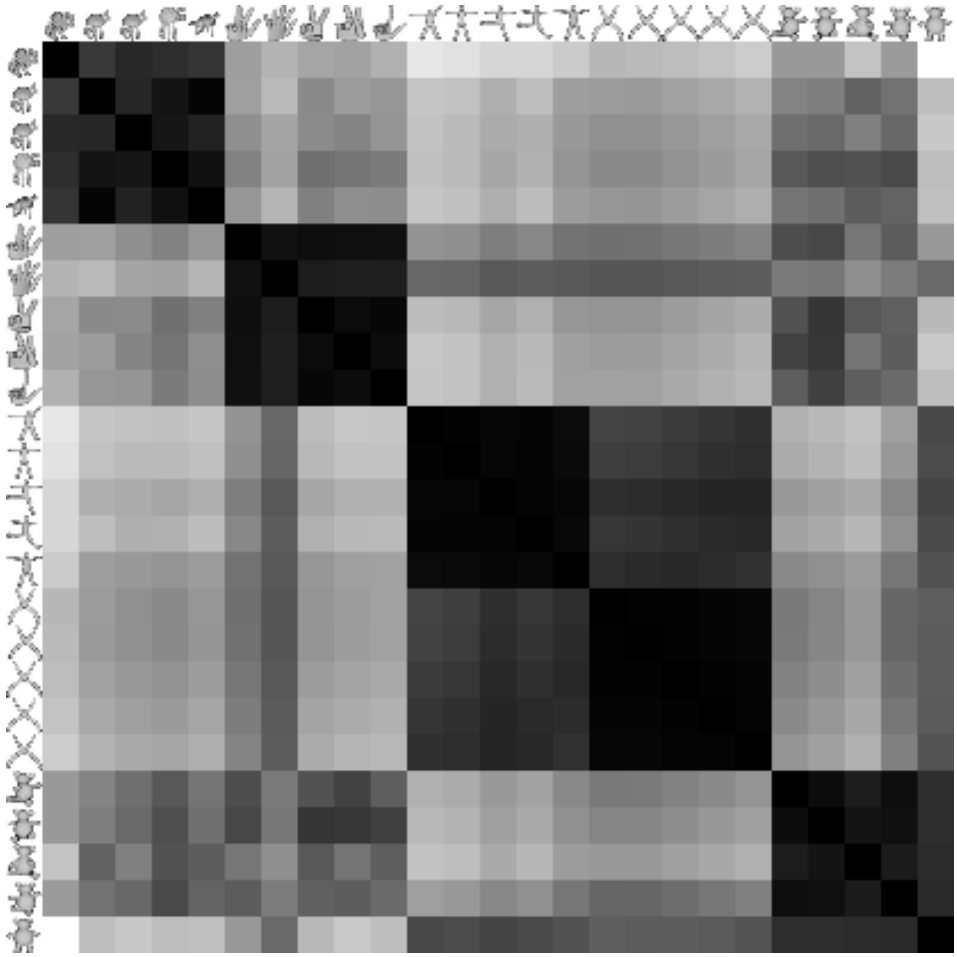

Figure 7.16: The color coded similarity matrix for integral signature in a noisy scenario

may generate a hole to change the topology of the face. The geodesic distance from the nose tip to the area under the mouth may hence change as a result of the opening mouth. One possible solution is suggested in [6] to remove the mouth region, and to always assume there is a hole. As such, a mouth is easy to locate with texture information, and the test data we are using provides both the geometrical and textural information. Using a level set approach [43], the mouth region may be located in the 2D images (as shown in Fig. 7.19). We map each vertex in 3D back to 2D. If it is located within the mouth contour, we simply delete it from 3D. As a result, the mouth region is removed from the face.

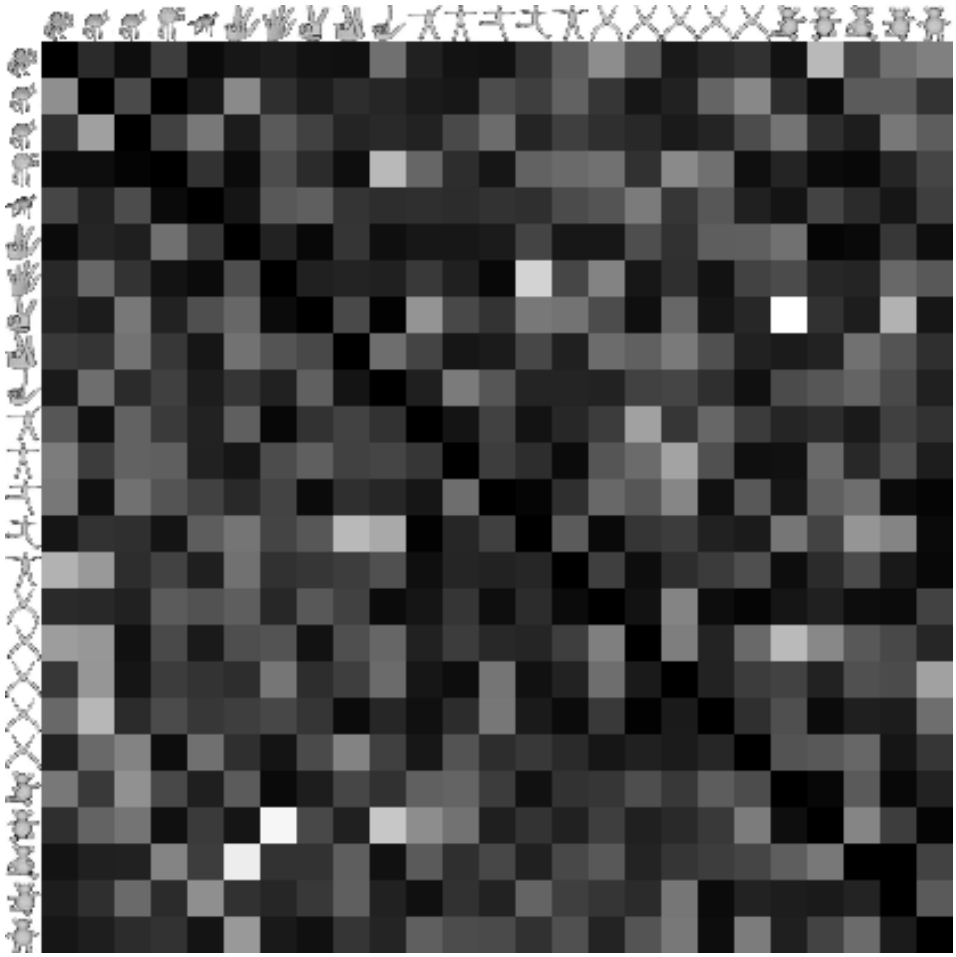

Figure 7.17: The color coded similarity matrix for differential signature in a noisy scenario

The GDF of several faces in Fig. 7.18 are shown in Fig. 7.20 (best viewed in color). The color of the object in Fig. 7.20 indicates the GDF value at each point on the surfaces of the object.

Iso-Geodesic curves

GDF (denoted as g) is a continuous function on the surface of an object. Within the surface, iso-geodesic curves of level c are defined as curves satisfying the following condition:

$$g(x, y, z) = c.$$

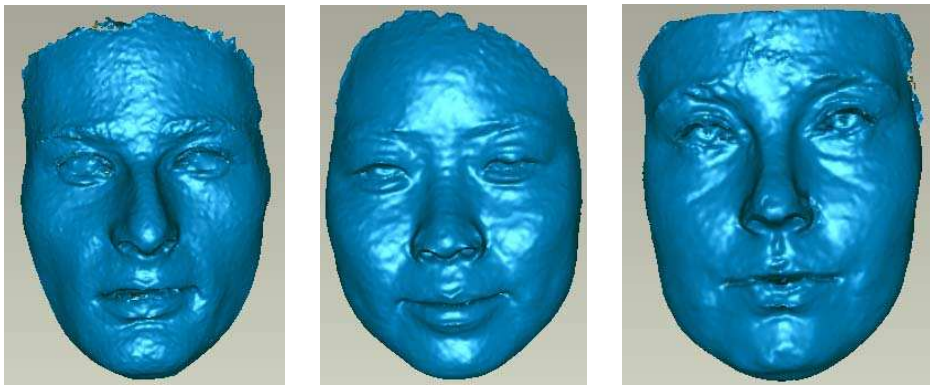

Figure 7.18: 3D faces

Figure 7.19: Mouth region of 2D faces

Let n be the total number of iso-geodesic curves extracted from a face. In our current approach, we set the maximum level c_n to be the curve bounded by the outer corner of the eyes, so that we are only focused on the n curves from the nose tips to the outer corner of the eyes. This covers most of the region of interest in a 3D face.

For a triangulated mesh surface, the vertex with the exact level c may not exist as noted earlier. Under a reasonable assumption that the GDF is a linear function along each edge, the vertex with exact level c may, however, be interpolated linearly. Specifically, it follows the same two steps of Section 7.2.3.

The iso-geodesic curves at level c may be generated by connecting the vertices on the same face and nearby faces sharing the same vertex. Several examples of iso-geodesic curves of surfaces are shown in Fig.7.21 as space curves in 3D. Each color indicates one level $c_i = \max(g_n v)\frac{i}{n}$ for a total of 20 levels (we chose $n = 20$) and $i = 1, 2, ..., n$ in our current experiment.

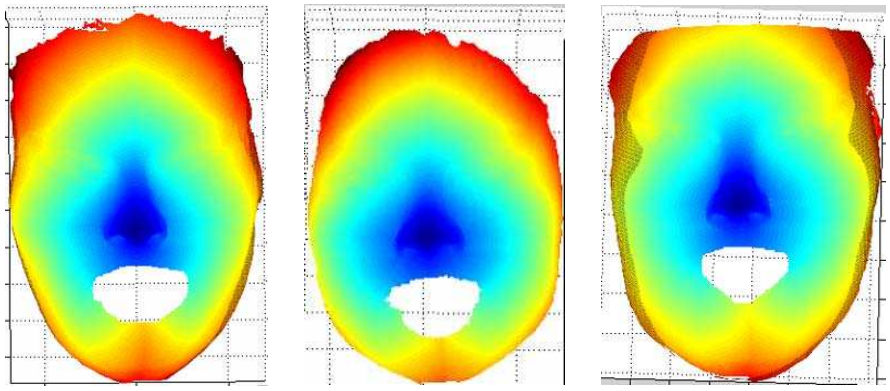

Figure 7.20: Geodesic Distance Function of 3D faces

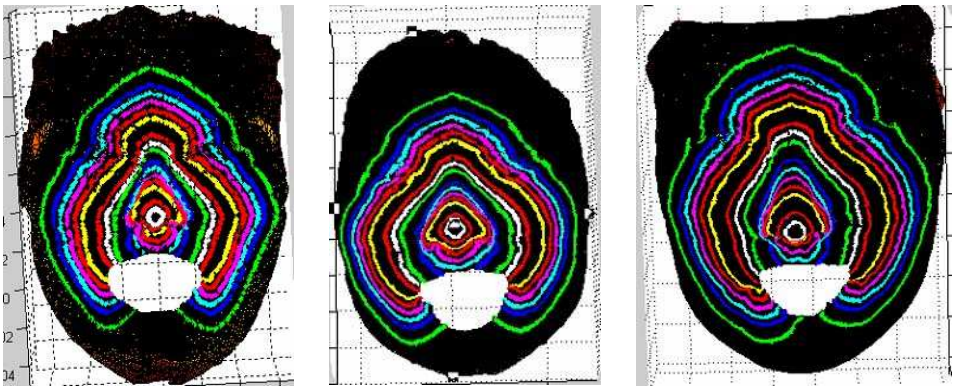

Figure 7.21: Iso-Geodesic curves of different 3D faces

7.3.2 Invariant features

The Iso-geodesic curves capture the same sets of points on a face under different pose and facial expression. As such, it is a robust representation of 3D faces, and the face recognition may be carried out by comparing the space iso-geodesic curves. Space curves undergo transformations, which makes the comparison difficult. A direct comparison of curves, as noted earlier, generally requires registration, further complicating an already difficult task for many important problems. A geometric Invariant is, as a result, a great tool.

In this application, we implement all of the 3D integral invariants and signatures we derived in Chapters 5 and 6, namely invariants J_1 and J_2, Global Affine Signature, Local Affine Signature, and Local Euclidean Signature. The invariants and signatures

serve as Invariants features. The best feature will be determined by the classification performance.

The invariants J_1 and J_2 require an initial point on a curve. In order to define the initial points, we need to use use the nose tip as one reference point. The second reference point is the one located on the mouth contour, which has the shortest Geodesic Distance to the nose tip. With these two reference points, a geodesic path between between the points is constructed, and the initial point for a given level curve is defined as the intersection of the level curve and the geodesic path, as shown in Fig. 7.22.

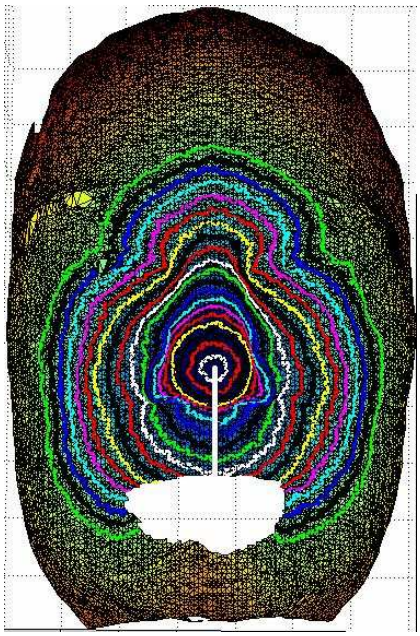

Figure 7.22: Initial points selection

Curve matching

With the integral invariants and signatures, the space curves in 3D are mapped to the 2D invariant space, where there is no transformation effects, and matching space

Table 7.4: Accuracy for face recognition using invariants and signatures.

Invariant Type	J_1	J_2	Global Affine Sig.	Local Euclidean Sig.	Local Affine Sig.
Accuracy	94.81%	89.32%	91.50%	**95.75**%	84.01%

curves under transformation in 3D is reduced to matching signatures. A signature curve is parameterized by arch-length starting at the $\min(I_1)$ point, and the signature may be represented by a vector. The cosine similarity is used to measure the similarity between signatures. And the similarity between objects is the sum of similarities between sets of curves.

7.3.3 Experimental result

The experimental data we are using in this paper is FRGC2 [38]. The data from spring 2003 are the training set, which contains 222 subjects, and the number of scans of each subject varies between 1 to 10. The data from the same 222 subjects are selected from spring 2004, serving as testing data. The number of 3D scans per subject varies from 1 to 12.

Following the procedures in the above two sections, each face is represented by 20 curves and the signature of each curve is constructed and sampled to a 200 dimensional vector. The cosine similarity between corresponding signatures is calculated as the similarity measurement. In this experiment, we use One Nearest Neighbor classification rule, and the accuracy is listed in Table 7.4.

Among them, the best performance (95%) is achieved with 3D Local Euclidean Invariant Signature, which verifies our intuition that facial curves globally undergo a Isometric Transformation, and locally undergo a Euclidean Transformation. In theory, 3D Local Affine Invariant Signature should also work since affine transformation includes Euclidean ones. However, the numerical complexity of the invariants is a practical problem and somewhat affects the performance.

Our result is numerically comparable with the most recently proposed geometry driven techniques in FRVT 2006 Large-Scale Results. By using the integral invariant signature, we successfully avoid the time consuming registration procedure, hence theoretically making our approach more amenable to a fast real time system.

In summary, we presented a new geometric invariant-based method for 3D face recognition. Each face may be represented by 20 iso-geodesic curves, which gives us a systematic way to capture the same sets of points under iso-metric transformations. The pose and facial expression effect may be eliminated by mapping the space iso-geodesic curves to Euclidean integral invariant signature space. Substantiating examples are provided with an achieved classification accuracy of 95%.

Chapter 8

Conclusion and Future work

In this thesis, we reinterpret 2D affine integral invariants, and present a novel 3D development, namely affine mixed invariant and integral invariants. Based on 3D integral Invariants, local signatures and global signatures are proposed. Due to the reduced noise sensitivity properties of integration, the robustness of integral invariants and signatures is a clear advantage. 2D and 3D integral invariants and signatures have been successfully implemented and applied to face recognition and 3D object matching.

In the next section, we summarize the contributions in each of the previous chapters and present the conclusions made from the research work. Potential research directions following this work are discussed in Section 8.2.

8.1 Contribution of the thesis

8.1.1 3D Affine Mixed Invariant

In Chapter 3, we presented a new 3D affine mixed invariant. Compared with the existing differential invariants, its sensitivity to noise reduced since it is based on integrals and only first order derivatives. The computation is in addition simplified with the introduction of first order derivatives. Such invariants present gains in classifying curves in contrast to differential invariants as verified in Chapter 3.3.

8.1.2 2D and 3D Affine Integral Invariants

In Chapter 5, we used an inductive approach to construct affine integral invariants for curves in 2D and 3D in terms of Euclidean invariants. In the 2D case this lad to a new geometric interpretation of previously known invariants, areas and volumes defined by a curve in 2D, whereas the integral invariants for curves in 3D are derived for the first time. One of the 3D affine integral invariants has a clearly defined geometric meaning, volume defined by curves in 3D. Integral invariants were proved to have significantly lower classification error rate than classical differential invariants and mixed invariants.

8.1.3 Integral Invariant Signature

Integral invariants depend on paramterization and initial point selection. In Chapter 6, we present two solutions: Global Integral Invariant Signature and Local Integral Invariant Signature. Global Integral Invariant Signature provides a classification method independent of parameterization (curve sampling). However, Global Integral Invariant Signature still depends on the choice of the initial point. Local Integral Invariant Signature provides a classification method independent of the choice of the initial point, they can be used on images with occlusions and for comparing fragments of the contours. It is slightly more sensitive to noise than Global Integral Invariant Signature.

If the parameterizations are not the same, the integral invariants with respect to a parameter can not be used for classification purpose. However, both the global signature and local signature are not affected. If the initial points of a curve are selected differently, both individual invariants and global signature have poor performance. Only local signature may be used to characterize a curve.

8.1.4 Face Recognition Using 2D Integral Invariants

In Chapter 7.1, we presented a new geometric and photometric invariants based method for 3D face recognition. A 2D affine integral invariant of each facial curve

is not affected by translation, scaling, rotation and shearing distortion of 3D faces. The reflectance ratio cancels the lighting factors to remain the albedo property. Our experiments indicate that the human face can be characterized by 12 affine invariant curves along with the corresponding reflectance ratio curves, which are located near the face center profile, center and corner of eye regions. Fusion of geometric information and photometric information at any of the three levels could result in performance more than 98% by a 3-NN classifier.

8.1.5 3D Object Matching Using 3D Euclidean Integral Invariant Signature

Euclidean Integral Invariant Signature is successfully used to characterize a space curve in 3D. Integral signatures obviate effects of a transformation, a parametrization, and also provide additional information, such as the locations of the non-Euclidean isometric changes. An application to matching of iso-geodesic curves of a 3D object as they are subjected to isometric transformation is considered. And the matching similarity matrices are shown to verify the robustness of 3D Integral Signature.

8.1.6 3D Face Recognition Using 3D Integral Invariants and Signatures

3D face recognition is improved in Chapter 7.3. We presented a new geometric invariant-based method. Each face may be represented by 20 iso-geodesic curves, which gives us a systematic way to capture the same sets of points under iso-metric transformations. The pose and facial expression effect may be eliminated by mapping the iso-geodesic space curves to the Euclidean integral invariant signature space. Substantiating examples are provided with an achieved classification accuracy of 95% with a large data set.

8.2 Future Research

Motivated by this thesis, there are several interesting research directions, which we intend to accomplish in future.

8.2.1 Projective Integral Invariant

Following the development of Euclidean and Affine Integral Invariants, the natural idea is if it is possible to develop projective invariant. Projective Integral Invariant development is one of the potential future research directions. It may help us to better correlate 2D information with 3D data.

8.2.2 Statistical Analysis of Integral Invariant Signature

With the integral invariant signature, the space curves in 3D are mapped to the 2D invariant space as discussed in Chapter 7.2, where there is no transformation effects, and the matching curves is reduced to matching signatures. 3D objects may be represented by a set of iso-geodesic curves. Matching object under transformations, hence, becomes a problem of matching a set of signature curves in 2D.

It seems to be a perfect solution, but the establishment of correspondence may not always be easy. Assume at level c_i in the GGF function, object A has m curves, while object B has n curves. If m is not equal to n, it may not be trivial to establish the best correspondence. One may only compare the $k(k = \min(m, n))$ most similar pairs, but the leftover curves may result in lowing accuracy.

The cardinality difference motivates us to isolate the entire set of curves at a certain level and seek a method to characterize them as such. A potential solution is to construct a probability density function(PDF) of the integral invariant signatures for curves at the same level. The comparison of two set of curves, which may have different cardinalities, is now simplified to comparing between two PDFs. Jensen-Shannon Divergence is an option to measure similarity.

Bibliography

[1] *Sophus Lie's 1884 differential invariant paper*. Math Sci Press, Brookline, Mass., 1976. In part a translation of "On differential invariants" [Über Differentialinvarianten] by S. Lie [Math. Ann. **24** (1884), 537–578], Translated from the German by M. Ackerman, Comments and additional material by Robert Hermann, Lie Groups: History, Frontiers and Applications, Vol. III.

[2] D. Auouada, S. Feng, and H. Krim. Statistical analysis of the global geodesic function for 3d object classification. In *ICASSP*.

[3] C. Beumier. 3D face recognition. In *Computational Intelligence for Homeland Security and Safety*.

[4] M. Boutin. Numerically invariant signature curves. *Int. J. Computer Vision*, 40:235–248, 2000.

[5] A. M. Bronstein, M. M. Bronstein, and R. Kimmel. Expression-invariant 3D face recognition. In *Audio and Video-Based Person Authentication, J. Kittler and M.S. Nixon*.

[6] A. M. Bronstein, M. M. Bronstein, and R. Kimmel. Expression-invariant representations of faces. *IEEE Trans Image Processing*, 2007.

[7] E. Calabi, P.J. Olver, C. Shakiban, A. Tannenbaum, and S. Haker. Differential and numerically invariant signature curves applied to object recognition. *Int. J. Computer Vision*, 26:107–135, 1998.

[8] K. Chang, K. Bowyer, and P. Flynn. Face recognition using 2D and 3D facial data. In *2003 Multimodal User Authentication Workshop*.

[9] K. I. Chang, K. W. Bowyer, and P. J. Flynn. An evaluation of multi-modal 2d+3d face biometrics. *IEEE Transactions on PAMI*, 27:619–624, 2005.

[10] J. Cook, V. Chandran, S. Sridharan, and C. Fookes. Face recognition from 3D data using Iterative Closest Point algorithm and Gaussian mixture models. In *3D Data Processing, Visualization and Transmission*.

[11] C. Dorai and A. Jain. Cosmos-a representation scheme for 3d free-form objects. *IEEE Transactions on Pattern Analysis and Machine Intelligence*, 19, 2003.

[12] A. Elad and R. Kimmel. On bending invariant signatures for surfaces. *IEEE Transactions on Pattern Analysis and Machine Intelligence*, 25, 2003.

[13] M. Fels and P. J. Olver. Moving Coframes. II. Regularization and Theoretical Foundations. *Acta Appl. Math.*, 55:127–208, 1999.

[14] S. Feng, D. Aouada, I. Kogan, and H. Krim. 3D Euclidean Integral Invariant Signature and Its Application on 3D Object Matching. In *submited to ICCV*.

[15] S. Feng, D. Aouada, I. Kogan, and H. Krim. I3D MIXED INVARIANT AND ITS APPLICATION ON OBJECT CLASSIFICATION. In *proceedings of ICASSP*, Honolulu, HI.

[16] S. Feng, I. Kogan, and H. Krim. Integral invariants for 3D curves: an Inductive Construction. In *proceedings of IS&T/SPIE joint symposium*, San Jose, CA.

[17] S. Feng, I. Kogan, and H. Krim. Integral invariants for 3D curves: an Inductive Construction. In *proceedings of IEEE workshop of Statistical Signal Processing*, Madison, WI.

[18] S. Feng, H. Krim, I. Gu, and M. Viberg. 3D Face Recognition Using Affine Integral Invariants. In *proceedings of ICASSP*, Honolulu, HI.

[19] G. Gordon. Face recognition based on depth and curvature features. In *CVPR*.

[20] A. B. Hamza and H. Krim. Geodesic object representation and recognition. In *Proc. International Conference Discrete Geometry for Computer Imagery*.

[21] C. Hann and M. Hickman. Projective curvature and integral invariants. *Acta applicandae mathematicae*, 74:177–193, 2002.

[22] Y. He, A. Ben Hamza, and H. Krim. A generalized divergence measure for robust image registration. *IEEE Transactions on Signal Processing*, 51:1211–1220, 2003.

[23] M. Hilaga, Y. Shinagawa, T. Kohmura, and T. L. Kunii. Topology matching for fully automatic similarity estimation of 3d shapes. In *Proceedings of the 28th annual conference on Computer graphics and interactive techniques table of contents*.

[24] M. O. Irfanoglu, B. Gokberk, and L. Akarun. 3D shape-based face recognition using automatically registered facial surfaces. In *ICPR*.

[25] V. Jain and H. Zhang. Shape-based retrieval of articulated 3d models using spectral embeddings. In *Geometric Modeling and Processing*.

[26] I. A. Kogan. Two algorithms for a moving frame construction. *Canad. J. Math.*, 55:266–291, 2003.

[27] R. Kohavi. A study of cross-validation and bootstrap for accuracy estimation and model selection. In *Proceedings of the Fourteenth International Joint Conference on Artificial Intelligence*, 1999.

[28] S. Lao, Y. Sumi, M. Kawade, and F. Tomita. 3D template matching for pose invariant face recognition using 3D facial model built with iso-luminance line based stereo vision. In *ICPR*.

[29] J. Lin. Divergence measures based on the shannon entropy. *IEEE Trans. Inform. Theory*, 37:145–151, 1991.

[30] W. Y. Lin, N. Boston, and Y. H. Hu. Summation invariant and its application to shape recognition. In *Proc. of ICASSP*, 2005.

[31] X. Lu and A. K. Jain. Integrating Range and Texture Information for 3D Face Recognition. In *Proc. 7th IEEE Workshop on Applications of Computer Vision*.

[32] S. Manay, D. Cremers, B. Hong, A. Yezzi, and S. Soatto. Integral invariants for shape matching. *IEEE Transactions on Pattern Analysis and Machine Intelligence*, 28(10):1602 – 1618, 2006.

[33] S. Manay, A. Yezzi, B. Hong, and S. Soatto. Integral invariant signatures. In *Proc. of the Eur. Conf. on Comp. Vision*, 2004.

[34] I. Mpiperis, S. Malassiotis, and M.G. Strintzis. Expression Compensation for Face Recognition Using a Polar Geodesic Representation. In *Proc. 3rd International Symposium on 3D Data Processing, Visualization, Transmission*.

[35] T. Nagamine, T. Uemura, and I. Masuda. 3D facial image analysis for human identification. In *International Conference on Pattern Recognition*.

[36] S. Nayar and R. Rolle. Reflectance based object recognition. *International Journal of Computer Vision*, 17(3):219–240, 1996.

[37] P. J. Olver. Joint invariant signatures. *Found. Comp. Math*, 1:3–67, 2001.

[38] P. J. Phillips, P. J. Flynn, T. Scruggs, K. W. Bowyer, J. Chang, K. Hoffman, J. Marques, J. Min, and W. Worek. Overview of the Face Recognition Grand Challenge. In *CVPR*, 2005.

[39] A. Ross and A. K. Jain. Information fusion in biometric. *Pattern Recognition Letters*, 24(13):2115–2125, 2003.

[40] s. Baloch, H. Krim, I. Kogan, and D. Zenkov. 3d object representationwith topo-geometric shape models. In *2005Eusipco*.

[41] C. Samir, A. Srivastava, and M. Daoudi. Automatic 3d face recognition using shapes of facial curves. *IEEE Transactions on Pattern Analysis and Machine Intelligence*, 28(11):1858–1863, 2006.

[42] J. Sato and R. Cipolla. Affine integral invariants for extracting symmetry axes. *Image and Vision Computing*, 15:627–635, 1997.

[43] J.A. Sethian. *Level Set Methods: Evolving Interfaces in Geometry, Fluid Mechanics, Computer Vision and Materials Sciences*. Cambridge University Press, 1996.

[44] Philip Shilane, Patrick Min, Michael Kazhdan, and Thomas Funkhouser. The Princeton Shape Benchmark. In *Shape Modeling International*.

[45] G. Taubin and D. Cooper. Object recognition based on moment (or algebraic) invariants. *Geometric Invariance in Computer Vision, J.L. Mundy and A. Zisserman (eds), MIT Press*, pages 375–397, 1992.

[46] F. Tsalakanidou, D. Tzocaras, and M. Strintzis. Use of depth and colour eigenfaces for face recognition. *Pattern Recognition Letters*, 24:1427–1435, 2003.

[47] T. Tung and F. Schmitt. Augmented reeb graphs for content-based retrieval of 3d mesh models. In *Shape Modeling Applications*.

[48] L. Van Gool, T. Moons, E. Pauwels, and A. Oosterlinck. Semi-differential invariants. *Geometric Invariance in Computer Vision, J.L. Mundy and A. Zisserman (eds), MIT Press*, pages 157–192, 1992.

[49] D. Xu and H. Li. 3-d affine moment invariants generated by geometric primitives. In *proceedings of ICPR*, pages 544 – 547, 2006.

[50] Y.Wang, C. Chua, and Y. Ho. Facial feature detection and face recognition from 2d and 3d images. *Pattern Recognition Letters*, 23:1191–1202, 2002.

[51] J. Zhang, K. Siddiqi, D. Macrini, A. Shokoufandeh, and S. Dickinson. Retrieving articulated 3-d models using medial surfaces and their graph spectra. In *CVPR*.

[52] W. Zhao, R. Chellappa, P.J Phillips, and A. Rosenfeld. Face recognition: A literature survey. *ACM Computing Survey*, 12:399–458, 2003.